

Preface – How to select a journal?

T. Czigány*

Department of Polymer Engineering, Faculty of Mechanical Engineering, Budapest University of Technology and Economics, Műegyetem rkp. 3., H-1111 Budapest, Hungary

Dear Readers,

You read the first issue of the ninth volume of **eXPRESS Polymer Letters**. We express our thanks to our authors, referees and readers for the increasing trust towards our journal reflected by the number of regular readers, downloads and by the continuous improvement of our impact factor. The latest impact factor of **eXPRESS Polymer Letters** is 2.953, meaning almost 30% improvements over that in the previous year. One year before we decided to become the member of the ‘elite club’, i.e. the group of the top 25% journals. This goal was reached as we are within the first 17% of the journals having impact factors. One can ask, of course whether the impact factor is the only thing distinguishing the journals from each other? After all, how should one select the proper journal for a manuscript nowadays when we are overloaded day by day by offers from newly launched journals? The first important rule is to be acquainted with the relevant literature, which already gives a hint where similar articles are published. This is important as it may happen that a very good article is submitted to a ‘wrong’ journal. In such cases there are usually two scenarios: The first is that the article is published in the given journal, however the interested readers will not find it, and as a result the article will not be cited, which is disadvantageous both for the journal and the author. Another possibility is that the editor refuses to publish the paper with and without reasoning. This may be annoying for the author, but in the long term, it serves his/her interest. The second most important rule is that based on the knowledge of the current literature the authors should be able to assess the quality of the paper, which may help in deciding whether to submit it to a journal

with impact factor, or to a local, or newly established journal. This latter category should be treated with reservation, as ‘bluff’ journals are proliferating, where papers are published without reviewing and edition, although publication costs are charged. The third most important rule of manuscript submission is again based on the knowledge of the literature: a proper order should be established for the journals thematically appropriate for the manuscript, which is typically based on their impact factors. The higher the impact factor of the journal the higher the probability that more colleagues will read them, thus one can be sure that the article will reach the interested readers. It is not by chance that a common part of all three rules is the proper knowledge of the literature, as without this it is impossible to write a good article or to select the proper journal. If one is convinced about the originality and novelty of the manuscript, one should dare to submit it to the best journals, as e.g. **eXPRESS Polymer Letters**.

I wish a proper journal selection for all authors, readers and referees of **eXPRESS Polymer Letters** and I wish to announce the March issue that will be dedicated to professor Karger-Kocsis, the chief editor of **eXPRESS Polymer Letters** on the occasion of his 65th birthday. Sincerely yours,



Prof. Dr. Tibor Czigány
editor

*Corresponding author, e-mail: czigany@eik.bme.hu
© BME-PT

Preparation and characterization of Protein A-immobilized PVDF and PES membranes

N. Akashi^{1*}, S. Kuroda²

¹Graduate School of Engineering, Gunma University 29-1 Hon-cho, Ohta, Gunma 373-0057, Japan

²Faculty of Science and Technology, Gunma University 29-1 Hon-cho, Ohta, Gunma 373-0057, Japan

Received 15 May 2014; accepted in revised form 29 July 2014

Abstract. Polyvinylidene fluoride (PVDF) and polyether sulfone (PES) membranes were activated using low-temperature plasma at atmospheric pressure, and their surface characteristics were investigated. In the plasma-treated PVDF, the XPS data showed that defluorination and oxidation reactions proceeded to 18 and 31%, respectively, at ± 4.0 kVp-p for 180 s. Hydroperoxide groups were detected on both the plasma-treated membranes. By decomposing the S2p spectrum, it was proven that the sulfide and sulfo groups were newly formed on the plasma-treated PES. Based on these findings, we proposed an activation mechanism. The SEM images showed that the macrovoid formations were maintained after the plasma treatment. Polyacrylic acid (PAA) was grafted on both of the plasma-treated membranes by thermal treatments. Protein A, originating from *Staphylococcus aureus*, was immobilized on the membrane grafted with PAA using the EDC/Sulfo-NHS system. Adsorption isotherms with a human immunoglobulin G (IgG) antibody were fitted with the monolayer Langmuir model, and the maximum binding capacity (q_m) and equilibrium association constant (K_a) were obtained. The ligand densities of the PVDF (pore size 0.45 and 5.0 μm) and PES (pore size 0.45 μm) membranes were 0.98, 1.42 and 2.06 $\text{mg}\cdot\text{mL}^{-1}$, respectively.

Keywords: polymer membranes, PVDF, PES, Protein A, plasma

1. Introduction

Fluoropolymers have excellent features, such as electrical and chemical resistance, high thermal stability and low surface energies [1]. Fluorinated polymers are applied in many industries, such as for thin film technology magnetic media, non-stick cookware and engineering plastics [2]. One of the commercially available fluoropolymers is polyvinylidene fluoride (PVDF). Research and application of PVDF membranes has been reported since the 1980s [3]. One of the reasons for this is that PVDF dissolves in common organic solvents, so porous PVDF membranes can be produced via phase inversion methods with a simple immersion precipitation process. On the other hand, polyether sulfone (PES) has also been widely available commercially, and has excel-

lent mechanical strength and is a thermally stable polymer [4]. Thus, PES membranes have been adopted as important materials in the food, hemodialysis and water purification fields, as well as for biopharmaceutical drugs as microfiltration (MF) and ultrafiltration (UF) [5]. PES and PVDF membranes are valuable as research subjects in separation fields. However, PVDF and PES have the issue of being intrinsically and severely hydrophobic [6]. As the result, proteins dissolved in aqueous solutions tend to clog the membranes. Therefore, manufacturers provide membranes that are hydrophilized to decreasing the nonspecific protein binding capacity with various surface modifications to prevent objective substances, such as recombinant proteins, from fouling the membranes [7, 8]. Other advancements

*Corresponding author, e-mail: akashi.n@jcom.home.ne.jp

in the field have been related to pore size distributions and membrane types, which are critical factors to achieve anti-fouling properties, and deal with variations at the production scale. High capacity membranes have been developed for the biotechnology industry with varying pore size distributions, such as isotropic and anisotropic structures [9].

In recent years, many functionalized membranes with surface modifications have been reported [10–12]. There has been significant interest in using affinity membrane chromatography for bioprocessing, but few reports are applied in production scales because the adsorption capacities of the affinity membranes are relatively low compared with those for conventional bead chromatography [13]. Humanized monoclonal antibodies (mAbs), which belong to a subclass of IgG, have been utilized in clinical fields as drug products [14]. To capture mAbs efficiently from the pool of the mAb production, Protein A is widely applied as a ligand on affinity chromatography media because Protein A strongly binds on the Fc region of IgG [15]. However, native Protein A originates from *Staphylococcus aureus* [9]. Therefore, it is important to establish a method for immobilizing Protein A on the media because of the decrease in the amount of leached Protein A. Simultaneously, a media with good chemical resistance and thermally stable features should be selected. As such, PVDF and PES membranes are important candidates as affinity media.

Plasma processing is a dry process for clean and energy saving surface modifications [16, 17]. Compared to plasma processing with a vacuum, atmospheric pressure low-temperature plasma does not need equipment for vacuum processing [18]. Plasma induced free radical polymerization is a useful technique for grafting polymers to hydrophilize or functionalize the surface of a polymeric substrate [19]. On the other hand, surface modifications on hydrophilic PVDF membranes have also been reported to have a covalent coupling of lysine as model of biologically active molecules [20]. It is highly plausible to minimize nonspecific adsorption on the membrane because the protein adsorption capacity of hydrophobic and hydrophilic PVDF membranes varies significantly, reportedly from 1157 and 84 mg·m⁻² [21].

The first goal of our study was to reveal the activation mechanism of PVDF and PES membranes activated by atmospheric pressure low-temperature

plasma. The surface chemicals and morphological properties of the membranes were characterized by attenuated total reflection (ATR), Fourier transform infrared (FT-IR) spectroscopic analysis, scanning electron microscopy (SEM) and X-ray photoelectron spectroscopy (XPS). The second goal of our study was to characterize the properties of Protein A-immobilized PVDF and PES membranes. The adsorption capacities with human IgG were confirmed according to the monolayer Langmuir model [22], and the ligand density on the membranes was also measured using a bicinchoninic acid (BCA) protein assay [23].

2. Experimental

2.1. Materials

PVDF (Durapore[®], hydrophilic) membranes were purchased from Merck Millipore Corp. (Darmstadt, Germany), commercially named HVLP01300 (pore size 0.45 μm) and SVLP01300 (pore size 5.0 μm). A PES membrane (Millipore Express[®] PLUS) was also purchased from Merck Millipore Corp., commercially named HPWP01300 (pore size 0.45 μm). Protein A from *Staphylococcus aureus* was purchased from Calbiochem (Darmstadt, Germany). *N*-Hydroxysulfosuccinimide (Sulfo-NHS), 1-(3-Dimethylaminopropyl)-3-ethylcarbodiimide (EDC) HCl, 2 (*N*-morpholino) ethanesulfonic acid (MES) and hydroxylamine HCl were purchased from ProteoChem, Inc. (IL, United States). An acrylic acid (AA) monomer and IgG from human serums were purchased from Sigma-Aldrich, Inc. (MO, United States). AA was distilled in a nitrogen atmosphere prior to use. The Micro BCA protein assay kit was purchased from Thermo Fisher Scientific Inc. (MA, United States). PBS (–) was purchased from Nissui Pharmaceutical Co., Ltd (Tokyo, Japan). The purity of the argon gas used was in excess of 99.99%.

2.2. Plasma reactor

The plasma reactor consists of a high frequency pulse power supply, a gas supply unit and a cold atmospheric pressure plasma torch (CAPPLAT). The CAPPLAT has a cylindrical structure in which the plasma is generated. The plasma is blown out through the end of the CAPPLAT, which consists of two co-axial cylindrical electrodes. The inner electrode, a copper tube (OD: 8 mm, ID: 7 mm), is connected to the power supply. The outer electrode (thickness: 1 mm, length: 20 mm) is made of alu-

minum and grounded. As a dielectric barrier, a silicone tube (thickness: 2.5 mm) is placed between the two electrodes. The outlet of the CAPPLAT is embedded in the edge of a perforated silicone tube.

2.3. Preparation of the PVDF and PES membranes immobilized with Protein A

Figure 1 shows a schematic illustration of the preparation for the PVDF/PES membranes immobilized with Protein A. Prior to the surface modification experiment, the membranes were rinsed with ethanol and dried at room temperature. For plasma treatment of the membranes, argon gas was fed into the CAPPLAT at a flow rate of $5 \text{ L}\cdot\text{min}^{-1}$, and the plasma was generated under an applied voltage of $\pm 4 \text{ kVp-p}$, frequency of 20 kHz, treatment time of 180 s and a duty cycle of 50%. The membranes were treated with plasma 20 mm away from the torch end. Subsequently, the membranes were exposed to air for 20 min at 35°C . The air-exposed membranes were immersed in an aqueous solution containing 20% (v/v) of AA monomer. After bubbling with nitrogen for 20 min to remove dissolved oxygen, the ampoules were sealed and heated at 70°C to initiate graft polymerization. The PVDF and PES membranes grafted with polyacrylic acid (hereafter called PVDF-g-PAA and PES-g-PAA, respectively or PVDF/PES-g-PAA) were rinsed with distilled water to remove non-grafted monomers. Protein A was immobilized on the PVDF/PES-g-PAA membranes using the EDC/Sulfo-NHS method. The membranes were activated with a $4 \text{ mmol}\cdot\text{L}^{-1}$ EDC, $10 \text{ mmol}\cdot\text{L}^{-1}$ Sulfo-NHS in $100 \text{ mmol}\cdot\text{L}^{-1}$ MES, $500 \text{ mmol}\cdot\text{L}^{-1}$

NaCl buffer solution with a pH of 6.0 for 15 min at room temperature. The immobilization of Protein A was carried out in a solution of $1 \text{ mg}\cdot\text{mL}^{-1}$ Protein A in $100 \text{ mmol}\cdot\text{L}^{-1}$ MES, $500 \text{ mmol}\cdot\text{L}^{-1}$ NaCl buffer with a pH of 6.0 under mild agitation for 3.0 h at room temperature. The immobilization reaction of the PVDF and PES membranes (hereafter called PVDF-g-PAA-PrA and PES-g-PAA-PrA, respectively or PVDF/PES-g-PAA-PrA) was quenched by adding hydroxylamine HCl to give a final concentration of $10 \text{ mmol}\cdot\text{L}^{-1}$. The membranes were rinsed with a solution of PBS (-) to remove loosely absorbed Protein A and the MES buffer solution, and then kept in a solution of PBS (-) at 5°C .

2.4. ATR FT-IR measurement

ATR FT-IR spectroscopic investigations were carried out with a Nicolet iS10 spectrometer (Thermo Fisher Scientific Inc.) using a Ge crystal. The spectra were collected by cumulating 64 scans at a resolution of 2 cm^{-1} .

2.5. XPS measurement

XPS was performed on a Kratos AXIS Nova spectrometer (Manchester, United Kingdom) using a monochromatized Al K α X-ray source (1486.6 eV photons). All measurements were made at a photoelectron takeoff angle of 45° . High resolution analyses were carried with a constant dwell time of 200 ms, pass energy of 20 eV and an energy resolution of 0.1 eV. All binding energies (BEs) were referenced to the C1s hydrocarbon peak at 286.4 eV. Spectra were analyzed using XPSPEAK software

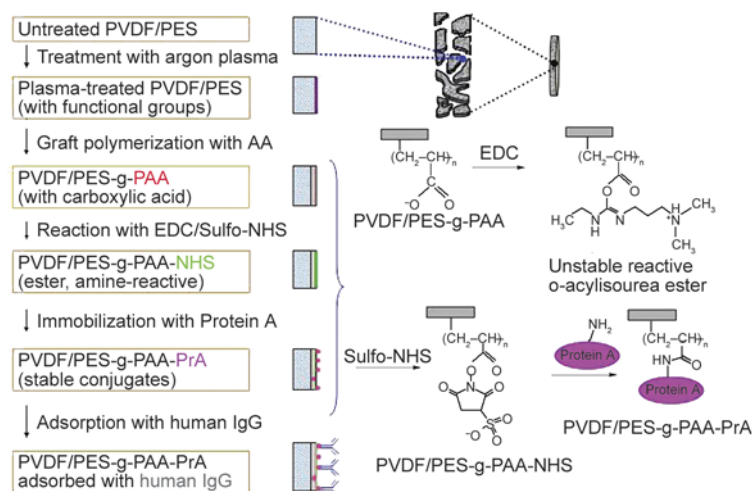


Figure 1. Schematic illustration of the preparation for the PVDF and PES membranes immobilized with Protein A and the adsorption with human IgG

(version 4.1). Curve fitting of the high resolution spectra used 30% Gaussian/70% Lorentzian mixed line shapes for each component.

2.6. Determination of adsorption capacities

The nonspecific adsorption on the PVDF/PES-g-PAA membranes and the adsorption isotherm on the PVDF/PES-g-PAA-PrA membranes with a human IgG were measured. Four of the membranes were employed in each closed glass vessel. The membranes were equilibrated in a solution of PBS (–) at a pH of 7.4 as an equilibrium buffer solution for 10 min. The equilibrium buffer solution was replaced with 4 mL of the equilibrium buffer solution dissolved with different concentrations of human IgG, and incubated for 12 h at 20°C. The amount of human IgG adsorbed on the membranes was determined by measuring the concentration of human IgG before and after the adsorption experiments were performed. Each concentration of human IgG was measured by a Micro BCA protein assay. The adsorption isotherms were constructed by plotting the adsorption capacity on the membranes versus the equilibrium concentration of human IgG dissolved in the liquid. Data were analyzed according to the monolayer Langmuir model shown in Equation (1):

$$q^* = \frac{q_m \cdot K_a \cdot c^*}{1 + K_a \cdot c^*} \quad (1)$$

where the c^* and q^* represented the equilibrium concentration of the human IgG dissolved in the liquid and the equilibrium capacity of human IgG adsorbed on the membranes, respectively. The variable q_m represented the maximum adsorption capacity on the membranes and K_a represented the equilibrium association constant. Equation (1) was transformed into a linear form as a double reciprocal plot, shown in Equation (2), to calculate q_m and K_a :

$$\frac{1}{q^*} = \frac{1}{q_m} + \frac{1}{K_a \cdot q_m} \cdot \frac{1}{c^*} \quad (2)$$

where the q^* and q_m were calculated in $\text{mg}\cdot\text{mL}^{-1}$, which represents the weight of human IgG adsorbed per volume of the membrane. Variable K_a was calculated in $\text{L}\cdot\text{mol}^{-1}$ by considering the molecular weight to be 146 kDa [24].

2.7. Determination of ligand densities

The amount of Protein A covalently immobilized on each PVDF/PES-g-PAA-PrA membrane was meas-

ured with a BCA protein assay [13]. The ligand density was calculated in $\text{mg}\cdot\text{mL}^{-1}$, which represents the weight of Protein A immobilized per volume of the membrane.

2.8. Procedure of stability test

The PVDF/PES-g-PAA-PrA membranes were treated by repeating the cycle of equilibration, adsorption, elution, washing and regeneration to estimate the stability of the membranes. Four membranes were employed in each closed glass vessel. First, the membranes were equilibrated by a solution of PBS (–) at a pH of 7.4 as an equilibrium buffer solution for 10 min (equilibration), and then replaced in 4 mL of the equilibrium buffer solution dissolved 0.1 $\text{mg}\cdot\text{mL}^{-1}$ human IgG for 10 min (adsorption). Secondly, the membranes were immersed in 4 mL of 0.1 $\text{mol}\cdot\text{L}^{-1}$ citric acid buffer solution at a pH of 3.0 for 10 min (elution), and then washed with a solution of PBS (–) at a pH of 7.4 for 10 min (washing). Finally, the membranes were immersed in 20% (v/v) ethanol for 20 min (regeneration). After the five cycles were performed, the ligand densities of the membranes were measured.

2.9. SEM measurement

The surface and cross-section morphologies of the membranes were examined by SEM, using a Hitachi S-3000N electron microscope (Tokyo, Japan). A thin layer of Pt was sputtered on the sample surface prior to the SEM measurement. The SEM measurements were performed at an accelerating voltage of 15.0 kV.

3. Results and discussion

3.1. Structure characterization of the membranes by ATR-FTIR analysis

Figure 2 shows the respective ATR-FTIR spectra of PES membrane and represented the data of the membranes untreated, treated with argon plasma, grafted with AA and those immobilized with the Protein A. The ATR-FTIR spectra of the PVDF membranes were similar to those in the previous report [19]. The strong absorption bands at 1107–1240 cm^{-1} were characteristic bands of aromatic ethers and sulfonyl groups of PES (Figure 2 curve a). The spectrum of the plasma-treated PES membrane contained a weak absorption band at approximately 1700 cm^{-1} (Figure 2 curve b). The spectrum of the PES-g-PAA membrane appeared with a strong car-

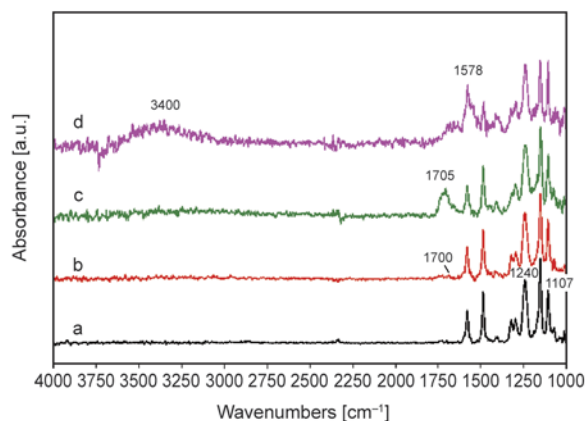


Figure 2. ATR-FTIR spectra of PES membranes. (a) untreated, (b) treated with argon plasma (treatment: ± 4.0 kVp-p, 180 s), (c) grafted with AA (treatment: 20% (v/v) AA, 70°C, 20 min) and (d) immobilized with Protein A (treatment: 1 mg·mL⁻¹, 3 h)

bonyl (C=O) stretching absorption band at 1705 cm⁻¹ (Figure 2 curve c). This indicates that polyacrylic acid chains were successfully grafted on the membrane. The spectrum of the PES-g-PAA-PrA membrane revealed the increase of the absorption band attributed to the NH-deformation vibration at 1578 cm⁻¹, and broad absorption bands attributed to primary amino groups with a maximum at 3400 cm⁻¹ were strongly observed (Figure 2 curve d). Consequently, it was demonstrated that Protein A was successfully immobilized on the PES-g-PAA membrane.

3.2. Structure characterization of the membranes by XPS analysis

We investigated the influence of defluorination and oxidation on the plasma treatment time and applied voltage compared with untreated PVDF membranes. The atomic composition was estimated from relative intensities of C1s, F1s, O1s, N1s and S2p high resolution spectra. Atomic ratios of the PVDF and PES samples are summarized in Tables 1 and 2, respectively.

The F/C and O/C atom ratios of the untreated PVDF membrane were individually 0.72 and 0.13 due to the hydrophilic treatment from the manufacturer. In the case of the plasma-treated PVDF membranes, the defluorination reactions proceeded 18, 18 and 24% for 60, 180 and 300 s of plasma exposure time, respectively. Secondly, the degree of defluorination resulted in 7, 18 and 18% at ± 2.8 , ± 4.0 and ± 5.0 kVp-p, respectively. The sample treated at ± 5.0 kVp-p was appeared to have an intensively

Table 1. Atomic ratios of the PVDF membrane (pore size 0.45 μ m) surfaces exposed to argon plasma (treatment: flow rate of argon gas at 5 L·min⁻¹)

Plasma treatment		Atomic ratio		Defluorination [%]	Oxidation [%]
Voltage [\pm kVp-p]	Exposure time [s]	F/C	O/C		
–	–	0.72	0.13	0	0
4.0	60	0.59	0.16	18	23
4.0	180	0.59	0.17	18	31
4.0	300	0.55	0.20	24	54
2.8	180	0.67	0.18	7	38
4.0	180	0.59	0.17	18	31
5.0	180	0.59	0.20	18	54

Table 2. Atomic ratios of the PES membrane surfaces exposed to argon plasma (treatment: flow rate of argon gas at 5 L·min⁻¹)

Plasma treatment		Atomic ratio		Oxidation [%]
Voltage [\pm kVp-p]	Exposure time [s]	O/C	S/C	
–	–	0.37	0.049	0
4.0	60	0.50	0.087	35
4.0	180	0.66	0.075	78
4.0	300	0.77	0.064	108
2.8	180	0.54	0.069	46
4.0	180	0.66	0.075	78
5.0	180	0.78	0.110	111

burnt area, so it was presumed to lead to heavy etching reactions. In a recent related report of the argon plasma treatment to other fluoropolymers, Hidzir *et al.* [25] described that the chemical environment of the surface of expanded poly (tetrafluoroethylene), which was treated with 100 W argon plasma under the low pressure and subsequently exposed to air changed substantially, displayed evidence of defluorination (F/C atom ratio of 1.9 from 2.4). On the other hand, oxidation reactions progressed 23, 31 and 54% for 60, 180 and 300 s, respectively, compared with an untreated PVDF membrane. Moreover, the degree of oxidation was 38, 31 and 54% at ± 2.8 , ± 4.0 and ± 5.0 kVp-p. These data imply that the oxygen functional groups, such as peroxide species, were generated on the plasma-treated PVDF membrane.

The O/C and S/C atom ratios of the untreated PES membrane were 0.37 and 0.049, respectively, due to the hydrophilic treatment. In the case of the plasma-treated PES membranes, the oxidation reactions proceeded 35, 78 and 108% for 60, 180 and 300 s, respectively. Secondly, the degree of oxidation was 46, 78 and 111% at ± 2.8 , ± 4.0 and ± 5.0 kVp-p,

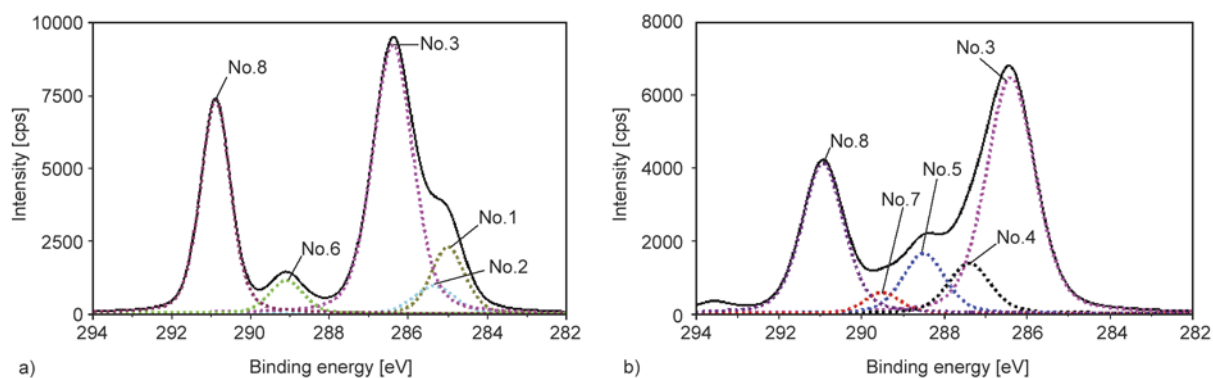


Figure 3. High resolution XPS spectra of C1s. (a) untreated PVDF (pore size 0.45 μm) membrane and (b) PVDF membrane treated with argon plasma (treatment: ± 4.0 kVp-p, 180 s).

respectively. Moreover, the oxidation reaction on the PES membranes progressed approximately two times higher than that of the PVDF membranes. These findings suggest that the plasma-treated PES membrane has more initiation sites for graft polymerization relative to the plasma-treated PVDF membrane.

Figure 3 shows C1s high resolution spectra for the untreated PVDF membrane and plasma-treated PVDF membrane. The decomposed peaks are illustrated as dotted lines. The underlined C, O or S means the objective was carbon, oxygen or sulfur, respectively.

The C1s high resolution spectrum of the untreated PVDF membrane was assigned to five peaks at BEs of 285.0 eV due to $\text{CH}(\text{COOH})-\underline{\text{C}}\text{H}_2-\text{CH}(\text{COOH})$: No. 1, 285.4 eV due to $\underline{\text{C}}\text{H}-\text{COOH}$: No. 2, 286.4 eV due to $\text{CF}_2-\underline{\text{C}}\text{H}_2-\text{CF}_2$: No. 3, 289.1 eV due to $\text{CH}-\underline{\text{C}}\text{OOH}$: No. 6 and 290.9 eV due to $\text{CH}_2-\underline{\text{C}}\text{F}_2-\text{CH}_2$: No. 8 (Figure 3a). These data indicate that the untreated PVDF membrane is cross-linked with hydroxyalkyl acrylate to hydrophilize the membrane [7]. The C1s high resolution spectrum of the plasma-treated PVDF membrane was decomposed into five peaks (Figure 3b) [19]. The five peaks appeared at BEs of 286.4, 287.4, 288.5, 289.5 and 290.9 eV, which were assigned to $\text{CF}_2-\underline{\text{C}}\text{H}_2-\text{CF}_2$, $\text{CH}_2-\underline{\text{C}}\text{F}=\text{CH}$, $\text{CH}_2-\underline{\text{C}}\text{F}=\text{CH}_2$ and hydroperoxide ($\text{CH}_2-\underline{\text{C}}\text{H}(-\text{OOH})-\text{CH}_2$) groups (No. 3); hydroperoxide ($\text{CF}_2-\underline{\text{C}}\text{H}(-\text{OOH})-\text{CF}_2$) (No. 4); carbonyl ($\text{CF}_2-\underline{\text{C}}\text{HO}$) and $\text{CH}_2-\underline{\text{C}}\text{FH}-\text{CH}_2$ groups (No. 5); hydroperoxide ($\text{CH}_2-\underline{\text{C}}\text{F}(-\text{OOH})-\text{CH}_2$) (No. 7); and $\text{CH}_2-\underline{\text{C}}\text{F}_2-\text{CH}_2$ and carbonyl ($\text{CH}_2-\underline{\text{C}}\text{FO}$) and $\text{CH}=\underline{\text{C}}\text{F}_2$ groups (No. 8), respectively. The composition showed that CF_2 carbons were modified into $\underline{\text{C}}\text{FH}$, $\underline{\text{C}}(-\text{OOH})$ and $\underline{\text{C}}\text{FO}$ carbons in the plasma exposure. Lee and Shim have measured the concen-

tration of peroxides formed on the argon plasma-treated PVDF membranes (pore size 0.22 μm and 70% porosity) by the 1,1-diphenyl-2-picrylhydrazyl (DPPH) method [26]. The density of peroxides showed $2.5 \cdot 10^{-8} \text{ mol} \cdot \text{cm}^{-2}$ at 30 W for 30 s in 50 mTorr. Although the density increased until the 30 s exposure, interestingly, it decreased with a 40 s exposure. These data suggested that the C1s high resolution spectrum shape of the plasma-treated PVDF membrane as shown in Figure 3 was dependent on the exposure conditions.

The C1s high resolution spectrum of the PVDF-g-PAA membrane was decomposed into three characteristic peaks attributable to the AA graft polymerization. The three peaks observed at BEs of 285.0, 285.4 and 289.1 eV, were individually assigned to the $\text{CH}(\text{COOH})-\underline{\text{C}}\text{H}_2-\text{CH}(\text{COOH})$; $\underline{\text{C}}\text{H}-\text{COOH}$; and carboxy ($\text{CH}-\underline{\text{C}}\text{OOH}$) groups.

Graft polymerization of acrylic acid is a useful method for forming many carboxy groups on the membranes to react with EDC, and subsequently results in a semi-stable amine-reactive NHS ester. In addition, Huang *et al.* [27] have reported that plasma induced grafting of acrylic acid significantly improved the wettability behavior of the PVDF nanofiber membranes. In this way, there are some advantages of applying the polymerization, but it is important to optimize the grafting conditions because excessive grafting leads to a decrease in the porosity and surface area of the microporous membranes with particularly small pore sizes.

We also investigated the data for C1s, O1s and S2p high resolution spectra of the PES membranes (Figure 4). The C1s and O1s high resolution spectra and percentages of each bond type on the PES-g-PAA membrane were consistent with the results of the PVDF-g-PAA membrane.

The C1s high resolution spectrum of the untreated PES membrane was assigned to three peaks at BEs of 284.7 eV due to aromatic $\underline{\text{C}}-\underline{\text{C}}$: No. 1, 285.3 eV due to $\underline{\text{C}}-\text{SO}_2-\underline{\text{C}}$: No. 2 and 286.3 eV due to $\underline{\text{C}}-\text{O}-\underline{\text{C}}$ and phenolic carbons that bond to hydroxy groups: No. 3 (Figure 4a). The $\pi-\pi^*$ shake-up satellite peak was shown at 291.7 eV. The peak area ratio at 286.3 eV (No. 3) was 37%, which was higher than the theoretical value of hydrophobic PES, and the peak area ratio at 284.7 eV (No. 1) was 44%, which was lower than that of hydrophobic PES. These results suggest that the dehydrogenation and oxidation reactions of the benzene ring on the PES membrane progressed, and several phenolic carbons are constituted on the membrane [8]. Secondly, the O1s

high resolution spectrum of the untreated PES membrane was deconvoluted into three peaks at BEs of 531.6 eV due to the sulfonyl group, $\text{C}-\underline{\text{S}}\text{O}_2-\text{C}$: No. 4, 532.3 eV due to oxygen in the hydroxy group, $\text{R}-\underline{\text{O}}-\text{H}$: No. 5 and 533.3 eV due to $\text{C}-\underline{\text{O}}-\text{C}$: No. 6 (Figure 4c). Thirdly, the S2p high resolution spectrum of the untreated PES membrane was deconvoluted into two distinct peaks at BEs of 167.6 eV due to $\text{S}2\text{p}_{3/2}$ for $\text{C}-\underline{\text{S}}\text{O}_2-\text{C}$: No. 10 and 168.8 eV due to $\text{S}2\text{p}_{1/2}$ for $\text{C}-\underline{\text{S}}\text{O}_2-\text{C}$: No. 12 (Figure 4e).

On the other hand, the C1s high resolution spectrum of the plasma-treated PES membrane was decomposed into three peaks of 284.7 eV due to aromatic $\underline{\text{C}}-\underline{\text{C}}$: No. 1, 285.3 eV due to $\underline{\text{C}}-\text{SO}_2-\underline{\text{C}}$: No. 2 and 286.3 eV due to $\underline{\text{C}}-\text{O}-\underline{\text{C}}$, $\underline{\text{C}}-\text{OH}$ and hydroperoxide

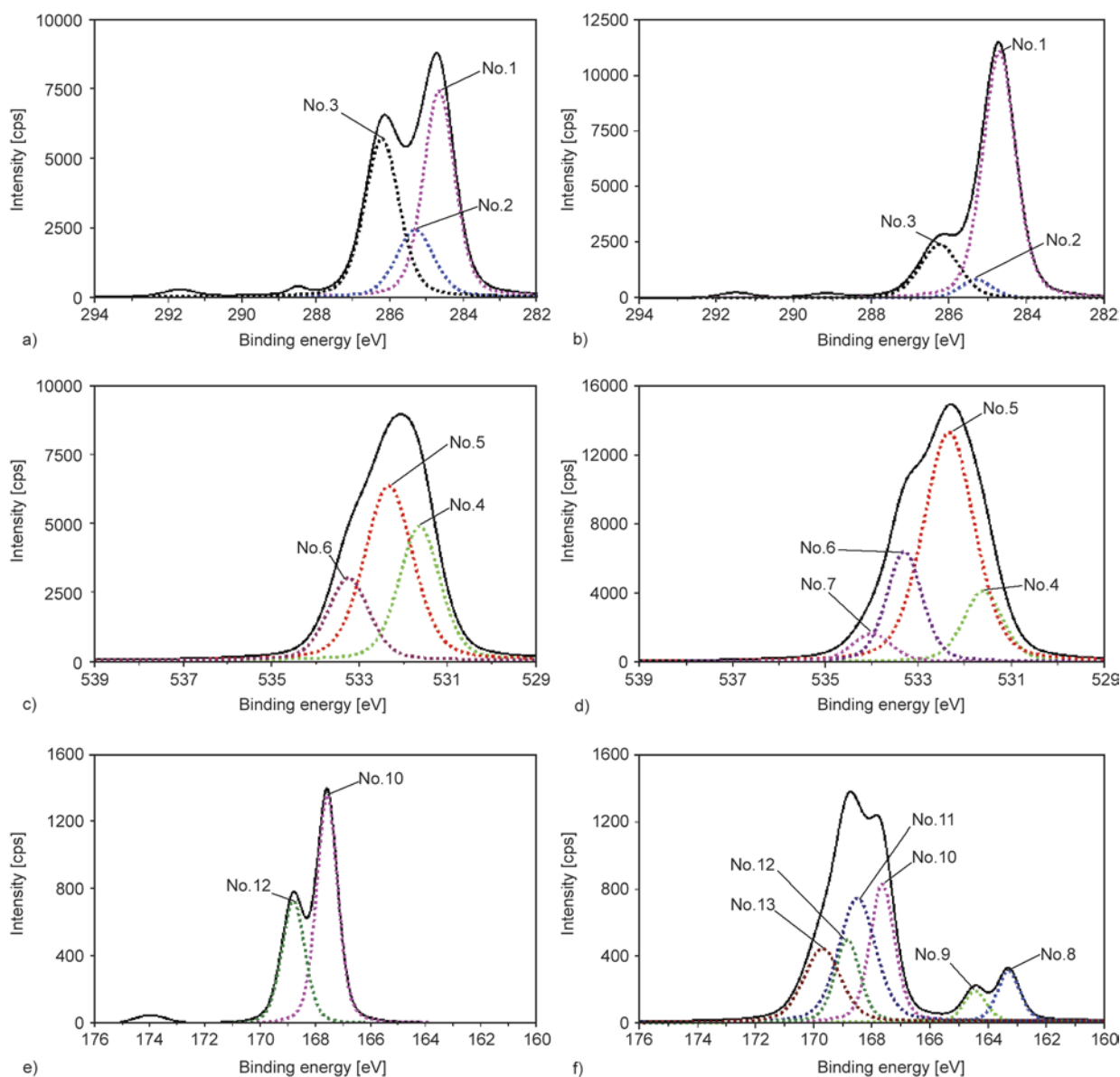


Figure 4. High resolution XPS spectra of C1s (a, b), O1s (c, d) and S2p (e, f): (a, c, e) untreated PES membrane and (b, d, f) PES membrane treated with argon plasma (treatment: ± 4.0 kVp-p, 180 s)

(C–CH(–OOH)–C) groups: No. 3 (Figure 4b). The peak area ratio of the π - π^* shake-up was 2%, which was approximately the same level as that of the untreated PES membrane. Secondly, the O1s high resolution spectrum of the plasma-treated PES membrane was curve-fitted with four peaks at BEs of 531.6 eV due to C–SO₂–C: No. 4, 532.3 eV due to R–OH: No. 5, 533.3 eV due to C–O–C and C–CH(–OOH)–C: No. 6, and 534.0 eV for hydroperoxide R–OOH: No. 7 (Figure 4d). Finally, the S2p high resolution spectrum of the plasma-treated PES membrane was deconvoluted into six peaks at BEs of 163.3 eV due to S2p_{3/2} for the sulfide group, C–S–C: No. 8, 164.4 eV due to S2p_{1/2} for C–S–C: No. 9 [28], 167.6 eV due to S2p_{3/2} for C–SO₂–C: No. 10, 168.5 eV due to S2p_{3/2} for the sulfo group, C–SO₃H: No. 11, 168.8 eV due to S2p_{1/2} for C–SO₂–C: No. 12 and 170.1 eV due to S2p_{1/2} for C–SO₃H: No. 13 (Figure 4f).

Based on these results, we proposed an activation mechanism on the membranes treated with atmospheric pressure low-temperature plasma. The each peak area ratio of 285.3 eV (No. 2 in Figure 4b) and 531.6 eV (No. 4 in Figure 4d) was individually 5 and 14%, which was lower than those of the untreated PES membrane. Two deconvoluted peaks were assigned for C–SO₂–C and C–SO₂–C, respectively. These findings suggest that metastable argon, which is the most important active species in the present plasma, collides with the oxygen in the sulfonyl group primarily and results in link cleavage, the formation of radicals such as phenyl radical, and deoxidization reactions. After the oxidation reaction proceeded due to air exposure, it was considered that functional groups were formed such as C–CH(–OOH)–C (No. 7 in Figure 4d) and C–SO₃H (No. 11, 13 in Figure 4f) groups. Furthermore, the peak area ratio of the π - π^* shake-up was comparable before and after plasma treatment. It was also suggested that there was low damage and disruption to the benzene ring by treating with plasma under this condition. Therefore, the phenyl radical and radicals originating from the hydroperoxide groups by thermal treatment would be significantly important initiators to induce graft polymerization with AA on the PES membranes.

3.3. Determination of the human IgG adsorption capacity of affinity membranes

Adsorption isotherms of the PVDF/PES-g-PAA-PrA membranes were constructed to investigate the capacity as affinity membranes. Simultaneously, non-specific adsorption tests were performed with the PVDF/PES-g-PAA membranes prior to immobilization with Protein A. The equilibrium capacities adsorbed on the membranes (q^*) were calculated via the equilibrium concentration of the human IgG dissolved in the liquid (c^*) (Figure 5).

The adsorption isotherms constructed with the PVDF/PES-g-PAA-PrA membranes were fitted with the monolayer Langmuir model. On the other hand, as the result of the nonspecific protein adsorption test, the q^* of the PVDF membranes with pore sizes of 0.45 and 5.0 μm and PES membranes with a pore size 0.45 μm were indicated to have relatively low levels of 0.09, 0.11 and 0.12, respectively. The thermodynamic parameters, which were obtained with the monolayer Langmuir model, are listed in Table 3. In terms of the PVDF-g-PAA-PrA membranes, it can be seen that the maximum binding capacity (q_m) for a pore size 0.45 μm was 0.55 $\text{mg}\cdot\text{mL}^{-1}$, which was similar to that with a pore size 5.0 μm . On the other hand, the equilibrium association constant (K_a) for a pore size of 5.0 μm was $10.6\cdot 10^6 \text{ L}\cdot\text{mol}^{-1}$, which was around three times higher than that with a pore size of 0.45 μm . These findings suggest that there is a relationship between the pore size and K_a .

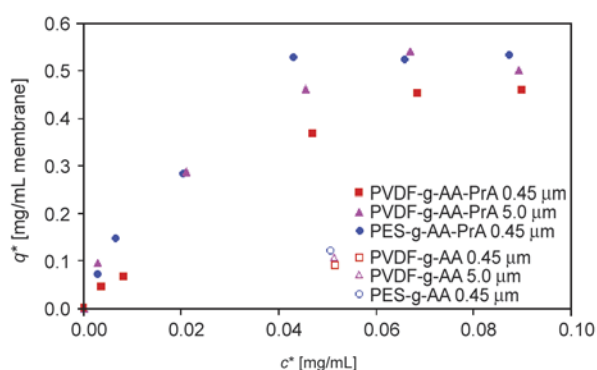


Figure 5. Adsorption isotherms of human IgG binding to the PVDF (pore size 0.45 μm : closed square, 5.0 μm : closed triangle) and PES (pore size 0.45 μm : closed circle) membranes that were immobilized with Protein A. Open symbols represent the results of the nonspecific adsorption tests. Adsorption conditions: PBS (–), pH 7.4 as an equilibrium buffer, 20°C, 12 h

Table 3. Thermodynamic parameters from adsorption isotherms of human IgG on the PVDF and PES membranes immobilized with Protein A, according to the Langmuir monolayer model. Adsorption conditions: PBS (-), pH 7.4 as an equilibrium buffer, 20°C, 12 h

Membrane	Pore size [μm]	q_m [$\text{mg}\cdot\text{mL}^{-1}$]	K_a [$\text{L}\cdot\text{mol}^{-1}$]	RSQ
PVDF-g-PAA-PrA	0.45	0.55	$3.3\cdot 10^6$	0.955
	5.0	0.56	$10.6\cdot 10^6$	0.992
PES-g-PAA-PrA	0.45	0.76	$4.9\cdot 10^6$	0.997

Membrane affinity matrices require K_a values above $10^5 \text{ L}\cdot\text{mol}^{-1}$ to ensure efficient adsorption, without risking ligates elution during washing [29]. Compared with capacities of the PVDF/PES-g-PAA-PrA membranes for the same pore size of $0.45 \mu\text{m}$, the q_m of the PES membrane was $0.76 \text{ mg}\cdot\text{mL}^{-1}$, which was 38% higher than that of the PVDF membrane. On the other hand, the K_a of the PES membrane was $4.9\cdot 10^6 \text{ L}\cdot\text{mol}^{-1}$, which was similar to that of the PVDF membrane. To further improve these thermodynamic parameters, it would be meaningful to adopt a cross-linking agent that avoids conjugating with the human IgG binding site of Protein A.

As the latest examples of protein purification adopted similar membranes, Sun and Wu [30] have proposed the bovine serum albumin (BSA) separation using mixed matrix membranes (MMMs) comprising of hydroxyapatite (HAP) inside a PES matrix. The BSA adsorption capacity of HAP particles in MMMs reached a maximum (29.4 mg/g membrane) at a pH of 7. Saufi and Fee [31] have demonstrated that the hydrophobic interaction chromatography MMMs, which consisted of a PVDF membrane using a commercial phenyl resin, had static binding capacities (on the membrane volume basis) of $18.4 \text{ mg}\cdot\text{mL}^{-1}$ for β -lactoglobulin. Hence, by integrating affinity membranes and various MMMs that have a distinct separation mode in the downstream processing of the mAb production, the common issues with packed bed column chromatography, such as complicated packing or operations, could be resolved, leading to reduced production costs.

The ligand densities on the PVDF/PES-g-PAA-PrA membranes were measured to investigate the amount of Protein A immobilized on the membrane surface. The results of the stability tests are also included in Table 4.

Compared with the influence of the PVDF-g-PAA-PrA membranes, the ligand density for a pore size

Table 4. Ligand density on the PVDF and PES membranes immobilized with Protein A. Values of ligand densities mean average ($n = 3$). Condition of one cycle: equilibration (PBS (-), pH 7.4, 10 min), adsorption ($0.1 \text{ mg}\cdot\text{mL}^{-1}$ human IgG in PBS (-), pH 7.4, 10 min), elution ($0.1 \text{ L}\cdot\text{mol}^{-1}$ citric acid buffer, pH 3.0, 10 min), washing (PBS (-), pH 7.4, 10 min) and regeneration (20% (v/v) ethanol, 20 min).

Membrane	Pore size [μm]	Cycle	Ligand density [$\text{mg}\cdot\text{mL}^{-1}$]	S.D.
PVDF-g-PAA-PrA	0.45	-	0.98	0.07
		5	0.94	0.06
	5.0	-	1.42	0.10
		5	1.51	0.13
PES-g-PAA-PrA	0.45	-	2.06	0.04
		5	1.98	0.08

$5.0 \mu\text{m}$ was $1.42 \text{ mg}\cdot\text{mL}^{-1}$, which was 49% higher than that for a pore size $0.45 \mu\text{m}$. On the other hand, compared with capacities of the PVDF/PES-g-PAA-PrA membranes for the same pore size of $0.45 \mu\text{m}$, the ligand density of the PES membrane was $2.06 \text{ mg}\cdot\text{mL}^{-1}$, which was approximately two times higher than that of the PVDF membrane. One of the explanations is that the O/C atom ratio of the plasma-treated PES membrane was 0.66 (Table 2), which was 3.9 times higher than that of the plasma-treated PVDF membranes (Table 1). Therefore, it was considered that the functional groups necessary for initiating graft polymerizations were generated more on the plasma-treated PES membranes relative to the PVDF membranes. On the other hand, for the PES membrane, the low accessibility to the ligand with the human IgG is suggested by grafting rich polymerization.

The ligand density was determined using a BCA protein assay as described in the experimental section, and this assay is tuned to detect not only active Protein A but also Protein A that is not capable of binding with human IgG due to the conjugation with the binding site of human IgG. Considering the q_m of the PVDF/PES-g-PAA-PrA membranes for pore size $0.45 \mu\text{m}$ shown in Table 3, the ratio of active Protein A modified on the PVDF-g-PAA-PrA membrane would be higher than that of the PES-g-PAA-PrA membrane.

As a recent related to the study of fabricating functional polymers, Starke *et al.* [32] have introduced a technique for covalent immobilization of trypsin on hydrophilic PVDF and PES membranes both with $0.22 \mu\text{m}$ pores using electron beam irradiation (150 kGy). Comparing the trypsin concentration

and activity of these immobilized membranes, the PES membrane showed the higher concentration of $3.48 \mu\text{g}\cdot\text{cm}^{-2}$ and an activity of $0.49 \text{ nmol}\cdot\text{min}^{-1}$ in the case of the PVDF membrane ($2.46 \mu\text{g}\cdot\text{cm}^{-2}$ and $0.36 \text{ nmol}\cdot\text{min}^{-1}$). However, the enzyme efficiency of trypsin, which was calculated as a quotient of the maximum released substrate per trypsin concentration, turned out to be $5.8 \text{ nmol}\cdot\text{cm}^2\cdot\mu\text{g}^{-1}$ of the PVDF membrane and was higher than the $3.2 \text{ nmol}\cdot\text{cm}^2\cdot\mu\text{g}^{-1}$ with the PES membrane described above.

In the results of the stability test, it was confirmed that the ligand densities were comparable, and Protein A was immobilized on the membrane surface rigidly. Castilho *et al.* [13] have reported that the ligand density of poly (vinyl alcohol)-coated membranes, which were the most suitable for IgG purification among the membranes tested in the work, was $4.66 \text{ mg protein A/mL membrane}$. In summary,

it was found that the PVDF/PES-g-PAA-PrA membranes were immobilized with Protein A rigidly, and had the properties of an affinity membrane.

3.4. Membrane morphology

It is important to understand whether the microporous structure of the membranes was retained after the plasma treatment and subsequent graft polymerization were conducted. Figure 6 shows the SEM images, obtained with a $3000\times$ magnification. Figures 6a–6c represent the untreated PVDF for pore sizes of 0.45 and $5.0 \mu\text{m}$, and the PES membrane for a pore size of $0.45 \mu\text{m}$, respectively. Figures 6d–6f show the plasma-treated membranes. The plasma-treated PVDF membrane fibers of the scaffolds for a pore size of $5.0 \mu\text{m}$, shown in Figure 6e, maintained the macrovoid formation as well as the untreated PVDF membrane. On the other hand, the plasma-

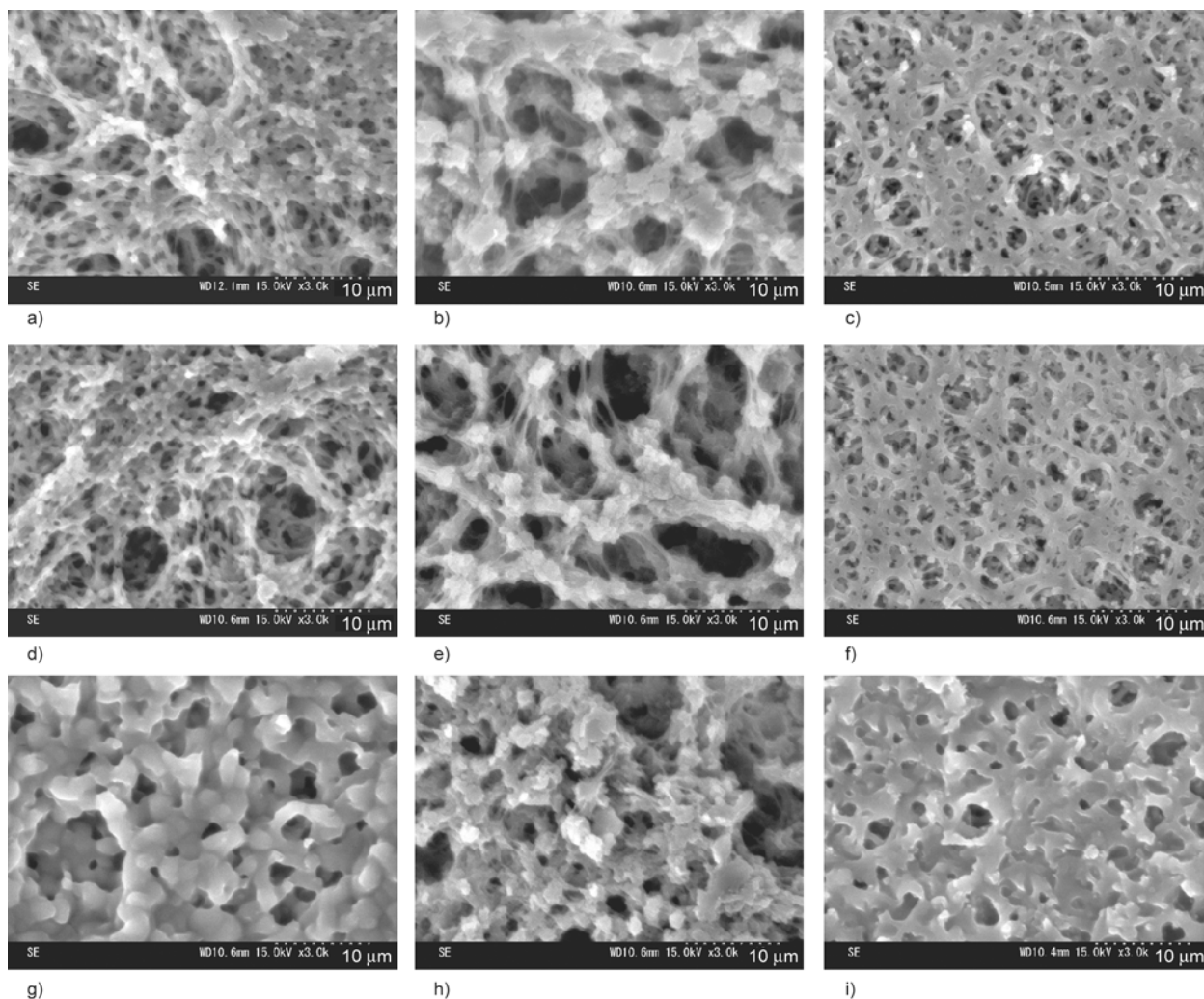


Figure 6. SEM images of PVDF (pore size $0.45 \mu\text{m}$ (a, d, g) and $5.0 \mu\text{m}$ (b, e, h)) and PES (c, f, i: pore size $0.45 \mu\text{m}$) membrane surfaces. Untreated (a, b, c), treated with argon plasma (d, e, f; treatment: $\pm 4.0 \text{ kVp-p}$, 180 s) and grafted with AA (g, h, i; treatment: 20% (v/v) AA, 70°C , 20 min). The argon plasma was treated from the above of these membranes.

treated PVDF and PES membrane fibers for a pore size of 0.45 μm , shown in Figures 6d and 6f, had grown slightly thicker than those for each untreated membrane surface. Figures 6g–6i show the PVDF/PES-g-PAA membranes. The PVDF/PES-g-PAA membranes with a pore size of 0.45 μm were densely modified with PAA. By contrast, the PVDF-g-PAA membrane for a pore size of 5.0 μm definitely retained the macrovoid formation (Figure 6h). These findings clearly indicate that it is effective to apply membranes with a pore size of 5.0 μm to maintain the high porosity and accessibility as affinity membranes.

4. Conclusions

We have described the characterization of Protein A-immobilized PVDF and PES membranes. The results of surface property tests on the membranes activated by argon plasma confirmed several functional groups such as hydroperoxide, sulfide and sulfo groups, and we proposed the activation mechanism on polymeric substrates. These findings suggest that the phenyl radical and radicals originating from hydroperoxide groups by thermal treatment are the important precursors to induce graft polymerization with AA on the PES membranes. The porosity of the membrane scaffold was preserved after the plasma treatment. The PVDF membrane for a pore size of 5.0 μm definitely retained the macrovoid formation after the graft polymerization. Protein A was successfully immobilized on the polymer-modified membranes. The adsorption capacities of the Protein A-immobilized membranes were determined and shown to be dependent on the pore size. The ligand density of the Protein A-immobilized PES membranes was approximately two times higher than that of the Protein A-immobilized PVDF membranes. Taken together, we conclude that the atmospheric pressure low-temperature plasma is an excellent tool for activation on the PVDF and PES membranes given the simplicity and effectiveness of this tool, and these polymers are candidates for affinity media for human IgG separation.

References

[1] Dargaville T. R., George G. A., Hill D. J. T., Whittaker A. K.: High energy radiation grafting of fluoropolymers. *Progress in Polymer Science*, **28**, 1355–1376 (2003). DOI: [10.1016/S0079-6700\(03\)00047-9](https://doi.org/10.1016/S0079-6700(03)00047-9)

[2] Johns K., Stead G.: Fluoroproducts – The extremophiles. *Journal of Fluorine Chemistry*, **104**, 5–18 (2000). DOI: [10.1016/S0022-1139\(00\)00251-7](https://doi.org/10.1016/S0022-1139(00)00251-7)

[3] Liu F., Hashim N. A., Liu Y., Abed M. R. M., Li K.: Progress in the production and modification of PVDF membranes. *Journal of Membrane Science*, **375**, 1–27 (2011). DOI: [10.1016/j.memsci.2011.03.014](https://doi.org/10.1016/j.memsci.2011.03.014)

[4] Kull K. R., Steen M. L., Fisher E. R.: Surface modification with nitrogen-containing plasmas to produce hydrophilic, low-fouling membranes. *Journal of Membrane Science*, **246**, 203–215 (2005). DOI: [10.1016/j.memsci.2004.08.019](https://doi.org/10.1016/j.memsci.2004.08.019)

[5] Zhu L-P., Zhu B-K., Xu L., Feng Y-X., Liu F., Xu Y-Y.: Corona-induced graft polymerization for surface modification of porous polyethersulfone membranes. *Applied Surface Science*, **253**, 6052–6059 (2007). DOI: [10.1016/j.apsusc.2007.01.004](https://doi.org/10.1016/j.apsusc.2007.01.004)

[6] Rahimpour A.: UV photo-grafting of hydrophilic monomers onto the surface of nano-porous PES membranes for improving surface properties. *Desalination*, **265**, 93–101 (2011). DOI: [10.1016/j.desal.2010.07.037](https://doi.org/10.1016/j.desal.2010.07.037)

[7] Steuck M. J.: Porous membrane having hydrophilic surface and process. U.S. Patent 4618533, USA (1986).

[8] Mezhirova M., Yeh E. B., Sale R.: Method for preparing hydrophilic polyethersulfone membrane. U.S. Patent 8425814 B2, USA (2013).

[9] van Reis R., Zydney A.: Bioprocess membrane technology. *Journal of Membrane Science*, **297**, 16–50 (2007). DOI: [10.1016/j.memsci.2007.02.045](https://doi.org/10.1016/j.memsci.2007.02.045)

[10] Nasef M. M., Güven O.: Radiation-grafted copolymers for separation and purification purposes: Status, challenges and future directions. *Progress in Polymer Science*, **37**, 1597–1656 (2012). DOI: [10.1016/j.progpolymsci.2012.07.004](https://doi.org/10.1016/j.progpolymsci.2012.07.004)

[11] Ulbricht M.: Advanced functional polymer membranes. *Polymer*, **47**, 2217–2262 (2006). DOI: [10.1016/j.polymer.2006.01.084](https://doi.org/10.1016/j.polymer.2006.01.084)

[12] Han M. J., Baroña G. N. B., Jung B.: Effect of surface charge on hydrophilically modified poly(vinylidene fluoride) membrane for microfiltration. *Desalination*, **270**, 76–83 (2011). DOI: [10.1016/j.desal.2010.11.024](https://doi.org/10.1016/j.desal.2010.11.024)

[13] Castilho L. R., Deckwer W-D., Anspach F. B.: Influence of matrix activation and polymer coating on the purification of human IgG with protein A affinity membranes. *Journal of Membrane Science*, **172**, 269–277 (2000). DOI: [10.1016/S0376-7388\(00\)00343-4](https://doi.org/10.1016/S0376-7388(00)00343-4)

[14] Shukla A. A., Hubbard B., Tressel T., Guhan S., Low D.: Downstream processing of monoclonal antibodies – Application of platform approaches. *Journal of Chromatography B*, **848**, 28–39 (2007). DOI: [10.1016/j.jchromb.2006.09.026](https://doi.org/10.1016/j.jchromb.2006.09.026)

- [15] Low D., O’Leary R., Pujar N. S.: Future of antibody purification. *Journal of Chromatography B*, **848**, 48–63 (2007).
DOI: [10.1016/j.jchromb.2006.10.033](https://doi.org/10.1016/j.jchromb.2006.10.033)
- [16] Chu P. K., Chen J. Y., Wang L. P., Huang N.: Plasma-surface modification of biomaterials. *Materials Science and Engineering R: Reports*, **36**, 143–206 (2002).
DOI: [10.1016/S0927-796X\(02\)00004-9](https://doi.org/10.1016/S0927-796X(02)00004-9)
- [17] Müller M., Oehr C.: Plasma aminofunctionalisation of PVDF microfiltration membranes: comparison of the in plasma modifications with a grafting method using ESCA and an amino-selective fluorescent probe. *Surface and Coatings Technology*, **116–119**, 802–807 (1999).
DOI: [10.1016/S0257-8972\(99\)00268-6](https://doi.org/10.1016/S0257-8972(99)00268-6)
- [18] Tendero C., Tixier C., Tristant P., Desmaison J., Leprince P.: Atmospheric pressure plasmas: A review. *Spectrochimica Acta Part B: Atomic Spectroscopy*, **61**, 2–30 (2006).
DOI: [10.1016/j.sab.2005.10.003](https://doi.org/10.1016/j.sab.2005.10.003)
- [19] Akashi N., Kuroda S.: Protein immobilization onto poly(vinylidene fluoride) microporous membranes activated by the atmospheric pressure low temperature plasma. *Polymer*, **55**, 2780–2791 (2014).
DOI: [10.1016/j.polymer.2014.04.029](https://doi.org/10.1016/j.polymer.2014.04.029)
- [20] Momtaz M., Dewez J. L., Marchand-Brynaert J.: Chemical reactivity assay and surface characterization of a poly(vinylidene fluoride) microfiltration membrane (“Durapore DVPP”). *Journal of Membrane Science*, **250**, 29–37 (2005).
DOI: [10.1016/j.memsci.2004.10.011](https://doi.org/10.1016/j.memsci.2004.10.011)
- [21] Persson K. M., Capannelli G., Bottino A., Trägårdh G.: Porosity and protein adsorption of four polymeric microfiltration membranes. *Journal of Membrane Science*, **76**, 61–71 (1993).
DOI: [10.1016/0376-7388\(93\)87005-V](https://doi.org/10.1016/0376-7388(93)87005-V)
- [22] Langmuir I.: The adsorption of gases on plane surfaces of glass, mica and platinum. *Journal of the American Chemical Society*, **40**, 1361–1403 (1918).
DOI: [10.1021/ja02242a004](https://doi.org/10.1021/ja02242a004)
- [23] Castilho L. R., Anspach F. B., Deckwer W-D.: Comparison of affinity membranes for the purification of immunoglobulins. *Journal of Membrane Science*, **207**, 253–264 (2002).
DOI: [10.1016/S0376-7388\(02\)00257-0](https://doi.org/10.1016/S0376-7388(02)00257-0)
- [24] Huse K., Böhme H-J., Scholz G. H.: Purification of antibodies by affinity chromatography. *Journal of Biochemical and Biophysical Methods*, **51**, 217–231 (2002).
DOI: [10.1016/S0165-022X\(02\)00017-9](https://doi.org/10.1016/S0165-022X(02)00017-9)
- [25] Hidzir N. M., Hill D. J. T., Taran E., Martin D., Grøndahl L.: Argon plasma treatment-induced grafting of acrylic acid onto expanded poly(tetrafluoroethylene) membranes. *Polymer*, **54**, 6536–6546 (2013).
DOI: [10.1016/j.polymer.2013.10.003](https://doi.org/10.1016/j.polymer.2013.10.003)
- [26] Lee Y. M., Shim J. K.: Plasma surface graft of acrylic acid onto a porous poly(vinylidene fluoride) membrane and its riboflavin permeation. *Journal of Applied Polymer Science*, **61**, 1245–1250 (1996).
DOI: [10.1002/\(SICI\)1097-4628\(19960822\)61:8<1245::AID-APP2>3.0.CO;2-K](https://doi.org/10.1002/(SICI)1097-4628(19960822)61:8<1245::AID-APP2>3.0.CO;2-K)
- [27] Huang F. L., Wang Q. Q., Wei Q. F., Gao W. D., Shou H. Y., Jiang S. D.: Dynamic wettability and contact angles of poly(vinylidene fluoride) nanofiber membranes grafted with acrylic acid. *Express Polymer Letters*, **4**, 551–558 (2010).
DOI: [10.3144/expresspolymlett.2010.69](https://doi.org/10.3144/expresspolymlett.2010.69)
- [28] Wavhal D. S., Fisher E. R.: Hydrophilic modification of polyethersulfone membranes by low temperature plasma-induced graft polymerization. *Journal of Membrane Science*, **209**, 255–269 (2002).
DOI: [10.1016/S0376-7388\(02\)00352-6](https://doi.org/10.1016/S0376-7388(02)00352-6)
- [29] Beeskow T. C., Kusharyoto W., Anspach F. B., Kroner K. H., Deckwer W-D.: Surface modification of microporous polyamide membranes with hydroxyethyl cellulose and their application as affinity membranes. *Journal of Chromatography A*, **715**, 49–65 (1995).
DOI: [10.1016/0021-9673\(95\)00540-4](https://doi.org/10.1016/0021-9673(95)00540-4)
- [30] Sun J., Wu L.: Polyether sulfone/hydroxyapatite mixed matrix membranes for protein purification. *Applied Surface Science*, **308**, 155–160 (2014).
DOI: [10.1016/j.apsusc.2014.04.123](https://doi.org/10.1016/j.apsusc.2014.04.123)
- [31] Saufi S. M., Fee C. J.: Mixed matrix membrane chromatography based on hydrophobic interaction for whey protein fractionation. *Journal of Membrane Science*, **444**, 157–163 (2013).
DOI: [10.1016/j.memsci.2013.05.007](https://doi.org/10.1016/j.memsci.2013.05.007)
- [32] Starke S., Went M., Prager A., Schulze A.: A novel electron beam-based method for the immobilization of trypsin on poly(ethersulfone) and poly(vinylidene fluoride) membranes. *Reactive and Functional Polymers*, **73**, 698–702 (2013).
DOI: [10.1016/j.reactfunctpolym.2013.02.013](https://doi.org/10.1016/j.reactfunctpolym.2013.02.013)

Thermo-stabilized, porous polyimide microspheres prepared from nanosized SiO₂ templating via *in situ* polymerization

M. Q. Liu, J. P. Duan, X. Z. Shi, J. J. Lu*, W. Huang

Key Laboratory of Coal Science and Technology (Taiyuan University of Technology), Ministry of Education and Shanxi Province, 79 YingZe West Street, 030024 Taiyuan, P. R. China

Received 4 June 2014; accepted in revised form 29 July 2014

Abstract. In this article, we addressed a feasible and versatile method of the fabrication of porous polyimide microspheres presenting excellent heat resistance. The preparation process consisted of two steps. Firstly, a novel polyimide/nano-silica composite microsphere was prepared via the self-assembly structures of poly(amic acid) (PAA, precursor of PI)/nanosized SiO₂ blends after *in situ* polymerization, following the two-steps imidization. Subsequently, the encapsulated nanoparticles were etched away by hydrofluoric acid treatment, giving rise to the pores. It is found the composite structure of PI/SiO₂ is a precondition of the formation of nanoporous structures, furthermore, the morphology of the resultant pore could be relatively tuned by changing the content and initial morphology of silica nano-particles trapped into PI matrix. The thermal properties of the synthesized PI porous spheres were studied, indicating that the introduction of nanopores could not effectively influence the thermal stabilities of PI microspheres. Moreover, the fabrication technique described here may be extended to other porous polymer systems.

Keywords: thermal properties, porous polyimide, microspheres, template, self-assembled composites

1. Introduction

In the last decades, owing to several special added-value applications in the area of catalysts, separation, chromatographic carriers, adsorbents, low-dielectric fillers, storage and deliver carriers for drugs, phonics crystals, nanoelectronics, or biotechnology [1–4], porous polymer materials, especially spherical ones, have been the hotspot of active study area in the development of new materials and some of them have been shown to be of practical use. Herein, an excellent porous polymer matrix should satisfy a variety of requirements, such as desirable thermal stability, chemical resistance and high modulus to support the void structure.

Polyimide (PI) is considered as the most promising candidates that could satisfy the above requirements with high thermal stability, good mechanical properties, excellent adhesion properties and out-

standing dimensional stability [5–7]. Up to now, several studies have been contributed to the preparation of well-defined porous PIs, such as PI membranes and PI foams; however, few reports have focused on preparing porous PI microspheres. Among those methods, reprecipitation method and thermal decomposition of the labile component are two of the most widely used techniques. Kasai *et al.* [8] proposed a route to fabricate porous PI nano-particles involving the use of LiCl, polymeric porogens (poly(acrylic acid) [9, 10], poly(vinyl alcohol) [9], poly(methyl methacrylate) [11], polyvinylpyrrolidone and polyelectrolyte [12]) as porogens. They investigated the effect of the porogen species and the reprecipitation conditions on the porous structures of the PI nano-particles. Unfortunately, the method they established requires precise control over the processing conditions, and cannot be employed for mass production

*Corresponding author, e-mail: lujianjunktz@tyut.edu.cn
© BME-PT

of porous particles. Besides, the final nanopore structure is still superficial, and it seems difficult to control the pore size and/or the pore number. Additionally, another alternative approach has been employed to fabricate meso- and macro-porous polymer materials using block copolymers that have two or more chemically immiscible blocks covalently linked together (e.g. the IBM Almaden Research Center, 1990s [13–15]; Chung *et al.* [16] (2006); Olson *et al.*, [17] (2008); Wu *et al.*, [4] (2012)). In these studies, the morphological structure of porous PI was determined by the initial morphology of the microphase separated structures of the copolyimides [17]. But the decomposition technique could plasticize the PI and generate the chain mobility during the pore formation, which made the pores collapse, particularly when the processing temperature is too close to the softening temperature (the minimum temperature of glass transition) of the PIs [18, 19]. Furthermore, thermal degradation is adverse to the molecular weight and certain critical mechanical properties.

Based on their contribution and theoretical support on the preparation of porous PI spheres, we attempted to introduce a simple and reproducible approach to prepare porous PI micro-particles using nano-silica particles as inorganic template. Through the typical self-assembly structures of poly(amic acid) (PAA, precursor of PI)/nano-SiO₂ sol blends, nano-porous PI spheres could be obtained after the removal of the silica component. Compared to the above method, the key advantage of the method lies in the mechanical and thermal properties of resultant porous PI spheres are little influenced and prevent the collapse of the porous structure during thermolysis. Furthermore, in this way, the whole process is easily controlled and applicable for mass production of porous PI particles, moreover, the pore size and pore struc-

ture of the porous polyimide spheres could be relatively controlled by adjusting the content and size of silica [20, 21]. The overview of the synthesis of the porous PMDA-ODA PI microspheres was shown in Figure 1.

2. Experimental procedures

2.1. Materials

4, 4'-diaminodiphenyl ether (ODA, CP) and pyromellitic dianhydride (PMDA, CP) were supplied by Aladdin Industrial Corporation and used with grinding and without further purification. Acetic anhydride (Ac₂O, dehydrating agent, AR), pyridine (catalyst, AR), N, N-Dimethylformamide (DMF, AR), Paraffin Liquid (LP, CP), hydrofluoric acid (HF, 40%, AR) and other solvents were purchased from Tianjin Kemiou Chemical Reagent Co., Ltd, China. Surfactants (Span 85 and Tween 80, CP) were obtained from Aladdin Industrial Corporation and dried at 80°C in a vacuum oven over night. Silica sol (JN-40, 100 nm, $\rho_{\text{SiO}_2} = 1.2 \text{ g/cm}^3$, pH = 8–10) and γ -glycidloxypropyltrimethoxysilane (GOTMS) were industrial grade reagent from Shandong Baxter new materials Co., Ltd and used as received.

2.2. Preparation of the PI/SiO₂ composite microspheres

2.0 mL GOTMS, in volumetric amount, was suspended in 20 mL SiO₂ sol with ultrasonic agitation. Subsequently, the mixed solution was stirred for 2 h at 40°C. Then, the GOTMS-stabilized silica sol was stored in room temperature for use.

In a 100 mL flask, 0.5000 g of ODA was dissolved in 15 mL of DMF solution with agitation at room temperature. Then the ODA dissolved completely, 0.5555 g of PMDA (1:1.02 molar ratio) was introduced into the solution in increments. After 15 min, 3.5 mL of the GOTMS-stabilized silica sol was added dropwise to the stirring mixture in batches. After magnetic agitation for 1 h and ultrasonic dispersion for 2 h, the reaction mixture was further stirred for 48 hours at room temperature to yield a homogeneous PAA/Si solution. Then the homogeneous PAA/Si solution was dispersed dropwise into 60 mL of vigorously stirred paraffin liquid containing 11.25 mL of surfactants ($V_{\text{span85}}:V_{\text{tween80}} = 2:1$), following by stirring over 2 h. Subsequently, a mixture of pyridine and Ac₂O (1:1, molar ratio) was added dropwise into the above emulsion system. After 2 h, the chemically imidized solid particulate product was

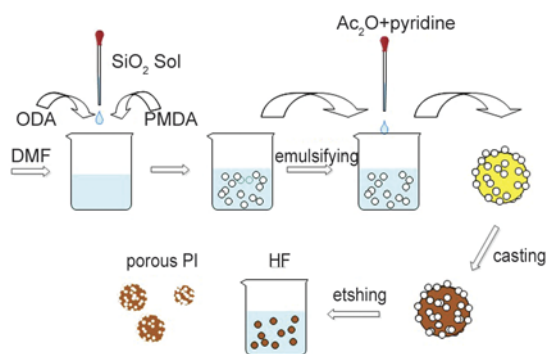


Figure 1. Overview of the synthesis of the porous PMDA-ODA PI microspheres

extracted by centrifugal separation and washed several times with petroleum ether and acetone to purify by removing any unreacted monomers and surfactants. Immediately following this, the solid particulate was placed in an air circulating oven with the curing procedure: 80°C (for 2 h), 120°C (for 2 h), 160°C (for 2 h), 200°C (for 2 h), 240°C (for 4 h), 280°C (for 4 h), 320°C (for 2 h).

2.3. Preparation of the porous PI microspheres

The detached PI/SiO₂ composite spheres were immersed in hydrofluoric acid solution with concentration of 25 wt% to remove the encapsulated silica particles. The etched spheres were collected by filtration, washed with distilled water to neutral, and dried under vacuum for 5 h at 200°C to remove traces

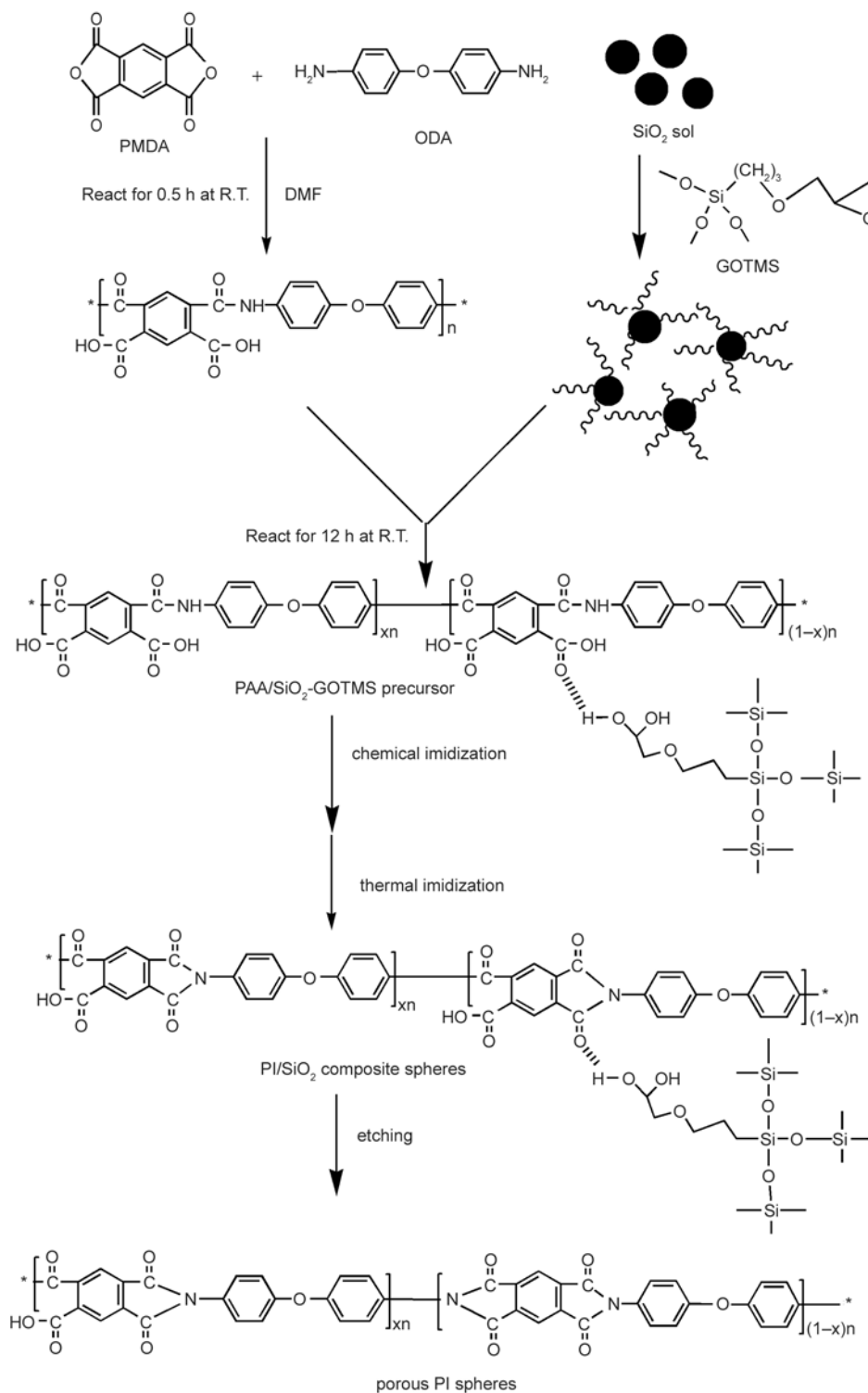


Figure 2. Reaction scheme for preparing the porous polyimide microspheres

of water. The porous PI microspheres were obtained. The typical reaction scheme for preparation the porous PMDA-ODA PI microspheres were presented in Figure 2.

2.4. Characterization

Chemical structure analysis was performed with a Bruker FT-IR Spectrometer model Equinox-55, USA. The changes of the characteristic absorption bands and corresponding functional groups were analyzed. Surface morphology characterization was evaluated using a FEI Navo Nano SEM-430 (FEI-SEM) at accelerating of 20 kV. The TGA instrument model Netzsch STA 409C under nitrogen at a heating rate of 10°C/min from room temperature to 900°C was used to characterize the differences in the thermal stability of the three type spheres.

3. Results and discussion

3.1. Chemical structure analysis

Previously, our laboratory research group prepared pure PI microspheres with a high solid content in a non-aqueous emulsion. Analogously, the porous spheres were obtained in the manner as mentioned in the experimental chapter. FT-IR was used to evaluate the presence of silica in the composite spheres and disappearance in the porous spheres. The FT-IR spectra of pure PI (Figure 3a), PI/SiO₂ (Figure 3b) and porous PI (Figure 3c) are illustrated in Figure 3. As shown in the obtained spectra, the characteristic imide group stretching vibrations were observed at 1721, 1777 cm⁻¹ (stretching vibration of cyclic C=O), 1373 cm⁻¹ (C–N stretching vibration) and 723 cm⁻¹ (bending vibration of C=O), which confirmed the complete conversion of the PAA precursor to PI and suggested they possessed of the same chemical basic

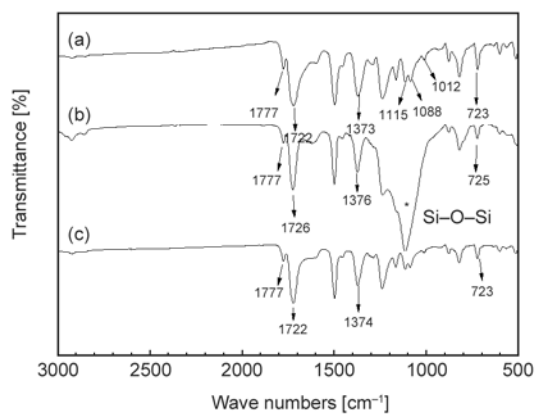


Figure 3. FT-IR spectra of the resulted PI spheres: (a) pure PI, (b) PI/SiO₂ composites, (c) porous PI

structure. Whereas, there were also obvious differences among the spectra (as shown in spectra by * marks). For example, the wavenumbers from 1000 to 1100 cm⁻¹ were attributed to typical absorption bands for Si–O–Si network vibrations derived silica, overlapping with absorption stretches associated with the in-plane C–H bending vibration band present in the 1080–1090 cm⁻¹ region, and the weak C–H peaks derived from GOTMS occurred in the 2867–2925 cm⁻¹ range in Figure 3b. Interestingly, it could be easily seen that the wavenumber of 1722 cm⁻¹ (C=O symmetric stretching) shift to higher frequencies at 1726 cm⁻¹, which was connected with change of the force constant, implying that there existed a few chemical bonds between organic molecules PI with functional groups such as carbonyl and ether bond and inorganic ingredient SiO₂ comprising a few hydroxyl groups. On the other hand, the coupling agent (GOTMS) also supplied many physical and chemical cross-linking points between the two phases, producing an increase of inter-chain interactions and ultimately higher frequencies. In Figure 3c, the spectra of porous PI is similar to the pure ones, and the disappearance corresponding to the Si–O–Si stretching band, ranging from 1000–1100 cm⁻¹, revealed the presence of only polyimide phase in porous spheres, and unveiled that the silica had been removed completely from the PI matrix and the HF chemical treatment did not affect the chemical structure of PI.

3.2. Microstructure analysis

Prior to discussion, the porous PI spheres were prepared successfully from nano-silica templating via *in situ* polymerization. SEM was performed to give details on the morphological changes of the various PI spheres. For the pure PI spheres (Figure 4a, 4b), they appear to be spherical perfectly with a smooth and dense surface and a narrow size distribution. Figure 4c, 4d represent a self-assembly composite spheres. It is noticed that the composites exhibit nearly fractal with the bumpy surface and non-uniform size. The amount of SiO₂ particles on the PI spheres obtained did not change after further product purification, in which the product were washed in petroleum ether and acetone under ultrasonic conditions. It can be seen that a large number of inorganic particles are deposited throughout outer surface of the PI microspheres (Figure 4d). Herein, only a small part volume of silica particles chemically

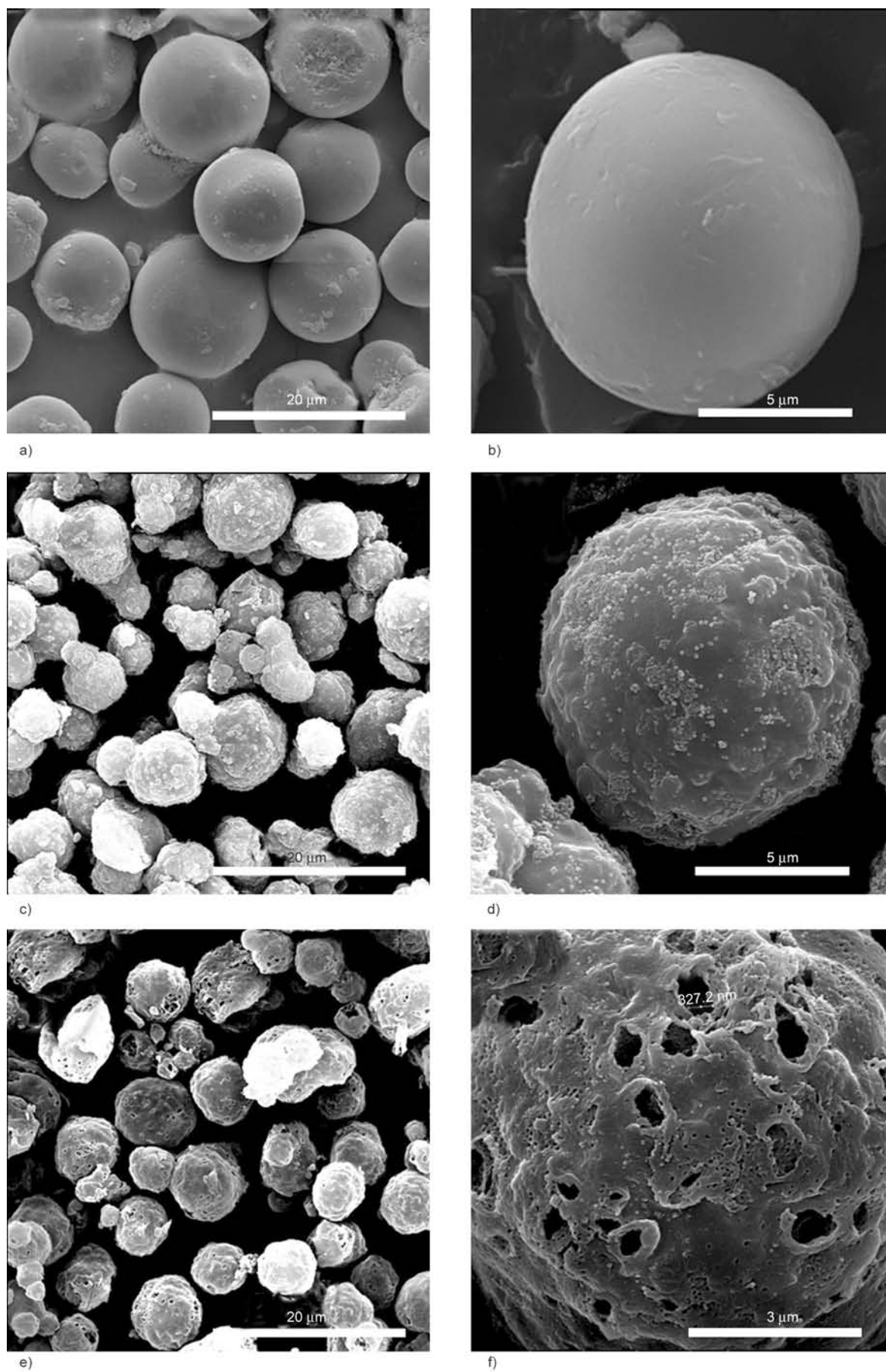


Figure 4. SEM images of the resulted PI spheres: (a) and (b) pure PI, (c) and (d) PI/SiO₂ composites, (e) and (f) porous PI

grafted to the organic phase exposed on the surface of PI spheres. In addition, a few granular aggregates derived from agglomeration of nano-particles occurred on the surface of composite spheres. The self-assembled PI/SiO₂ composite spheres were etched by HF acid to obtain the porous PI structure (Figure 4e, 4f). Compared to the composite spheres, the inorganic domains disappear and shape of spherical structure are conformed to be unchanged before and after the etching process, again indicating that HF etching have little influence on the structure of PI domains. Here, template method was applied to replace traditional thermal decomposition technique to prevent the collapse of the pore structure during thermolysis at the softening temperature. Because the size and distribution of pores strongly depended on the morphology of silica particles in PI matrix, estimated from the SEM overview, the resulted pores are randomly distributed and the average size locates approximately in the range of 70–100 nm and is consistent with the morphology of SiO₂ (Figure 4f). Interestingly, some meso- and macro- pores caused by the agglomeration of the nano-SiO₂ that are opening at the external surface of the PI spheres. Thus, much effort should be also put into attempt to develop the miscibility of the two phases with reducing the agglomeration of the inorganic particle, moreover, improve the uniformity of the pore distribution and size.

These phenomena could be explained as follows: During the process of the chemical imidization, the PI chains twisted, encapsulated the whole SiO₂ par-

ticles, dissolved out gradually and formed the composites. In preparing composite process, the functional groups of the GOTMS provided the bond link between the inorganic domains SiO₂ network and the phase PI matrix, leading to the formation of a considerable fine interconnected network system [22]. Furthermore, because the solubility of PI in DMF decreased rapidly, the small part of inorganic particles has not been trapped into the organic phase, giving rise to the demi-exposition of silica particles. Meanwhile, the compatibility between the two phases was low, leading to the intertwists between the PAA chains and silica three-dimensional networks were not enough dense compared to the intertwists among the single PAA chains. Moreover, as a result of nanometer effect, the inorganic particles of small size down to nanometer were easy to develop into very large ones through the condensation with neighboring particles, commonly, when the inorganic component content of PAA/Si solution was excessively high, the inorganic phase should present obvious agglomeration.

To further observe the variation of internal morphologies of the spheres, we searched for the broken spheres in SEM field-of-view (Figure 5a, 5b). We observed that the SiO₂ particles at the range of 70–100 nm appeared to be interconnected by the thin-wall of PI substrate to form groups of larger objects. The composites were acid treated to produce porous structure. Compared to the former, the interpenetrating network disappears and converts to a mass of disordered pores. Unfortunately, the collapse of

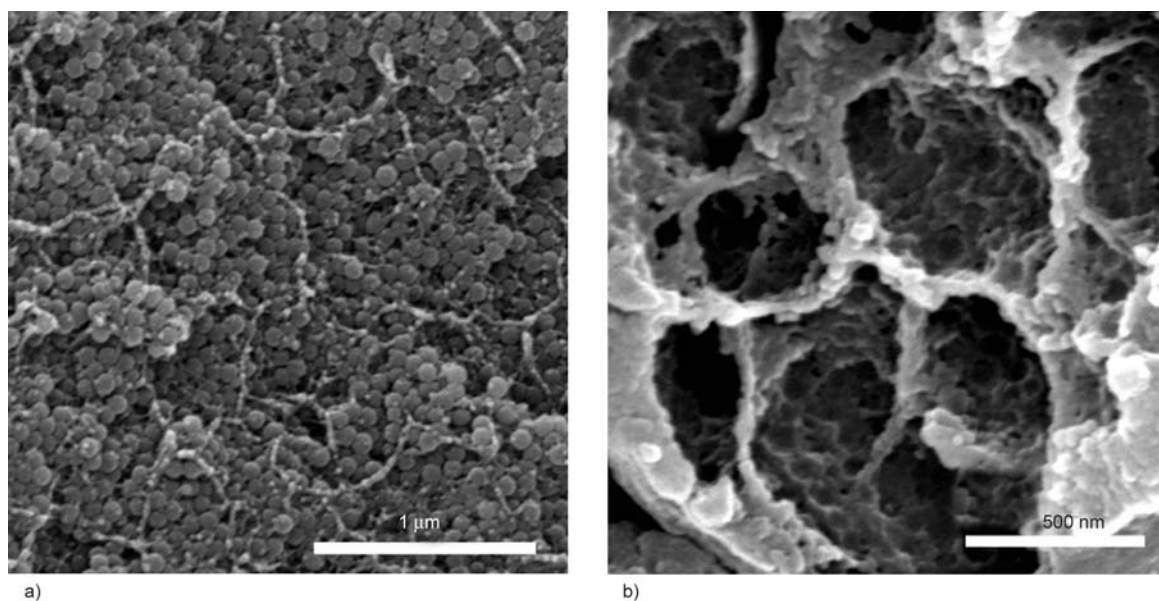


Figure 5. SEM images of the internal morphologies of the resulted PI spheres: (a) PI/SiO₂ composites, (b) porous PI

the thin-wall produced the macropores and may deteriorate the mechanical properties. Apparently, developing the dispersibility of the inorganic particles in PI matrix with reducing the agglomeration is the key of the method.

3.3. Thermal analysis

As shown in Figures 6 and 7, the thermal stabilities of the pure PI spheres, the PI/SiO₂ spheres and its corresponding porous PI spheres were compared by using TGA and DTGA curves in the range of 40–900°C. The thermal stabilities of the spheres are expressed by the temperature for 5 and 10% weight loss, and the temperature for maximum mass loss rate, $T_{5\%}$, $T_{10\%}$ and T_{max} , which are listed in Table 1. As expected, one may notice that the thermal stability of porous spheres presented less lower than the other ones. It is natural since the thermal stability of inorganic moiety is higher than organic resins, the inclusion of the inorganic component will enhance the thermal stability of polymer [23, 24]. Besides, when the inorganic component content was enough large, a duplex-continuous interpenetrating network

Table 1. Thermal stabilities of the three type spheres

Sample code	$T_d(5\%)$ [°C]	$T_d(10\%)$ [°C]	T_{max} [°C]	Char yield at 900°C [wt%]
(a)	499	566	601	48.11
(b)	499	552	569	73.97
(c)	455	519	562	52.49

had formed after *in situ* polymerization, hindering the movement of polymer molecules and enhancing the thermal conductivity. The factors all cooperated to increase the thermal decomposition temperature of the composites. However, the incorporation of pores will impair the regularity and the crystallization of the chain segments, and increase the free volume of polymer, which are adverse to the thermal stability of PI matrix. The two elements resulted in the lowest thermal stability of the three spheres. But, there was no apparent weight loss before 455°C for the porous PI, and until 562°C the obvious changes of weight loss were brought about. Therefore, the obtained porous PI spheres are still high heat resistance, being of central importance to the practical applications. Moreover, this conclusion unveiled that the HF etching process did not affect the backbones of polyimide, which was in good agreement with FT-IR results.

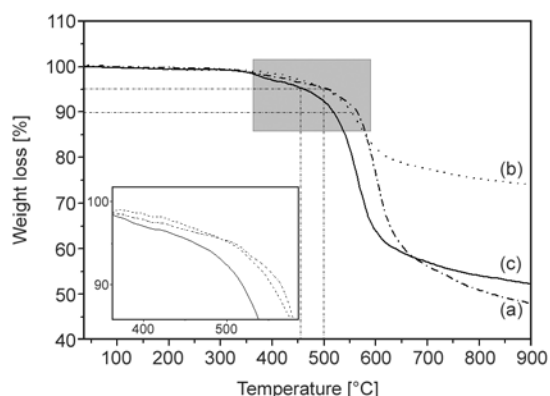


Figure 6. TGA curves of the resulted PI spheres: (a) pure PI, (b) PI/SiO₂ composites, (c) porous PI

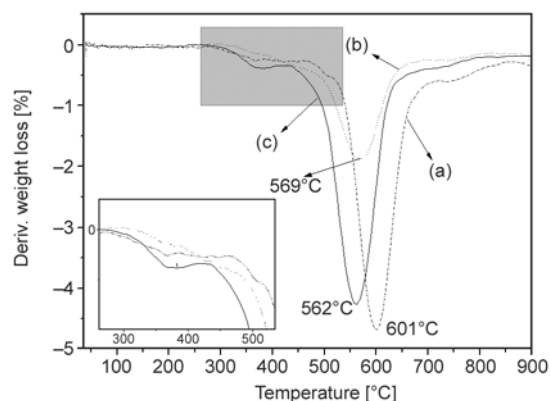


Figure 7. DTGA curves of the resulted PI spheres: (a) pure PI, (b) PI/SiO₂ composites, (c) porous PI

3.4. The mechanism for formation of the porous PI microspheres

On the basis of the above results, we audaciously propose a mechanism of formation for porous structures, which is a much more complicated process. Firstly, the uniform solution of PAA-DMF containing SiO₂ particles was obtained after polymerization, following by dispersing into Paraffin Liquid to form emulsion system. Immediately, most of the PAA and SiO₂ molecules gradually formed dispersion phase. Then the fine DMF droplets containing PAA and SiO₂ particles were initially generated in the Paraffin Liquid medium. Herein, the dispersibility of inorganic particles was a crucial condition for the uniformity of pore network. Secondly, upon the process of the chemical cyclization, the solubility of PI in DMF decreased rapidly, the PI chains bonded with nano-SiO₂ began to twist, dissolve out gradually, solidify and form composite spheres of PI and SiO₂. Finally, the discontinuous inorganic SiO₂ particles were eluted perfectly from composite system by the HF rinse procedure, providing porous PI microspheres with closed pore structure.

Indeed, the dispersibility of inorganic particles is influenced by the complicated interactions, the rate of solidification and the inorganic particles content of composites, which should determine directly the resulted pore structure. It is well known that on the surface of silica particles, there exist many hydroxyls which could have strong hydrogen bonding interaction with carboxyl of PAA, moreover, the coupling agent also provide more bond sites between the PAA chains and SiO₂ network. The PI/SiO₂ composite spheres resulted from a balance between the varied interactions and the diffusion of the molecules, namely, after chemically imidization, most of inorganic particles were complexed into organic phase and the composites were obtained. By the removal of SiO₂, the PI porous structures having clear interfaces were formed successfully. Nevertheless, the compatibility of two phases is the most dominant factor affecting the fabrication of the porous PI micro-particles. Furthermore, considering the diversity of polymers, we suspect that it will be suited to prepare other porous polymer micro-particles possessing anomalous structures through judicious selection of the combination of organic polymer and the inorganic components.

4. Conclusions

In conclusion, a simple methodology of the fabrication of porous polyimide microspheres with pore size in the nanometer regime was presented. This is a novel, versatile paradigm in the production of porous PI spheres with high heat resistance, based on a self-assembly composite structure comprised of a polyimide as the matrix or dominant phase with silica as the templates, which have been designed primarily via *in situ* polymerization route. Upon a HF etching treatment, the silica particles tripped into the matrix were released, leaving the pores in the range of 70–100 nm. The resultant porous morphology of the as-synthesized PI spheres could be involved in variety of factors (e.g. the initial morphology and weight content of the silica, the complicated interactions in two phases). The prepared thermo-stabilized, porous PI microspheres make it promising in the high temperature resistance of microelectronics. Furthermore, the various inorganic particles, in this way, could be self-assembled into versatile polymer matrix, allowing the preparation of the multifarious porous polymer materials not only porous polyimide materials.

Acknowledgements

Financial support from the Shanxi Provincial Scientific research project fund (20130321026-05) is highly appreciated.

References

- [1] Wang H., Shi L., Yan T., Zhang J., Zhong Q., Zhang D.: Design of graphene-coated hollow mesoporous carbon spheres as high performance electrodes for capacitive deionization. *Journal of Materials Chemistry A*, **2**, 4739–4750 (2014). DOI: [10.1039/C3TA15152B](https://doi.org/10.1039/C3TA15152B)
- [2] Zhang S., Chen L., Zhou S., Zhao D., Wu L.: Facile synthesis of hierarchically ordered porous carbon via *in situ* self-assembly of colloidal polymer and silica spheres and its use as a catalyst support. *Chemistry of Materials*, **22**, 3433–3440 (2010). DOI: [10.1021/cm1002274](https://doi.org/10.1021/cm1002274)
- [3] Zhang S., Zhou S., You B., Wu L.: Fabrication of ordered porous polymer film via a one-step strategy and its formation mechanism. *Macromolecules*, **42**, 3591–3597 (2009). DOI: [10.1021/ma900055f](https://doi.org/10.1021/ma900055f)
- [4] Wu D., Xu F., Sun B., Fu R., He H., Matyjaszewski K.: Design and preparation of porous polymers. *Chemical Reviews*, **112**, 3959–4015 (2012). DOI: [10.1021/cr200440z](https://doi.org/10.1021/cr200440z)
- [5] Bartolotta A., Calandra P.: Indication of local phase separation in polyimide/silica hybrid polymers. *Macromolecular Chemistry and Physics*, **211**, 1784–1792 (2010). DOI: [10.1002/macp.201000110](https://doi.org/10.1002/macp.201000110)
- [6] Ragosta G., Musto P.: Polyimide/silica hybrids via the sol-gel route: High performance materials for the new technological challenges. *Express Polymer Letters*, **3**, 413–428 (2009). DOI: [10.3144/expresspolymlett.2009.51](https://doi.org/10.3144/expresspolymlett.2009.51)
- [7] Hsu S-C., Whang W-T., Hung C-H., Chiang P-C., Hsiao Y-N.: Effect of the polyimide structure and ZnO concentration on the morphology and characteristics of polyimide/ZnO nanohybrid films. *Macromolecular Chemistry and Physics*, **206**, 291–298 (2005). DOI: [10.1002/macp.200400326](https://doi.org/10.1002/macp.200400326)
- [8] Kasai H., Mitsui H., Zhao G., Ishizaka T., Suzuki M., Oikawa H., Nakanishi H.: Fabrication of porous nanoscale polyimide structures. *Chemistry Letters*, **37**, 1056–1057 (2008). DOI: [10.1246/cl.2008.1056](https://doi.org/10.1246/cl.2008.1056)
- [9] Zhao G., Ishizaka T., Kasai H., Oikawa H., Nakanishi H.: Fabrication of unique porous polyimide nanoparticles using a reprecipitation method. *Chemistry of Materials*, **19**, 1901–1905 (2007). DOI: [10.1021/cm062709w](https://doi.org/10.1021/cm062709w)
- [10] Zhao G., Ishizaka T., Kasai H., Nakanishi H., Oikawa H.: Introducing porosity into polyimide nanoparticles. *Journal of Nanoscience and Nanotechnology*, **8**, 3171–3175 (2007). DOI: [10.1166/jnn.2008.074](https://doi.org/10.1166/jnn.2008.074)

- [11] Zhao G., Ishizaka T., Kasai H., Hasegawa M., Furukawa T., Nakanishi H., Oikawa H.: Ultralow-dielectric-constant films prepared from hollow polyimide nanoparticles possessing controllable core sizes. *Chemistry of Materials*, **21**, 419–424 (2009).
DOI: [10.1021/cm802989u](https://doi.org/10.1021/cm802989u)
- [12] Zhao G., Ishizaka T., Kasai H., Hasegawa M., Nakanishi H., Oikawa H.: Using a polyelectrolyte to fabricate porous polyimide nanoparticles with crater-like pores. *Polymers for Advanced Technologies*, **20**, 43–47 (2009).
DOI: [10.1002/pat.1278](https://doi.org/10.1002/pat.1278)
- [13] Hedrick J., Labadie J., Russell T., Hofer D., Wakharkar V.: High temperature polymer foams. *Polymer*, **34**, 4717–4726 (1993).
DOI: [10.1016/0032-3861\(93\)90707-H](https://doi.org/10.1016/0032-3861(93)90707-H)
- [14] Hedrick J. L., Hawker C. J., DiPietro R., Jerome R., Charlier Y.: The use of styrenic copolymers to generate polyimide nanofoams. *Polymer*, **36**, 4855–4866 (1995).
DOI: [10.1016/0032-3861\(95\)99303-C](https://doi.org/10.1016/0032-3861(95)99303-C)
- [15] Hedrick J. L., Carter K. R., Richter R., Miller R. D., Russell T. P., Flores V., Meccerreyes D., Dubois P., Jérôme R.: Polyimide nanofoams from aliphatic polyester-based copolymers. *Chemistry of Materials*, **10**, 39–49 (1998).
DOI: [10.1021/cm960523z](https://doi.org/10.1021/cm960523z)
- [16] Chung C-M., Lee J-H., Cho S-Y., Kim J-G., Moon S-Y.: Preparation of porous thin films of a partially aliphatic polyimide. *Journal of Applied Polymer Science*, **101**, 532–538 (2006).
DOI: [10.1002/app.23360](https://doi.org/10.1002/app.23360)
- [17] Olson D. A., Chen L., Hillmyer M. A.: Templating nanoporous polymers with ordered block copolymers. *Chemistry of Materials*, **20**, 869–890 (2008).
DOI: [10.1021/cm702239k](https://doi.org/10.1021/cm702239k)
- [18] Lee J. Y., Lee S. T.: Laser-induced thermal imaging of polymer light-emitting materials on poly(3,4-ethylenedioxythiophene): Silane hole-transport layer. *Advanced Materials*, **16**, 51–54 (2004).
DOI: [10.1002/adma.200305699](https://doi.org/10.1002/adma.200305699)
- [19] Chen Y., Wang W., Yu W., Yuan Z., Kang E-T., Neoh K-G., Krauter B., Greiner A.: Nanoporous low- κ polyimide films via poly(amic acid)s with grafted poly(ethylene glycol) side chains from a reversible addition–fragmentation chain-transfer-mediated process. *Advanced Functional Materials*, **14**, 471–478 (2004).
DOI: [10.1002/adfm.200305050](https://doi.org/10.1002/adfm.200305050)
- [20] Jiang L., Liu J., Wu D., Li H., Jin R.: A methodology for the preparation of nanoporous polyimide films with low dielectric constants. *Thin Solid Films*, **510**, 241–246 (2006).
DOI: [10.1016/j.tsf.2005.12.216](https://doi.org/10.1016/j.tsf.2005.12.216)
- [21] Wang C., Wang Q., Wang T.: Simple method for preparation of porous polyimide film with an ordered surface based on *in situ* self-assembly of polyamic acid and silica microspheres. *Langmuir*, **26**, 18357–18361 (2010).
DOI: [10.1021/la103473u](https://doi.org/10.1021/la103473u)
- [22] Liu Q-P., Gao L-X., Gao Z-W., Yang L.: Preparation and characterization of polyimide/silica nanocomposite spheres. *Materials Letters*, **61**, 4456–4458 (2007).
DOI: [10.1016/j.matlet.2007.02.022](https://doi.org/10.1016/j.matlet.2007.02.022)
- [23] Ahmad Z., Mark J. E.: Polyimide–ceramic hybrid composites by the sol–gel route. *Chemistry of Materials*, **13**, 3320–3330 (2001).
DOI: [10.1021/cm010175n](https://doi.org/10.1021/cm010175n)
- [24] Shang X-Y., Zhu Z-K., Yin J., Ma X-D.: Compatibility of soluble polyimide/silica hybrids induced by a coupling agent. *Chemistry of Materials*, **14**, 71–77 (2002).
DOI: [10.1021/cm010088v](https://doi.org/10.1021/cm010088v)

Control of nanostructures generated in epoxy matrices blended with PMMA-*b*-PnBA-*b*-PMMA triblock copolymers

H. Kishi^{1*}, Y. Kunimitsu¹, Y. Nakashima¹, T. Abe¹, J. Imade¹, S. Oshita², Y. Morishita², M. Asada²

¹Graduate School of Engineering, University of Hyogo, 2167, Shosha, Himeji, 671-2201 Hyogo, Japan

²Kuraray Co. Ltd., 1-1-3, Otemachi, Chiyoda-ku, 100-8115 Tokyo, Japan

Received 22 May 2014; accepted in revised form 30 July 2014

Abstract. Stability of nanostructures of epoxy/acrylic triblock copolymer blends was studied. PMMA-*b*-PnBA-*b*-PMMA triblock copolymers (acrylic BCPs) having several compositions on the ratio of the block chains and the molecular weight were initially prepared and were blended with diglycidyl ether of bisphenol-A epoxy thermosets. The blends were cured using phenol novolac with tri phenyl phosphine (TPP) as the catalyst. Several nanostructures, such as spheres, cylinders, curved lamellae, were observed in the cured blends. The nanostructures were controlled by the molecular weight of the immiscible PnBA-block chain and the ratio of the PnBA in the blends. Moreover, the effect of the gel time to the nanostructures was examined by altering the trace amount of the TPP in the blends. The types of the nanostructures were almost kept irrespective of the gel time of the blends when the composition of the blends was maintained. This suggested the stability of the nanostructures of the epoxy/acrylic BCP blends made via the self-assembly mechanism, therefore a phase diagram of the cured blends was proposed.

Keywords: polymer blends and alloys, thermosets, nanomaterials, epoxy, block copolymer

1. Introduction

Epoxy thermosets are some of polymers widely used as structural materials and adhesives in many industries, such as the aerospace, automotive and electronics industries, for their reliable mechanical properties, high heat and solvent resistance. The distinguishing properties originate from the crosslinked chemical structure. However, the crosslinked structure tends to give low fracture toughness due to the restricted molecular motion of the polymer chains. Considerable effort to toughen the epoxy thermosets has been made in the past decades.

Relatively low crosslinked epoxy thermosets can be toughened by the incorporation of elastomer phases, but more highly crosslinked epoxy thermosets were difficult to toughen by the method [1–6]. Therefore, highly crosslinked epoxy polymer blends modified with engineering thermoplastic polymers have been

researched [7–11]. The improvement in toughness depended on the phase morphology of the epoxy polymer blends. The phase separation occurs during the reaction process from the initial homogeneous mixture of the epoxy/thermoplastic blends [12, 13]. The driving force of the ‘reaction-induced phase separation’ is the elevated free energy of the mixture by the increase in the molecular weight via the reaction of epoxies and curing agents [12–14]. The phase sizes of the ‘reaction-induced phase separation’ were often from sub-micrometers to tens of micrometers.

In the background, block copolymers (BCPs) have attracted attention as toughening modifiers for nanostructured epoxy blends in the past years [15–37]. It is well known that the BCPs consisting of chemically distinct block chains form nano-phase structures in self-assembly [38–40]. Hillmyer *et al.* [15]

*Corresponding author, e-mail: kishi@eng.u-hyogo.ac.jp

and Lipic *et al.* [16] first reported nanostructured epoxy blends with the amphiphilic BCPs. Poly (ethylene oxide)-*b*-poly (ethyl ethylene) (PEO-PEE) diblock copolymer and poly (ethylene oxide)-*b*-poly (ethylene-alt-propylene) (PEO-PEP) diblock copolymer [15, 16] were synthesized as modifiers for diglycidyl ether of bisphenol-A (DGEBA) type epoxy thermosets. Hexagonally-packed cylindrical core-shell nanostructures were formed in the epoxy matrix blended with the 25 wt% PEO-PEE diblock copolymer [15]. In addition, the nanostructure of the uncured blends (DGEBA/PEO-PEP) was investigated using small-angle X-ray scattering (SAXS). By increasing the BCP amounts, the body-centered cubic packed spheres were changed to hexagonally packed cylinders, gyroid, and lamellar structures [16]. In-situ SAXS was also examined for an epoxy/69 wt% PEO-PEP diblock copolymer blend using an aromatic amine hardener. The phase structure changed from a gyroid to a lamella structure during the cure process [16]. Moreover, the same group synthesized many kinds of BCPs having PEO block for the epoxy polymer blends. The blends gave several nanostructures, such as spherical micelles, worm-like micelles, and vesicles [17–22].

Ritzenthaler and coworkers [23, 24] studied epoxy/ABC triblock copolymer blends. ‘Raspberry-like’ (spheres-on-spheres) nanostructures were observed in the polystyrene-*b*-polybutadiene-*b*-poly (methyl methacrylate) triblock polymer (PS-PB-PMMA)/DGEBA blends cured with MCDEA (4,4’-methylene-bis-(3-chloro 2,6-diethyl-aniline)). The triblock copolymer having the increased PB segment showed ‘onion-like’ multilayered morphology in the DGEBA cured with MCDEA.

Nanostructured epoxy blends with polystyrene-*b*-polybutadiene (PS-PB) diblock copolymers were prepared by Serrano *et al.* [29]. The MCDEA-cured DGEBA/PS-PB diblock copolymer blends showed worm-like micelles and hexagonally-packed cylindrical micelles. The phase morphologies depended on the amount of the BCPs and the degree of epoxidation in the polybutadiene block.

In our previous study [30], poly (methyl methacrylate)-*b*-poly(n-butyl acrylate)-*b*-poly(methyl methacrylate) (PMMA-*b*-PnBA-*b*-PMMA) triblock copolymers (acrylic BCPs) were synthesized via living anionic polymerization. The acrylic BCPs were blended with the epoxy using a wide range of curing agents. Though aromatic amine (diamino diphenyl

sulphone), acid anhydride (methyl nadic anhydride) and anionic polymerization catalyst (tris-dimethyl amino methyl phenol) gave macro-phase separation in the cured epoxy blends, phenol novolac (PN)-cured epoxy/acrylic BCP blends gave nanostructures. Cylindrical micelles (both randomly-dispersed and regularly-arrayed) and spherical micelles were observed in the blends. The miscibility between the PMMA segments of the BCPs and the cured epoxy was a key factor to make the nanostructures in the blends. The fracture toughness of the epoxy/acrylic BCP blends having the nano-cylindrical structures was 2530 J/m². The toughness was twenty-fold compared to the unmodified epoxy thermoset.

In the literatures by Bates and coworkers [15, 16, 18, 20–22], nanostructures were generated via ‘self-assembly’ mechanism of epoxy/BCP blends. In other words, the nanostructures were pre-formed before the curing reaction of the blends, and were fixed by the network formation after the curing. On the other hand, Zheng and coworkers [31–34] showed that the nanostructures of the epoxy/BCP blends can be also generated via the ‘reaction-induced phase separation’. In this case, it is not required that BCPs generate the nanostructures in self-assembly prior to the curing reaction; all the BCPs may be miscible with the thermoset precursors [34]. The formation of the nanostructures is due to the phase separation of the thermoset-phobic blocks of the BCPs from the matrix blends in the curing process [34]. Recently, Romeo *et al.* [37] reported that the cure cycle determined the types of the nanostructures of a DGEBA/PS-*b*-PMMA BCP blend, in which the nanostructures were generated via ‘reaction-induced phase separation’. The difference of the mechanisms of the phase formation would have big effect on the stability of the nanostructures. Although various nanostructures were reported using many types of the epoxy/BCP blends, to the best of our knowledge, there are only limited literatures on the stability of the nanostructures in relation to the curing reaction rate. This is very important issue to be discussed in both scientific and industrial viewpoints.

The objective of the present study is twofold: (i) to find the key parameters to determine the nanostructures of the cured epoxy/acrylic BCP blends. The block composition and the molecular weight of the PMMA-*b*-PnBA-*b*-PMMA triblock copolymers were systematically controlled by living anionic poly-

merization, and the morphologies of the DGEBA blends were examined. (ii) to examine the effect of the reaction rate on the nanostructures using the each composition of the epoxy/acrylic BCP blends. From the results, the phase diagram of the epoxy/acrylic triblock copolymer blends will be proposed.

2. Experimental procedure

2.1. Materials

The epoxy thermoset used in this study was diglycidyl ether of bisphenol-A (DGEBA), jER828 (epoxy equivalent weight: 189 g/eq., provided by Mitsubishi Chemical Co. Ltd., Japan). Phenol novolac (PN, hydroxyl group equivalent weight: 105 g/eq., provided by Sumitomo Bakelite Co., Ltd., Japan) was utilized as the curing agent. Tri phenyl phosphine (TPP, produced by Tokyo Chemical Industry Co. Ltd., Japan) was applied as a catalyst with the PN. Several types of PMMA-*b*-PnBA-*b*-PMMA triblock copolymers (acrylic BCPs) were synthesized by living anionic polymerization (produced by Kuraray Co. Ltd., Japan), and were applied as the modifiers for the epoxy blends. The molecular weight of the acrylic BCPs and the composition (the ratio of the PnBA in the acrylic BCPs) were systematically controlled. The PnBA block chain is the segment which is immiscible with the PN-cured DGEBA type epoxy thermosets [30]. The characterization of the BCPs is shown in Table 1 in detail. Also, the chemical structure of the BCPs is shown in Figure 1.

Table 1. Weight-average molecular mass (M_w), PnBA content and polydispersity of PMMA-PnBA-PMMA triblock copolymers (BCPs)

No. of BCP	Molecular mass M_w	PnBA in BCP [wt%]	M_w/M_n
BCP50-6	64 000	50	1.19
BCP68-6	60 000	68	1.25
BCP77-7	72 000	77	1.19
BCP70-3	26 000	70	1.07
BCP69-13	132 000	69	1.31
BCP79-11	105 000	79	1.43

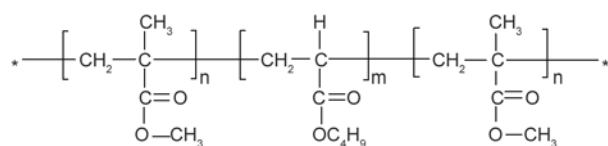


Figure 1. Chemical structure of PMMA-PnBA-PMMA triblock copolymers (BCPs)

2.2. Size exclusion chromatography

The molecular weight distributions of the BCPs were determined using size exclusion chromatography (SEC, PU-2080 HPLC system using JASCO-Borwin-GPC program), which was equipped with two connected columns of Shodex LF-804. Tetrahydrofuran (THF) was used as the solvent. The average molecular weights were calibrated by mono-dispersed polystyrene standards.

2.3. Preparation of cured thermosets

The DGEBA/acrylic BCP systems were cured by the following procedure. First, the BCP was mixed with the DGEBA at room temperature. The mixture was heated while being stirred in an oil bath at 200°C for 30 min in order to dissolve the BCP in the DGEBA. After the mixture was cooled to below 100°C, the stoichiometric quantities of PN and a small amount [0.05–2.0 parts per hundred parts of resin (DGEBA+PN): phr] of TPP were added to the mixture and degassed. The mixture was cast into a pre-treated mold with a release agent. The curing condition is shown in Table 2. The gel time was measured during the pre-curing step at 120°C for the thermoset compositions by using the method described in the section 2.5. After this procedure, the oven was switched off and the cured polymers were allowed to cool slowly to room temperature.

Table 2. Curing conditions and gel times of DGEBA/acrylic-BCP blends cured with PN (catalyzed by TPP)

Amount of TPP [phr]	Gel time [min]	Curing condition
2.0	5	120°C 2 h + 150°C 2 h
1.0	8	
0.5	15	
0.05	150	120°C 4 h + 150°C 2 h

2.4. Microscopic observation

2.4.1. Transmission Electron Microscopy (TEM)

Thin sections of the cured polymers were cryo-microtomed at –80°C. The setting thickness was 40–50 nm. The microtomed thin sections of the cured polymers were stained by vapor of RuO₄ and observed by a transmission electron microscope (TEM: HITACHI H-800NA, Japan) with 100 kV as the acceleration voltage.

2.5. Evaluation for gel time of the epoxy/BCP blend

The time dependencies of the viscoelastic properties (storage modulus: G' and loss modulus: G'') of the DGEBA/BCP/PN blends were evaluated by dynamic mechanical analysis (DMA) in shear mode between two parallel plates (Rheosol-G5000, UBM Co. LTD, Japan). The diameter of the parallel plates was 25 mm, and the gap between the two plates was 2.5 mm. The dynamic frequency was 1 Hz and the amplitude was 0.01° . The tests were conducted at 120°C . The gel time was defined at the time when the line of G' and the line of G'' intersected.

2.6. Glass transition temperature, T_g , measurement for BCPs

Glass transition temperatures of BCPs were determined using differential scanning calorimetry (DSC 6200, Seiko Instruments, Inc., Japan). Measurements were performed at a scanning rate of $40^\circ\text{C}/\text{minute}$. Mid-point T_g values were recorded.

2.7. Ultra small-angle X-ray scattering (USAXS)

In order to evaluate the phase separated structures of the cured epoxy/BCP blends, ultra small angle X-ray scattering (USAXS) measurements were conducted at the BL03XU beamline at SPring-8 (Hyogo, Japan) with the approval of JASRI (Proposal No. 2010B7206). The X-ray wavelength was 0.2 nm, and the distance between the sample and the detector (Imaging Plate) was ca. 6000 mm. The exposure time was 10 sec.

3. Results and discussion

3.1. Phase structures of cured epoxy/PMMA-PnBA-PMMA triblock copolymers

First, the effect of the ratio of PnBA in the BCPs was examined in terms of the nanostructures of the cured epoxy (DGEBA)/BCP blends. Three types of the BCPs (BCP50-6, BCP68-6, and BCP77-7) were compared as the modifiers for the epoxy blends. The PnBA ratios in the BCPs were 50, 68, and 77%, respectively. Figure 2 (10 wt% BCP in the blends) and Figure 3 (20 wt% BCP in the blends) show the phase structures (TEM photographs) of the DGEBA/BCP blends. As had been clarified in our previous paper, the relatively dark phases consist of the

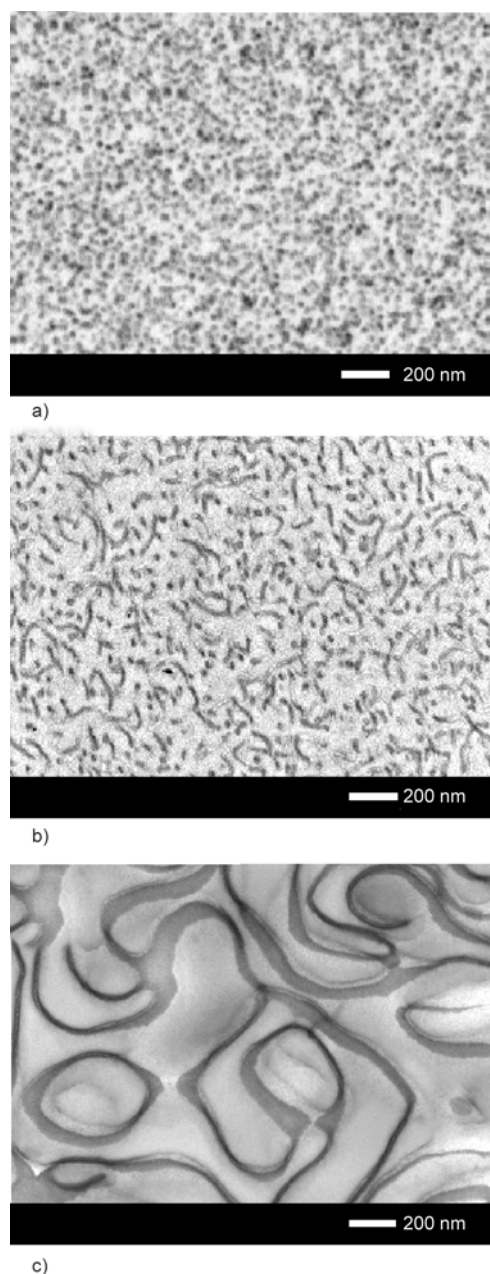


Figure 2. Effect of the PnBA content in the acrylic BCPs on the phase structures of DGEBA/10 wt% acrylic BCP blends cured with PN (catalyzed by 0.5 phr TPP): a) DGEBA/BCP50-6 (PnBA content in the BCP: 50 wt%), b) DGEBA/BCP68-6 (PnBA content in the BCP: 68 wt%), c) DGEBA/BCP77-7 (PnBA content in the BCP: 77 wt%)

PnBA stained by RuO_4 , and the bright matrix mainly consists of the epoxy thermoset [30].

The cured blends of the DGEBA/BCP50-6 (ie. 50% PnBA in the BCP) showed spherical nano-micelles composed of the PnBA, in both cases of the 10% BCP blend and the 20% BCP blend. The cured blends of the DGEBA/BCP68-6 (ie. 68% PnBA in the BCP) showed cylindrical nano-micelles, in both

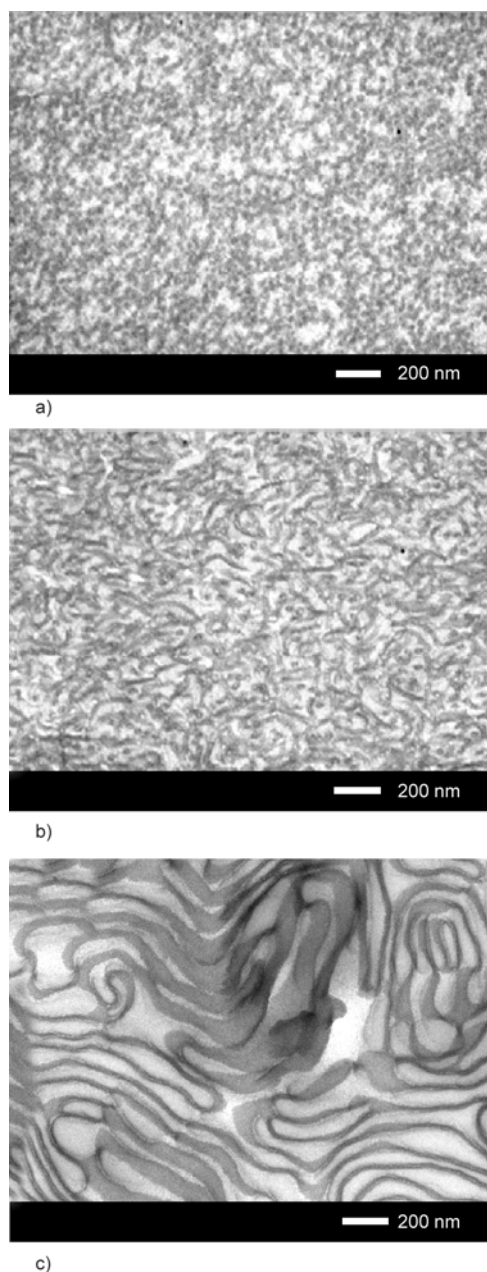


Figure 3. Effect of the PnBA content in the acrylic BCPs on the phase structures of DGEBA/20 wt% acrylic BCP blends cured with PN (catalyzed by 0.5 phr TPP): a) DGEBA/BCP50-6 (PnBA content in the BCP: 50 wt%), b) DGEBA/BCP68-6 (PnBA content in the BCP: 68 wt%), c) DGEBA/BCP77-7 (PnBA content in the BCP: 77 wt%)

the cases of the 10% BCP blend and the 20% BCP blend. Figure 4 shows the magnified image of the 20% BCP68-6 blend. The diameter of the cylindrical micelles was about 20 nanometers. The branched micelles were dispersed randomly and partially connected to each other in 3-dimensional directions. And the cured blends of the DGEBA/BCP77-7 (ie. 77% PnBA in the BCP) gave nano-micelles of ‘curved lamella’, in the both the cases of the 10%

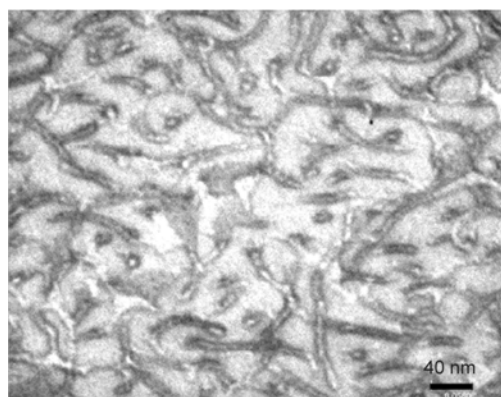
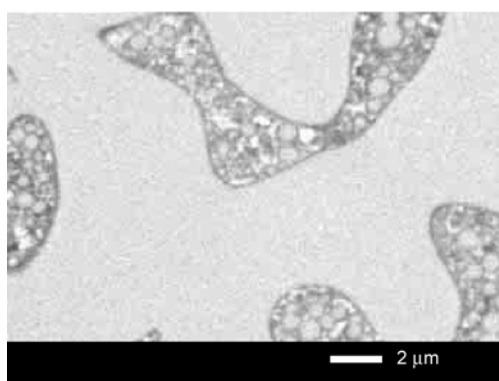


Figure 4. Phase structure (higher magnified image) of DGEBA/20 wt% BCP68-6 blend cured with PN (PnBA content in the BCP: 68 wt%, M_w of the BCP = 60 000). Note the nano-cylinders were branched in random directions.

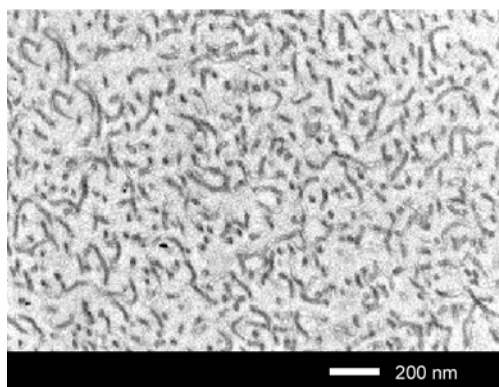
BCP blend and the 20% BCP blend, as shown in Figures 2c and 3c. The ‘curved lamella’ micelles were 3-dimensionally continuous in the whole observed area.

Dean *et al.* [21] clarified that the methylenedianiline-cured DGEBA/PEO-PB block copolymer blends showed phase transition from spherical micelles to wormlike micelles and finally to vesicles, as the volume fraction of the epoxy-miscible block decreased [21]. The interfacial curvature could be determined by the geometrical constraints of the block copolymers, balancing the competing factors, such as achieving a constant density of the polymer chain and minimizing the chain stretching [15, 16, 21]. Although the types of the phase structures in the present study were different from theirs, the basic rule determining the interfacial curvature was similar. Namely, the interfacial curvature of the phase structures decreased as the ratio of the epoxy-immiscible block increased (i.e. the ratio of the epoxy-miscible block decreased), from spherical micelles to branched cylindrical micelles, and to ‘curved lamella’ micelles.

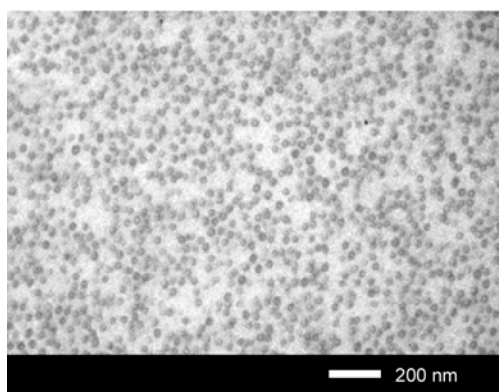
Next, the effect of the molecular weight of the BCP was also examined in terms of the phase structures of the epoxy blends. The molecular weights of the BCPs were changed from 26 000 to 132 000. In the meantime, the PnBA ratio of the BCPs was maintained at 68–70 wt%. Therefore, the effect of the molecular weight of the BCPs could be extracted. Figure 5 (10 wt% BCP in the blends) and Figure 6 (20 wt% BCP in the blends) show the phase structures (TEM photographs) of the epoxy/BCP blends.



a)



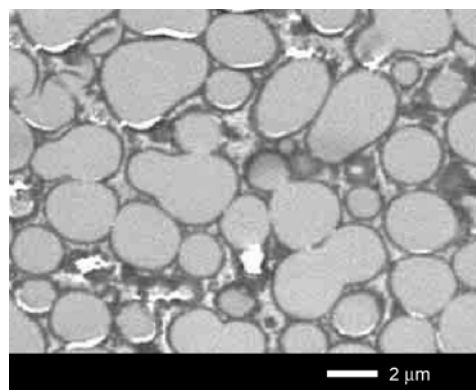
b)



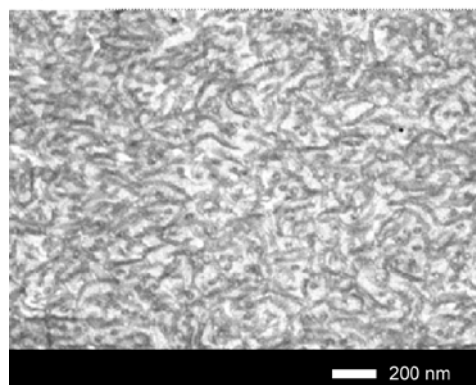
c)

Figure 5. Effect of the molecular weight of the acrylic BCPs on the phase structures of DGEBA/10 wt% acrylic BCP blends cured with PN (catalyzed by 0.5 phr TPP): a) DGEBA/BCP70-3 (M_w of the BCP: 26 000), b) DGEBA/BCP68-6 (M_w of the BCP: 60 000), c) DGEBA/BCP69-13 (M_w of the BCP: 132 000)

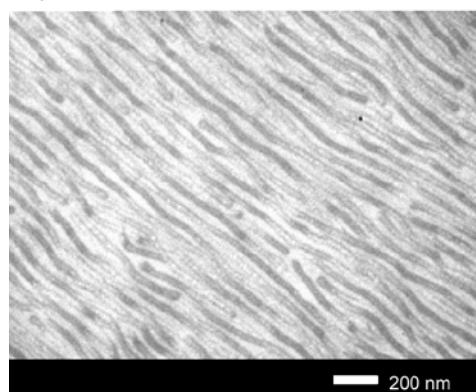
Figure 5b and Figure 6b show the blends of the BCP68-6 with the molecular weight of 60 000, which were explained as in Figure 2b and Figure 3b. Figure 5c and Figure 6c show the blends of the BCP69-13 with the molecular weight of 132 000. The blend of 10% BCP69-13 in Figure 5c showed spherical nano-micelles. The blend of 20% BCP69-13 in Figure 6c showed arrayed cylindrical micelles which were dispersed regularly in an epoxy-rich



a)



b)



c)

Figure 6. Effect of the molecular weight of the acrylic BCPs on the phase structures of DGEBA/20 wt% acrylic BCP blends cured with PN (catalyzed by 0.5 phr TPP): a) DGEBA/BCP70-3 (M_w of the BCP: 26 000), b) DGEBA/BCP68-6 (M_w of the BCP: 60 000), c) DGEBA/BCP69-13 (M_w of the BCP: 132 000)

matrix, similar to the phase structure in our previous paper [30]. Moreover, the phase separated structure of the cured 20% BCP69-13 blend was examined by the USAXS measurement. Figure 7a shows the azimuthally integrated USAXS intensity against scattering vector q . The scattering profile is the result from both the structure factor and the form factor of the phase separated BCP blend. The first order peak, which can be assigned to the structure factor

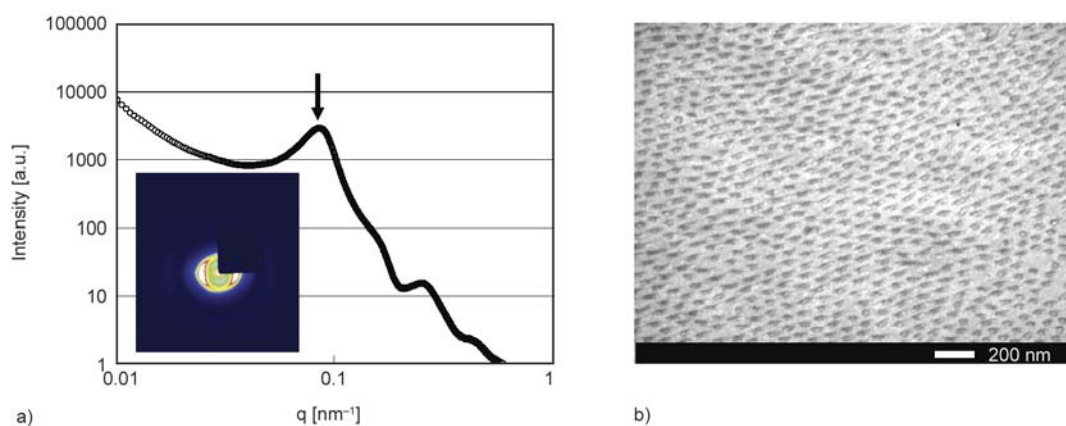


Figure 7. a) Azimuthally integrated USAXS profile for the PN-cured DGEBA/20 wt% BCP69-13 blend. The inset in the figure shows the corresponding two-dimensional images. b) Cross-section of the 20 wt% BCP blend in Figure 6c, which was cut from the perpendicular direction and observed by TEM. Both the USAXS profile and the TEM images suggest that the blend has the hexagonally packed cylindrical micelles.

from the phase structure, was indicated by the left arrow. The inset in the Figure 7a corresponds to the two-dimensional image of the scattering, and presents the strongly oriented phase structure. Figure 7b shows the section cut from the perpendicular direction of the same blends in Figure 6c, which indicates the cross-sections of the packed cylindrical micelles. The estimated distance of the micelles from the first order peak in the Figure 7a was about 75 nm, which is consistent with the TEM images showing the hexagonally packed cylindrical micelles. As will be discussed later, the anisotropic phase structure could be created by the growth of the initial phase structure due to the thermodynamic repulsion between the epoxy matrix and the PnBA segment which is immiscible with the epoxy matrix. The immiscibility is also the source that the form factor is pronounced. It was confirmed from the USAXS measurements that all the epoxy/BCP blends possessed the nanostructures which were indicated from the TEM observations.

Figures 5a and 6a show the cured blends of the DGEBA/BCP70-3 (the molecular weight: 26 000). Please note the magnification of these photographs is 10 times lower than the others in Figures 5 and 6. Both the 10% BCP70-3 blend and the 20% BCP70-3 blend had macro-phase separation in micrometer-sizes. A plausible reason for the macro-phase separation of the DGEBA/BCP70-3 blends would be in the poor ability of the low molecular-weight BCP to stabilize the nanostructure. The phase sizes in Figures 5a and 6a were similar to those of the epoxy

blends which were formed by the reaction-induced phase separation [12–14]. This suggests that the PMMA blocks in the low molecular-weight BCP were separated from the epoxy matrices in the curing process. The demixing of the PMMA block would be the trigger to make the macro-phase via reaction-induced phase separation. Moreover, the T_g s of the BCPs themselves were measured by DSC to examine the properties of the blocks. In general, the PMMA-*b*-PnBA-*b*-PMMA triblock copolymer shows two T_g s, assigned to the PMMA block chain and the PnBA block chain. In fact, the BCP68-6 and the BCP69-13 had two T_g s at -40 and 120°C . The first T_g (-40°C) can be assigned to the PnBA block chain, and the second T_g (120°C) can be assigned to the PMMA block chain. However, the T_g s of the low molecular-weight BCP70-3 were different from these two. Namely, the T_g s of the BCP70-3 were at -25 and at 40°C , which indicated that the properties of the block chains with low molecular-weight was clearly different from those with high molecular-weight. These results also suggest that the low molecular-weight PMMA block of BCP70-3 would not have same ability to stabilize the nano-phase structures in the epoxy/BCP blends, in comparison with the high molecular-weight PMMA block in other BCPs. The ability to stabilize the phase separation would be a key factor in the creation of periodical nano-phase structures in the epoxy/BCP blends, as well as the miscibility-immiscibility of the block chains to the matrix polymer [30].

3.2. Influence of the reaction rate on the phase structures and the phase diagram of cured DGEBA/PMMA-PnBA-PMMA triblock copolymers

In general, the morphology of the epoxy/thermoplastic polymer blends having a ‘reaction-induced phase separation mechanism’ is not determined at the thermodynamically stable state [12, 13]. It is often affected by the curing reaction rate, because the progress of the phase separation of the blends could be frozen by the cross-link formation of the epoxies and curing agents. The final phase structures depend on the kinetics between the reaction-induced phase separation and the fixation of the phase structure by the cross-link formation. Therefore, the phase structures of each epoxy/acrylic BCP blend were reexamined, in terms of the effect of the reaction rate (gel time). To be specific, the gel time of the epoxy blends at 120°C was altered from 5 to 150 minutes by only slightly changing the amount of the catalyst (TPP), while keeping the main composition of the DGEBA/acrylic BCP/PN.

Figure 8 shows the case of the DGEBA/BCP69-13 (10 wt%) blends. The phase type was spherical

nano-micelles, and the phase type and the phase sizes were maintained, irrespective of the gel times. Figure 9 shows the case of random cylindrical nano-micelles of the DGEBA/BCP68-6 (10 wt%) blends. This also indicated that the changes of the phase types and the phase sizes were not observed, irrespective of the gel times. Figure 10 shows the case of hexagonally packed cylindrical micelles of the DGEBA/BCP69-13 (20 wt%) blends. The type of the nano-structure was roughly kept. However, the alignment of the cylinders in the blends with a gel time of 5 min was not sufficient. The alignment of the cylinders progressed according to the delay of the gel time. Figure 11 shows the case of the ‘curved lamella’ micelles of the DGEBA/BCP79-11 (20 wt%) blends. Roughly speaking, the type of the nano-structure was maintained, but the alignment of the lamella progressed, with the delay of the gel time. It can be summarized that the details of the phase structures having anisotropic nature could be affected by the reaction rate though the thermodynamics was the main driving force for leading a stable state in each phase structure.

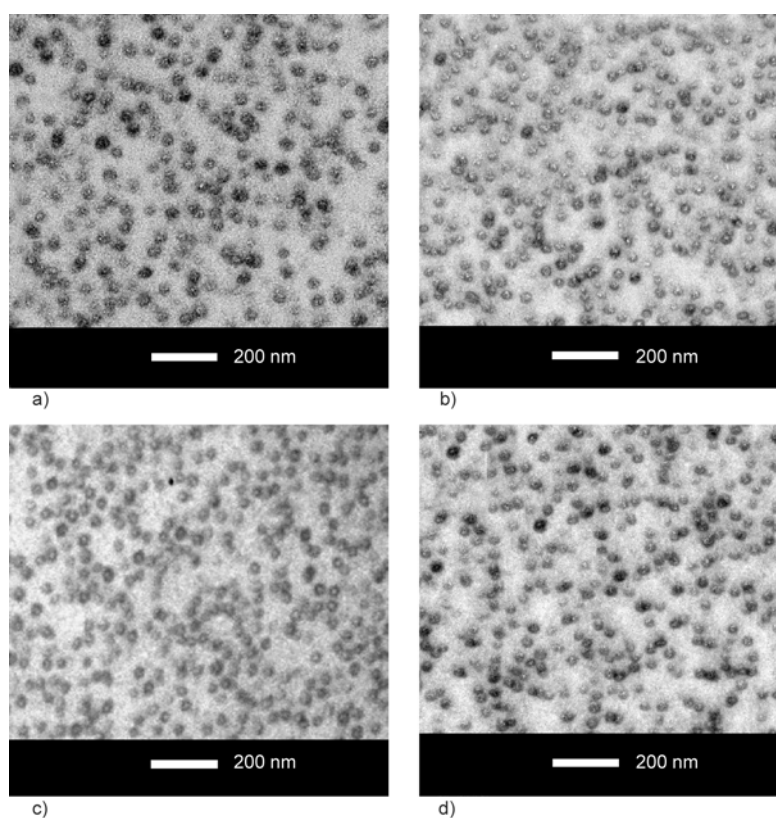


Figure 8. Influences of curing reaction rate (gel time) on the phase structures of the DGEBA/BCP69-13 (PnBA content in the BCP: 69 wt%) blends cured with PN. Content of the BCP in the blend: 10 wt%. Gel time at 120°C: (a) 5 min, (b) 8 min, (c) 15 min, (d) 150 min.

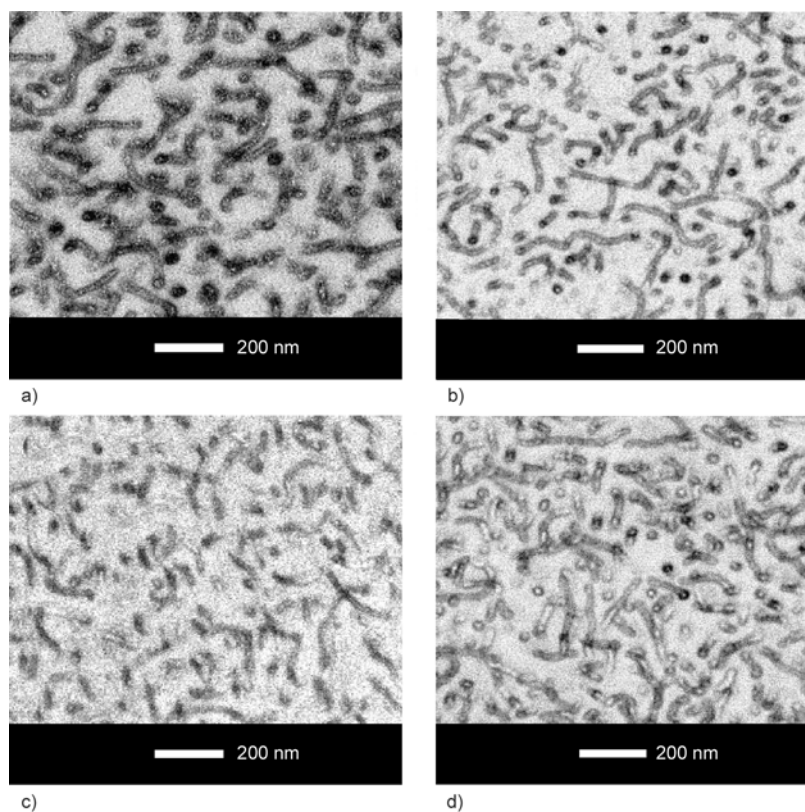


Figure 9. Influences of curing reaction rate (gel time) on the phase structures of the DGEBA/BCP68-6 (PnBA content in the BCP: 68 wt%) blends cured with PN. Content of the BCP in the blend: 10 wt%. Gel time at 120°C: (a) 5 min, (b) 8 min, (c) 15 min, (d) 150 min.

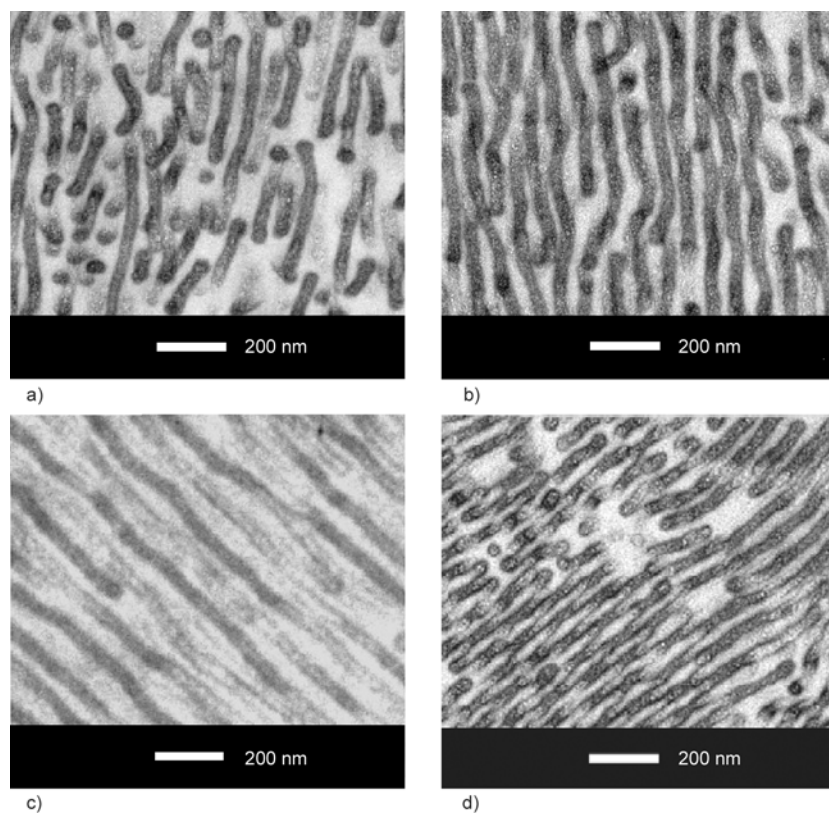


Figure 10. Influences of curing reaction rate (gel time) on the phase structures of the DGEBA/BCP69-13 (PnBA content in the BCP: 69 wt%) blends cured with PN. Content of the BCP in the blend: 20 wt%. Gel time at 120°C: (a) 5 min, (b) 8 min, (c) 15 min, (d) 150 min.

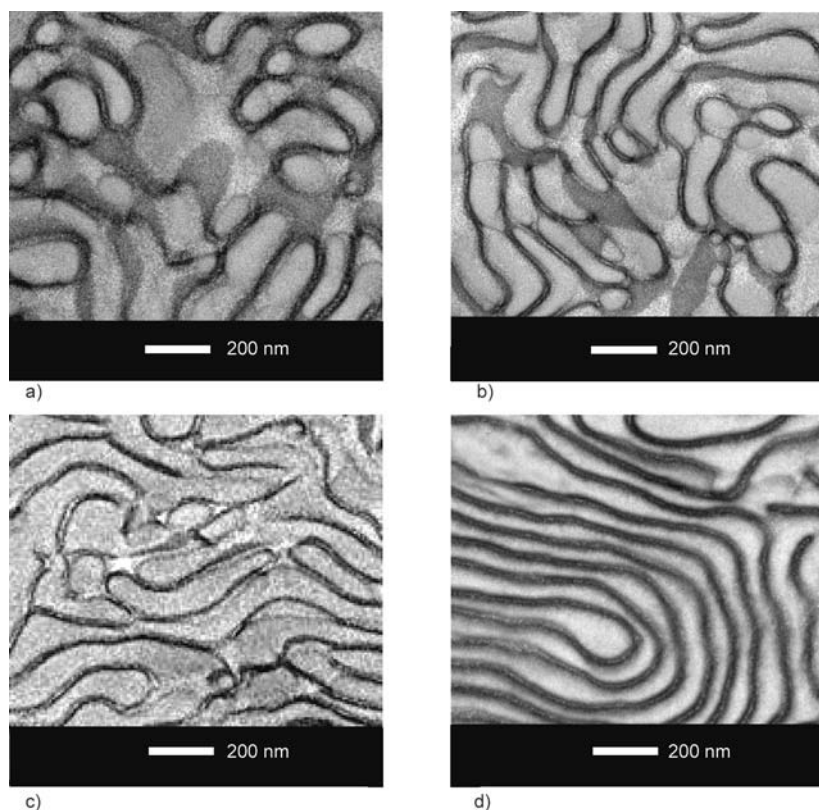


Figure 11. Influences of curing reaction rate (gel time) on the phase structures of the DGEBA/BCP79-11 (PnBA content in the BCP: 79 wt%) blends cured with PN. Content of the BCP in the blend: 20 wt%. Gel time at 120°C: (a) 5 min, (b) 8 min, (c) 15 min, (d) 150 min.

On the other hand, the types of the nanostructures were maintained in this study, irrespective of the gel time, under the condition of keeping the main composition of the blends. Specifically, the phase structures in the PN-cured DGEBA/acrylic BCP blends were roughly determined from the compositions of the blends. This is probably because the seeds of the nanostructures already existed in the blends before the start of the reaction of epoxy and PN [15, 16]. Figure 12 is the initial SAXS profile for the DGEBA/20 wt% BCP69-13 blend which is just reaching 120°C. This is the evidence to show the existence of the seeds of the cylindrical nanostructure before the curing. Of course, the USAXS results do not mean that there was no change in the phase structures in the curing process. In-situ SAXS analyses during the curing process are necessary to verify the details of the structure change of the DGEBA/acrylic BCP blends, which will be clarified in the next paper. However, the USAXS results (Figure 12) indicated clearly that the nanostructure existed before the curing. The seeds of the nanostructures were formed via ‘self-assembly’ mechanism, not formed via ‘reaction-induced phase separation’ mechanism. Meanwhile, Romeo *et al.* [37] reported that the cure cycle

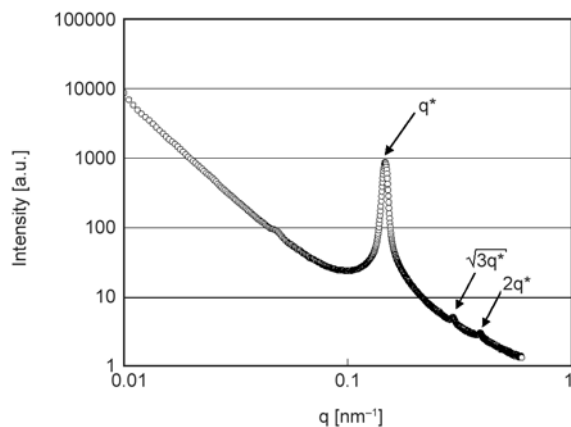


Figure 12. USAXS profile for the DGEBA/20 wt% BCP69-13 blend just reaching 120°C (before the curing). The profile suggests the hexagonally packed cylindrical micelles.

affected the types of the nanostructures of a DGEBA/PS-*b*-PMMA BCP blend which were formed via ‘reaction-induced phase separation’. The selected blend in the literature firstly made a homogeneous solution before the curing, and phase-separated in the curing process. The ‘reaction-induced phase separation’ would be favorable in terms of giving the versatile morphologies of the epoxy/BCP blends by changing the cure cycle. On the other hand, the

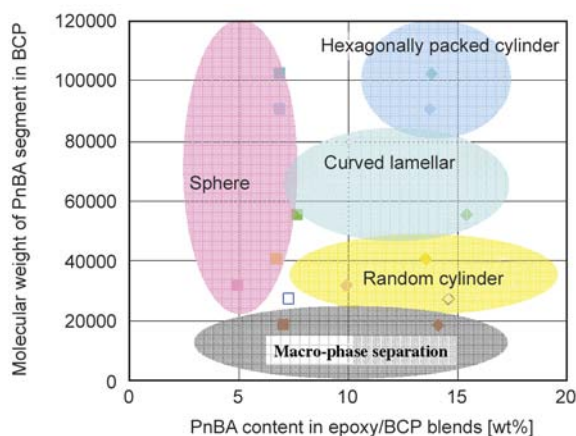


Figure 13. Phase diagram of the DGEBA/acrylic-BCP blends cured with PN (catalyzed by TPP)

experimental results obtained in our study may suggest the advantage of the ‘self-assembly’ system in terms of giving robustness of the nanostructures of the epoxy/BCP blends, against the change of the curing conditions.

As the final stage of the present paper, we tried to describe a phase diagram of the PN-cured DGEBA/PMMA-*b*-PnBA-*b*-PMMA triblock copolymer blends, as shown in Figure 13. The horizontal axis shows the amount of the PnBA block chain in whole blend polymers, and the vertical axis shows the molecular weight of the PnBA block chain of the BCPs. The phase diagram described the regions of nano-spheres, hexagonally packed cylinders, curved lamellae, randomly dispersed cylinders, and the macro phase separation. The PnBA block chains of the BCPs were immiscible with the PN-cured DGEBA [30]. Namely, it can be summarized that the nanostructures of the PN-cured DGEBA/PMMA-*b*-PnBA-*b*-PMMA triblock copolymer blends were controlled by the molecular weight of the immiscible PnBA-block chain and the ratio of the PnBA in the blends. The information could become the basis to control the morphology and the mechanical properties of the DGEBA/acrylic BCP blends.

4. Conclusions

Nanostructures of DGEBA/PMMA-*b*-PnBA-*b*-PMMA triblock copolymers (acrylic BCPs) were studied. Several nanostructures, such as spheres, cylinders (hexagonally-packed or randomly-dispersed), curved lamellae, were observed in the cured epoxy blends using a transmission electron microscope. It was found that the nanostructures were controlled by the molecular weight of the immiscible

PnBA-block chain and the ratio of the PnBA in the blends. Moreover, the effect of the gel time to the nanostructures in the blends was examined by altering the trace amount of the catalyst. When the compositions of the epoxy blends were maintained, the types of the nanostructures were almost always maintained, irrespective of the difference of the gel time. The USAXS results indicated clearly that the nanostructures existed before the curing. The seeds of the nanostructures were formed via ‘self-assembly’ mechanism, not formed via ‘reaction-induced phase separation’. From these experimental results, a phase diagram of the cured DGEBA/acrylic BCP blends was proposed.

Acknowledgements

This work was financially supported by a Grant-in Aid for Scientific Research (24360280) from the Ministry of Education, Culture, Sports, Science and Technology, and also by Yazaki Corporation.

References

- [1] Kinloch A. J., Shaw S. J., Tod D. A., Hunston D. A.: Deformation and fracture behaviour of a rubber-toughened epoxy: 1. Microstructure and fracture studies. *Polymer*, **24**, 1341–1354 (1983). DOI: [10.1016/0032-3861\(83\)90070-8](https://doi.org/10.1016/0032-3861(83)90070-8)
- [2] Yee A. F., Pearson R. E.: Toughening mechanisms in elastomer-modified epoxies, Part 1. Mechanical studies. *Journal of Materials Science*, **21**, 2462–2474 (1986). DOI: [10.1007/BF01114293](https://doi.org/10.1007/BF01114293)
- [3] Pearson R. E., Yee A. F.: Toughening mechanisms in elastomer-modified epoxies, Part 2. Microscopy studies. *Journal of Materials Science*, **21**, 2475–2488 (1986). DOI: [10.1007/BF01114294](https://doi.org/10.1007/BF01114294)
- [4] Pearson R. E., Yee A. F.: Toughening mechanisms in elastomer-modified epoxies, Part 3. The effect of cross-link density. *Journal of Materials Science*, **24**, 2571–2580 (1989). DOI: [10.1007/BF01174528](https://doi.org/10.1007/BF01174528)
- [5] Yee A. F., Li D., Li X.: The importance of constraint relief caused by rubber cavitation in the toughening of epoxy. *Journal of Materials Science*, **28**, 6392–6398 (1993). DOI: [10.1007/BF01352202](https://doi.org/10.1007/BF01352202)
- [6] Kishi H., Shi Y-B., Huang J., Yee A. F.: Ductility and toughenability study of epoxy resins under multiaxial stress states. *Journal of Materials Science*, **33**, 3479–3488 (1998). DOI: [10.1023/A:1013222421843](https://doi.org/10.1023/A:1013222421843)
- [7] Bucknall C. B., Partridge I. K.: Phase separation in epoxy resins containing polyethersulphone. *Polymer*, **24**, 639–644 (1983). DOI: [10.1016/0032-3861\(83\)90120-9](https://doi.org/10.1016/0032-3861(83)90120-9)

- [8] Raghava R. S.: Development and characterization of thermosetting-thermoplastic polymer blends for applications in damage-tolerant composites. *Journal of Polymer Science Part B: Polymer Physics*, **26**, 65–81 (1988). DOI: [10.1002/polb.1988.090260103](https://doi.org/10.1002/polb.1988.090260103)
- [9] Bucknall C. B., Gilbert A. H.: Toughening tetrafunctional epoxy resins using polyetherimide. *Polymer*, **30**, 213–217 (1989). DOI: [10.1016/0032-3861\(89\)90107-9](https://doi.org/10.1016/0032-3861(89)90107-9)
- [10] Hedrick J. L., Yilgor I., Jurek M., Hedrick J. C., Wilkes G. L., McGrath J. E.: Chemical modification of matrix resin networks with engineering thermoplastics: 1. Synthesis, morphology, physical behaviour and toughening mechanisms of poly(arylene ether sulphone) modified epoxy networks. *Polymer*, **32**, 2020–2032 (1991). DOI: [10.1016/0032-3861\(91\)90168-I](https://doi.org/10.1016/0032-3861(91)90168-I)
- [11] Kishi H., Odagiri N.: Toughened thermoset resin matrix composites. in ‘Series in materials science and engineering – Aerospace materials’ (eds.: Cantor B., Assender H., Grant P.) Institute of Physics Publishing, Bristol, Chapter 14, 187–198 (2001).
- [12] Yamanaka K., Inoue T.: Structure development in epoxy resin modified with poly(ether sulphone). *Polymer*, **30**, 662–667 (1989). DOI: [10.1016/0032-3861\(89\)90151-1](https://doi.org/10.1016/0032-3861(89)90151-1)
- [13] Yamanaka K., Takagi Y., Inoue T.: Reaction-induced phase separation in rubber-modified epoxy resins. *Polymer*, **30**, 1839–1844 (1989). DOI: [10.1016/0032-3861\(89\)90355-8](https://doi.org/10.1016/0032-3861(89)90355-8)
- [14] Williams R. J. J., Rozenberg B. A., Pascault J-P.: Reaction-induced phase separation in modified thermosetting polymers. *Advances in Polymer Science, Polymer Analysis Polymer Physics*, **128**, 95–156 (1997). DOI: [10.1007/3-540-61218-1_7](https://doi.org/10.1007/3-540-61218-1_7)
- [15] Hillmyer M. A., Lipic P. M., Hajduk D. A., Almdal K., Bates F. S.: Self-assembly and polymerization of epoxy resin-amphiphilic block copolymer nanocomposites. *Journal of the American Chemical Society*, **119**, 2749–2750 (1997). DOI: [10.1021/ja963622m](https://doi.org/10.1021/ja963622m)
- [16] Lipic P. M., Bates F. S., Hillmyer M. A.: Nanostructured thermosets from self-assembled amphiphilic block copolymer/epoxy resin mixtures. *Journal of the American Chemical Society*, **120**, 8963–8970 (1998). DOI: [10.1021/ja981544s](https://doi.org/10.1021/ja981544s)
- [17] Mijovic J., Shen M., Sy J. W., Mondragon I.: Dynamics and morphology in nanostructured thermoset network/block copolymer blends during network formation. *Macromolecules*, **33**, 5235–5244 (2000). DOI: [10.1021/ma991894e](https://doi.org/10.1021/ma991894e)
- [18] Dean J. M., Lipic P. M., Grubbs R. B., Cook R. F., Bates F. S.: Micellar structure and mechanical properties of block copolymer-modified epoxies. *Journal of Polymer Science Part B: Polymer Physics*, **39**, 2996–3010 (2001). DOI: [10.1002/polb.10062](https://doi.org/10.1002/polb.10062)
- [19] Guo Q., Thomann R., Gronski W., Thurn-Albrecht T.: Phase behavior, crystallization, and hierarchical nanostructures in self-organized thermoset blends of epoxy resin and amphiphilic poly(ethylene oxide)-*block*-poly(propylene oxide)-*block*-poly(ethylene oxide) triblock copolymers. *Macromolecules*, **35**, 3133–3144 (2002). DOI: [10.1021/ma011971h](https://doi.org/10.1021/ma011971h)
- [20] Dean J. M., Verghese N. E., Pham H. Q., Bates F. S.: Nanostructure toughened epoxy resins. *Macromolecules*, **36**, 9267–9270 (2003). DOI: [10.1021/ma034807y](https://doi.org/10.1021/ma034807y)
- [21] Dean J. M., Grubbs R. B., Saad W., Cook R. F., Bates F. S.: Mechanical properties of block copolymer vesicle and micelle modified epoxies. *Journal of Polymer Science Part B: Polymer Physics*, **41**, 2444–2456 (2003). DOI: [10.1002/polb.10595](https://doi.org/10.1002/polb.10595)
- [22] Wu J., Thio Y. S., Bates F. S.: Structure and properties of PBO-PEO diblock copolymer modified epoxy. *Journal of Polymer Science Part B: Polymer Physics*, **43**, 1950–1965 (2005). DOI: [10.1002/polb.20488](https://doi.org/10.1002/polb.20488)
- [23] Ritzenthaler S., Court F., David L., Girard-Reydet E., Leibler L., Pascault J. P.: ABC triblock copolymers/epoxy-diamine blends. 1. Keys to achieve nanostructured thermosets. *Macromolecules*, **35**, 6245–6254 (2002). DOI: [10.1021/ma0121868](https://doi.org/10.1021/ma0121868)
- [24] Ritzenthaler S., Court F., Girard-Reydet E., Leibler L., Pascault J. P.: ABC triblock copolymers/epoxy-diamine blends. 2. Parameters controlling the morphologies and properties. *Macromolecules*, **36**, 118–126 (2003). DOI: [10.1021/ma0211075](https://doi.org/10.1021/ma0211075)
- [25] Maiez-Tribut S., Pascault J. P., Soulé E. R., Borrajo J., Williams R. J. J.: Nanostructured epoxies based on the self-assembly of block copolymers: A new miscible block that can be tailored to different epoxy formulations. *Macromolecules*, **40**, 1268–1273 (2007). DOI: [10.1021/ma0621851](https://doi.org/10.1021/ma0621851)
- [26] Gerard P., Boupat N. P., Fine T., Gervat L., Pascault J-P.: Toughness properties of lightly crosslinked epoxies using block copolymers. *Macromolecular Symposia*, **256**, 55–64 (2007). DOI: [10.1002/masy.200751006](https://doi.org/10.1002/masy.200751006)
- [27] Rebizant V., Abetz V., Tournilhac F., Court F., Leibler L.: Reactive tetrablock copolymers containing glycidyl methacrylate. synthesis and morphology control in epoxy-amine networks. *Macromolecules*, **36**, 9889–9896 (2003). DOI: [10.1021/ma0347565](https://doi.org/10.1021/ma0347565)
- [28] Rebizant V., Venet A-S., Tournilhac F., Girard-Reydet E., Navarro C., Pascault J-P., Leibler L.: Chemistry and mechanical properties of epoxy-based thermosets reinforced by reactive and nonreactive SBMX block copolymers. *Macromolecules*, **37**, 8017–8027 (2004). DOI: [10.1021/ma0490754](https://doi.org/10.1021/ma0490754)

- [29] Serrano E., Tercjak A., Ocando C., Larrañaga M., Parrellada M. D., Corona-Galván S., Mecerreyes D., Zafeiropoulos N. E., Stamm M., Mondragon I.: Curing behavior and final properties of nanostructured thermosetting systems modified with epoxidized styrene-butadiene linear diblock copolymers. *Macromolecular Chemistry and Physics*, **208**, 2281–2292 (2007). DOI: [10.1002/macp.200700169](https://doi.org/10.1002/macp.200700169)
- [30] Kishi H., Kunimitsu Y., Imade J., Oshita S., Morishita Y., Asada M.: Nano-phase structures and mechanical properties of epoxy/acryl triblock copolymer alloys. *Polymer*, **52**, 760–768 (2011). DOI: [10.1016/j.polymer.2010.12.025](https://doi.org/10.1016/j.polymer.2010.12.025)
- [31] Meng F., Zheng S., Zhang W., Li H., Liang Q.: Nanostructured thermosetting blends of epoxy resin and amphiphilic poly(ϵ -caprolactone)-*block*-polybutadiene-*block*-poly(ϵ -caprolactone) triblock copolymer. *Macromolecules*, **39**, 711–719 (2006). DOI: [10.1021/ma0518499](https://doi.org/10.1021/ma0518499)
- [32] Meng F., Zheng S., Li H., Liang Q., Liu T.: Formation of ordered nanostructures in epoxy thermosets: A mechanism of reaction-induced microphase separation. *Macromolecules*, **39**, 5072–5080 (2006). DOI: [10.1021/ma060004+](https://doi.org/10.1021/ma060004+)
- [33] Yu R., Zheng S.: Morphological transition from spherical to lamellar nanophases in epoxy thermosets containing poly(ethylene oxide)-*block*-poly(ϵ -caprolactone)-*block*-polystyrene triblock copolymer by hardeners. *Macromolecules*, **44**, 8546–8557 (2011). DOI: [10.1021/ma201456x](https://doi.org/10.1021/ma201456x)
- [34] Yu R., Zheng S., Li X., Wang J.: Reaction-induced microphase separation in epoxy thermosets containing *block* copolymers composed of polystyrene and poly(ϵ -caprolactone): Influence of copolymer architectures on formation of nanophases. *Macromolecules*, **45**, 9155–9168 (2012). DOI: [10.1021/ma3017212](https://doi.org/10.1021/ma3017212)
- [35] Liu J., Sue H-J., Thompson Z. J., Bates F. S., Dettloff M., Jacob G., Verghese N., Pham H.: Nanocavitation in self-assembled amphiphilic *block* copolymer-modified epoxy. *Macromolecules*, **41**, 7616–7624 (2008). DOI: [10.1021/ma801037q](https://doi.org/10.1021/ma801037q)
- [36] Thompson Z. J., Hillymer M. A., Liu J., Sue H-J., Dettloff M., Bates F. S.: Block copolymer toughened epoxy: Role of cross-link density. *Macromolecules*, **42**, 2333–2335 (2009). DOI: [10.1021/ma900061b](https://doi.org/10.1021/ma900061b)
- [37] Romeo H. E., Zucchi I. A., Rico M., Hoppe C. E., Williams R. J. J.: From spherical micelles to hexagonally packed cylinders: The cure cycle determines nanostructures generated in block copolymer/epoxy blends. *Macromolecules*, **46**, 4854–4861 (2013). DOI: [10.1021/ma400778s](https://doi.org/10.1021/ma400778s)
- [38] Inoue T., Soen T., Hashimoto T., Kawai H.: Thermodynamic interpretation of domain structure in solvent-cast films of A–B type block copolymers of styrene and isoprene. *Journal of Polymer Science Part A-2: Polymer Physics*, **7**, 1283–1301 (1969). DOI: [10.1002/pol.1969.160070801](https://doi.org/10.1002/pol.1969.160070801)
- [39] Matsuo M., Sagae S., Asai H.: Fine structures of styrene-butadiene block copolymer films cast from toluene solution. *Polymer*, **10**, 79–87 (1969). DOI: [10.1016/0032-3861\(69\)90010-X](https://doi.org/10.1016/0032-3861(69)90010-X)
- [40] Matsen M. W., Bates F. S.: Unifying weak- and strong-segregation block copolymer theories. *Macromolecules*, **29**, 1091–1098 (1996). DOI: [10.1021/ma951138i](https://doi.org/10.1021/ma951138i)

Reinforcing styrene butadiene rubber with lignin-novolac epoxy resin networks

P. Yu, H. He*, C. Jiang, D. Wang, Y. Jia, L. Zhou, D. M. Jia

School of Materials Science and Engineering, South China University of Technology, 510641 Guangzhou, People's Republic of China

Received 18 June 2014; accepted in revised form 6 August 2014

Abstract. In this study, lignin-novolac epoxy resin networks were fabricated in the styrene butadiene rubber (SBR) matrix by combination of latex compounding and melt mixing. Firstly, SBR/lignin compounds were co-coagulated by SBR latex and lignin aqueous solution. Then the novolac epoxy resin (F51) was added in the SBR/lignin compounds by melt compounding method. F51 was directly cured by lignin via the ring-opening reaction of epoxy groups of F51 and OH groups (or COOH groups) of lignin during the curing process of rubber compounds, as was particularly evident from Fourier transform infrared spectroscopy (FTIR) studies and maximum torque of the curing analysis. The existence of lignin-F51 networks were also detected by scanning electron microscope (SEM) and dynamic mechanical analysis (DMA). The structure of the SBR/lignin/F51 was also characterized by rubber process analyzer (RPA), thermogravimetric analysis (TGA) and determination of crosslinking density. Due to rigid lignin-F51 networks achieved in SBR/lignin/F51 composites, it was found that the hardness, modulus, tear strength, crosslinking density, the temperature of 5 and 10% weight-loss were significantly enhanced with the loading of F51.

Keywords: rubber, reinforcements, lignin, novolac epoxy resin, interpenetrating polymer networks

1. Introduction

The copolymer Styrene butadiene rubber (SBR), a general-purpose synthetic elastomer widely used in the rubber industry, is nonpolar and noncrystalline with a low gum tensile strength. Therefore, a reinforcing filler is often required in this matrix to improve the physic mechanical properties of SBR composites and reduce the material cost [1, 2]. Lignin, one of the most abundant biopolymers on earth, is a polyphenolic macromolecule which is comprised of 9-carbon phenol propane units (p-coumaryl alcohol, coniferyl alcohol, and sinapyl alcohol) linked together by different types of bonds. Large amounts of lignin have been generated by the papermaking industry and emerging cellulosic ethanol production [3]. Lignin is mainly used as a low-grade fuel and its potential is not fully exploited. It is economically

and environmentally desirable to convert lignin into valuable reinforcing additives for rubbers. Various academic papers regarding preparations of rubber/lignin compounds have been published [4–8]. Most recently, Xiao *et al.* [1] prepared styrene-butadiene rubber/lignin-layered double hydroxide composites by melt mixing. Jiang *et al.* [9] fabricated natural rubber/nano-lignin composites. Jiang *et al.* [10] also fabricated cationic lignin/montmorillonite nanosheets and used it to reinforce SBR. Frigerio *et al.* [11] prepared lignin modified by hexamethylenetetramine as a filler for styrene butadiene rubber. Liao *et al.* [12] and Cao *et al.* [13] fabricated a lignin-montmorillonite complex as a novel rubber filler and used it in acrylonitrile butadiene rubber composites. Bahl and Jana [14] modified lignosulfonate by cyclohexylamine and used it as a filler into SBR. Bahl *et al.*

*Corresponding author, e-mail: pshuihe@scut.edu.cn
© BME-PT

[15] also exploited non-covalent interactions between lignin and carbon black to lower the viscoelastic dissipation in rubber compounds.

Numerous scientific articles relating to preparations of lignin as curing agent in epoxy resin have been published [16, 17]. Self-crosslinkable lignin/epoxidized natural rubber composites were prepared by the ring-opening reaction between lignin and epoxidized natural rubber in our research group [18]. Epoxy resins also have been synthesized by an in-situ vulcanization to reinforce SBR [19]. Meanwhile, various interpenetrating polymer networks in the rubber compounds have been prepared [20–23]. However, to the best of our knowledge, there is no report about lignin-novolac epoxy resin networks reinforced SBR. Novolac epoxy resin (F51) was incorporated into SBR/lignin compounds to form lignin-F51 networks composites by in-situ reaction between epoxy groups of F51 and OH groups (or COOH groups) of lignin at the vulcanization condition of the rubber, therefore it could be pointed out that the lignin acts not only as a reinforcing agent but also as a crosslinking agent of F51. Thanks to the whole strong lignin-F51 networks constructed in the rubber matrix, the stress is partially transferred by lignin-F51 networks themselves, thus the reinforcement will not be so much dependent on the

interfacial properties, polarity discrepancy and dispersion of the filler, which were traditionally considered as crucial factors of reinforcement for the polymer [24]. This novel reinforcing strategy irrespective of the great polarity discrepancy between polar lignin and non-polar SBR is highly desirable. The formation and characteristics of lignin-F51 networks were investigated. The mechanical performances and vulcanization behaviors were studied as well as the thermal stability.

2. Materials and methods

2.1. Materials

Industrial sulfate lignin (the average molecular weight is 4235 and the polydispersity index is 2.4) was kindly provided by Guangzhou Linge Polymer Material Co., Ltd. (China). SBR latex with trade name of SBR 132 (the solid contents of the latex was 65 wt%) was obtained from Dongguan Benke Latex Co., Ltd. (China), which is a random copolymer consisting of 25 wt% styrene monomer. Novolac epoxy resin (tradename F51, which is a low molecular weight liquid) was purchased from Nanya Plastics Corporation (the epoxy value is 0.51) in China. The structures of the materials are given in Figure 1. The reagents used in rubber formula such as zinc oxide (ZnO), Stearic acid (SA), Sulfur (S), Accelerator N-

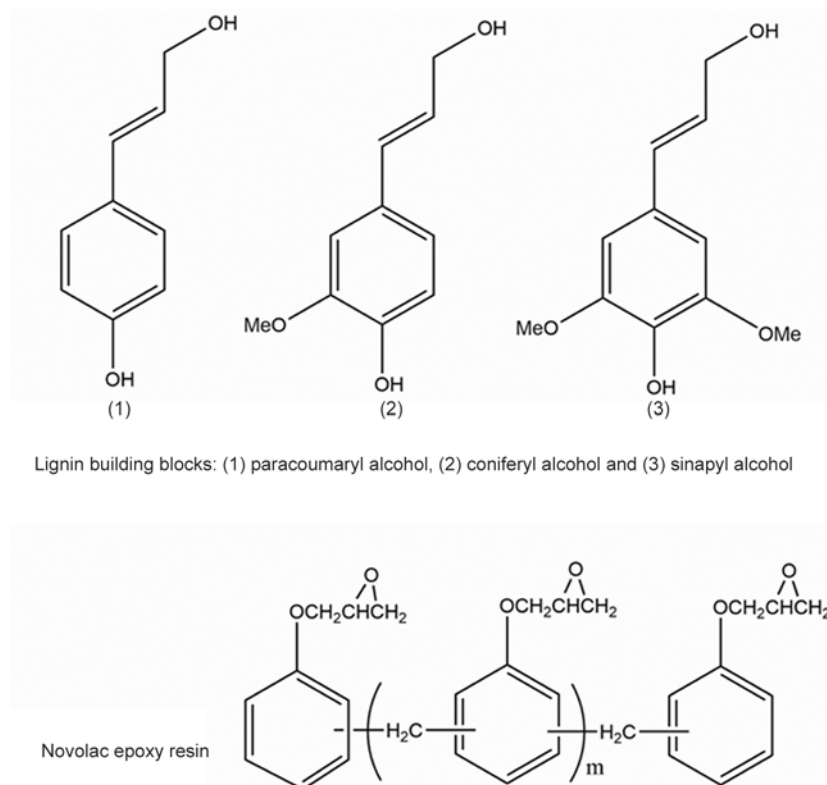


Figure 1. Structures of raw materials

cyclohexyl-2-benzothiazole sulfonamide (CZ) and Accelerator 2,2'-dibenzothiazole disulfide (DM) were provided by Rubber Institute of Guangzhou in China.

2.2. Preparation of SBR/50lignin compounds

Lignin was dissolved in deionized water at a mass concentration of 10% and the pH was adjusted to 12.5. The lignin solution (the dry weight ratio of lignin to SBR is 1:2) was dropped slowly into the SBR latex with vigorous stirring, and then 5 wt% sulfuric acid solution was added to co-coagulate the mixture. The mixture was filtered, water washed and then dried in oven at 70°C until a constant weight was obtained, the compounds were named SBR/50lignin.

2.3. Preparation of SBR/50lignin/F51 compounds and SBR/F51 compounds

F51 was added in the SBR/50lignin (or SBR) compounds by using a two-roll mill, followed by adding zinc oxide, stearic acid, accelerator CZ, accelerator DM and sulfur according to the recipe listed in Table 1. The compounds were compression molded and vulcanized at 160°C for optimum vulcanization time (T_{90}), which was determined by the U-CAN UR-2030 vulcameter. The preparation of SBR/

50lignin/F51 compounds is schematically depicted in Figure 2. The compounds were named SBR/50lignin/xF51 or SBR/xF51 compounds, x refers to the phr of F51 in the compounds (phr refers to parts per hundred of rubber).

2.4. Preparation of Model Compounds

In order to explore the possible interactions between lignin and F51, two model compounds were designed.

Model Compounds A: 100 g lignin and 20 g F51 were mixed in the high-speed multi mill (the speed was 30 000 rpm) for 5 minute, then put it in the oven for a curing process at the 160°C for 30 minutes. Fourier-transform infrared (FTIR) spectroscopy was used to characterize the possible reactions between lignin and F51 before and after curing. For comparison, neat lignin and neat F51 were also studied by FTIR.

Model Compounds B: *N*-SBR/50lignin/F51 compounds were prepared with the same procedure of SBR/50lignin/F51 except that no rubber additives (sulfur etc.) were added. For comparison, *N*-SBR and *N*-SBR/20F51 were also prepared. Note that *N* means that no rubber additives were added in this paper.

Table 1. Formulation of the mixtures and purposes*

Samples	Purpose
SBR, SBR/5F51, SBR/10F51, SBR/15F51, SBR/20F51.	To determine the influence of F51 on curing behavior of SBR vulcanizates.
SBR/50lignin, SBR/50lignin/5F51, SBR/50lignin/10F51, SBR/50lignin/15F51, SBR/50lignin/20F51.	To determine the influence of F51 on SBR/50lignin vulcanizates.

*rubber ingredients: ZnO 5, Stearic acid 2, S 1.6, Accelerator CZ 1.5, Accelerator DM 0.5.

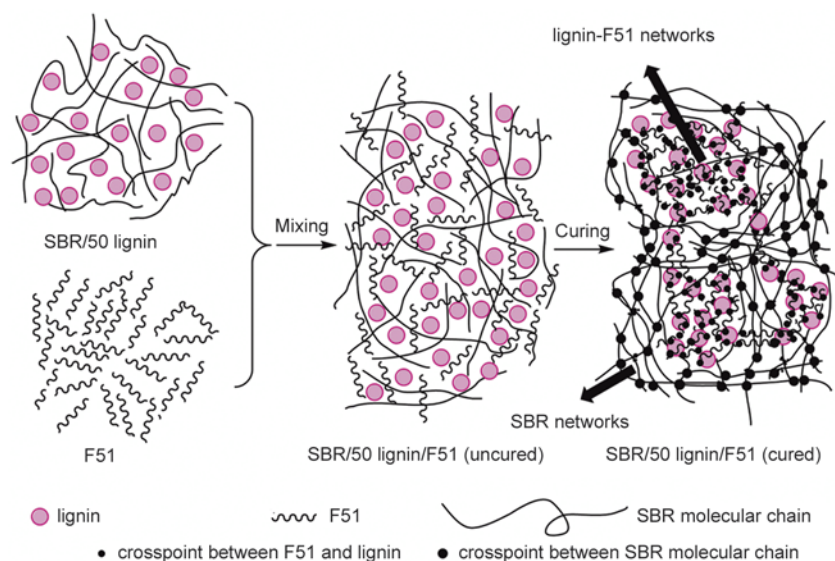


Figure 2. The preparation of SBR/50lignin/F51

2.5. Characterizations

Fourier transform infrared spectra (FTIR) were recorded in transmission mode on a Bruker Vertex 70 infrared spectrum analyzer (BRUKER OPTICS, Germany) with KBr pellets within the wave number range from 4000 to 400 cm^{-1} . The scanning was performed 32 times with a resolution of 4 cm^{-1} .

Mechanical properties measurements. The tensile and tear tests of the vulcanizates were performed according to ASTM D412 and ASTM D624 specifications, respectively. U-CAN UT-2060 (U-CAN Dynatex Inc., Taiwan) instrument was used with the strain rate of 500 mm/min.

The curing characteristics of the compounds were determined at 160°C by U-CAN UR-2030 vulcimeter (U-CAN Dynatex Inc., Taiwan).

Dynamic mechanical analysis was conducted on a Netzsch 242C DMA equipment (Netzsch, Germany). The tensile mode was selected. The measurements were carried out at a frequency of 2 Hz, a heating rate of 5°C/min over a temperature range of -90 to 200°C.

Measurements of crosslink density were carried out on Magnetism Resonance crosslinking density spectrometer (XLDS-15, IIC Innovative Imaging Corporation, Germany) according to the IIC test and analysis software package with a magnetic field intensity of 15 MHz at 85°C. Rubber sample with a length of 10 mm and a diameter of approximately 6 mm was placed into a glass tube for the test.

Thermal gravimetric analysis was carried out in a TA Q20 (TA Corporation, New Castle, America) thermogravimetric analyzer over a temperature range from 30 to 700°C at a heating rate of 10°C/min. Nitrogen was used as purging gas.

Rubber process analysis (RPA) was carried out in a RPA2000 (Alpha technologies Co, USA). Strain sweeps of uncured composites: During the strain sweeps, the temperature and frequency were kept at 60°C and 60 cpm, respectively. The range of the strain sweeps was 0–200%. Storage modulus (G')

was measured as a function of strain. Strain sweeps of cured composites: the temperature was raised to 160°C to cure the compound for T_{90} . Then, the temperature was reduced to 60°C again. During the strain sweeps, the temperature and frequency were kept at 60°C and 60 cpm. The range of the strain sweeps was 0–140% for the vulcanizates.

Scanning electron micrographs (SEM) of the composites were taken by a Nova Nano SEM 430 instrument (FEI, Netherlands), the voltage of the electron beam used for SEM observation was 10 kV. Preparation of the tensile fracture surface: the tensile fracture surfaces of SBR/50lignin and SBR/50lignin/20F51 were obtained by the tensile tests. Preparation of the etched surfaces of *N*-SBR/50lignin/F51: *N*-SBR/50lignin/F51 compounds were fractured at liquid N_2 temperature and then etched by toluene for 10 days to remove the free SBR matrix (the SBR phase are not crosslinked since no sulfur was added), then the etched surfaces were obtained. Note that all the samples were plated with a thin layer of gold before any observations.

3. Results and discussion

3.1. Reactions between lignin and F51

In the present study, it is believed that the OH groups (or COOH groups) of lignin could react with the epoxy groups of F51 by the ring-opening reaction, the reaction between OH and epoxy groups is schematically illustrated in Figure 3.

In order to eliminate the disturbance of SBR molecules in the FTIR investigation, the FTIR of F51/lignin = 5:1 (uncured and cured), F51 and lignin were performed and the results are presented in Figure 4. In the spectrum of lignin, the broad strong band between 3700 and 3200 cm^{-1} belongs to the hydroxyl stretching vibrations of lignin hydroxyls or absorbed water, and the peaks at about 2935 and 1460 cm^{-1} are attributed to CH stretching of methyl (CH_2) or methylene groups (CH_3). The absorption at about 1700 cm^{-1} are attributed to C=O stretching

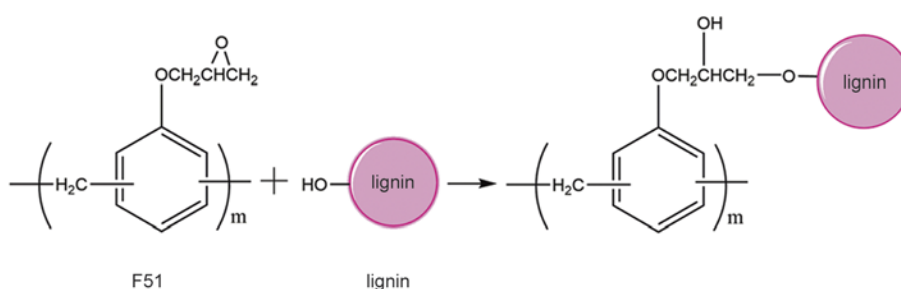


Figure 3. Schematic of the reaction between the epoxy groups of F51 and OH groups of lignin

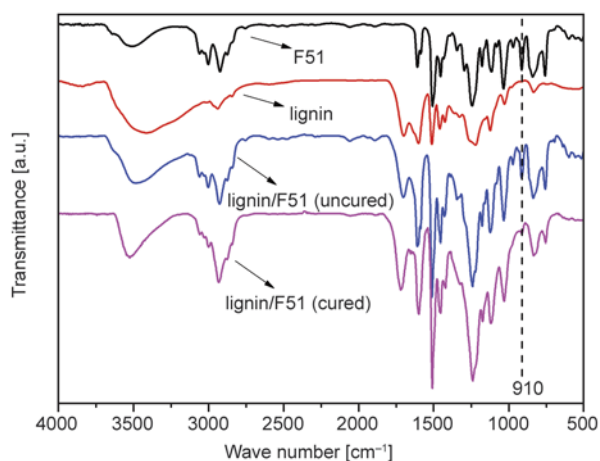


Figure 4. FTIR spectra of Model Compounds A

of lignin, and the absorption at 1510, 1424 and 1600 cm^{-1} is assigned to the aromatic skeletal vibration. Compared to lignin, in the case of uncured F51/lignin, there are some new absorption peaks appeared, and the peaks at 910 cm^{-1} are assigned to the stretching vibration of the C–O of the epoxy, which belong to characteristic absorptions of F51. This band almost disappeared after curing, indicating that F51 could react with lignin via the ring-opening reaction under the curing process of 160°C. Curing analysis of Model Compounds B were carried out to characterize the possible interactions between lignin and F51. As shown in Figure 5, the maximum torque (M_H) of *N*-SBR/20F51 is lower than that of *N*-SBR, this is because that F51 remains a low molecular weight liquid which acts as a plasticizer and lubricant in the SBR/20F51. Indicating there are no crosslinking reaction between F51 and SBR. The M_H of *N*-SBR/50lignin is higher than that

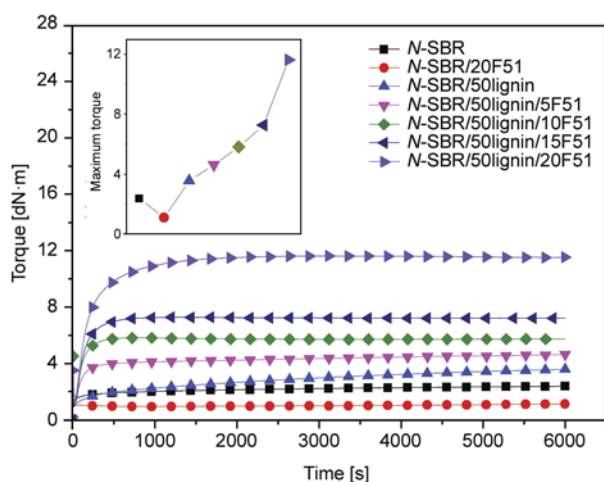


Figure 5. Curing curves of the Model Compounds B at 160°C

of *N*-SBR, this is because that there will be the rubber-filler interaction as well as usual volume fraction effects after addition of lignin, and this tends to impose extra resistance to flow of the SBR composites as a higher restriction to motion of the SBR molecules [25]. The M_H of *N*-SBR/50lignin/F51 compounds increases significantly with the increasing loading of F51. As an increase in torque is proportional to the crosslinking density [18]. It is evident that the crosslinked networks are formed due to the crosslinking reactions between lignin and F51. In order to further substantiate the formation and existence of lignin-F51 networks in the composites, the etched surfaces of *N*-SBR/50lignin/F51 are observed by SEM. As shown in Figure 6, no networks are observed in the sample of *N*-SBR/50lignin. However, preliminary networks embedded in the matrix are observed which disperse uniformly in the sample of *N*-SBR/50lignin/5F51, and the network pores are approximately 200~500 nanometers. In the sample of SBR/50lignin/10F51, the morphologies of the networks resemble glass fibers, the networks become more obvious and the network pores become smaller. In the sample of SBR/50lignin/15F51, irregular spherical particles are formed and interconnected. It should be noted that the lignin-F51 networks are not exactly the identical with the networks observed in Figure 6, this is because if a rubber and a filler are mixed, they interact in such a way that even a good solvent can only partially dissolve the rubber which originally is completely soluble in the solvent. The insoluble rubber is often referred to as the bound rubber [26]. We can infer that the networks observed in Figure 6 is complex of lignin-F51 networks and bound rubber held together by lignin-F51 networks. Since the networks observed in Figure 6 is closely related with lignin-F51 networks, we can say that the general morphology of F51-lignin networks is roughly outlined in the SEM when the free SBR was dissolved by toluene. So we demonstrate the existence of lignin-F51 network.

3.2. Curing analysis of SBR/50lignin/F51 compounds and SBR/F51 compounds

As shown in Figure 7 and Table 2, the T_{90} of SBR/F51 compounds is increased significantly with the increasing loading of F51, indicating that F51 delays the vulcanization, which is ascribed to the consumption of rubber additives by epoxy group of

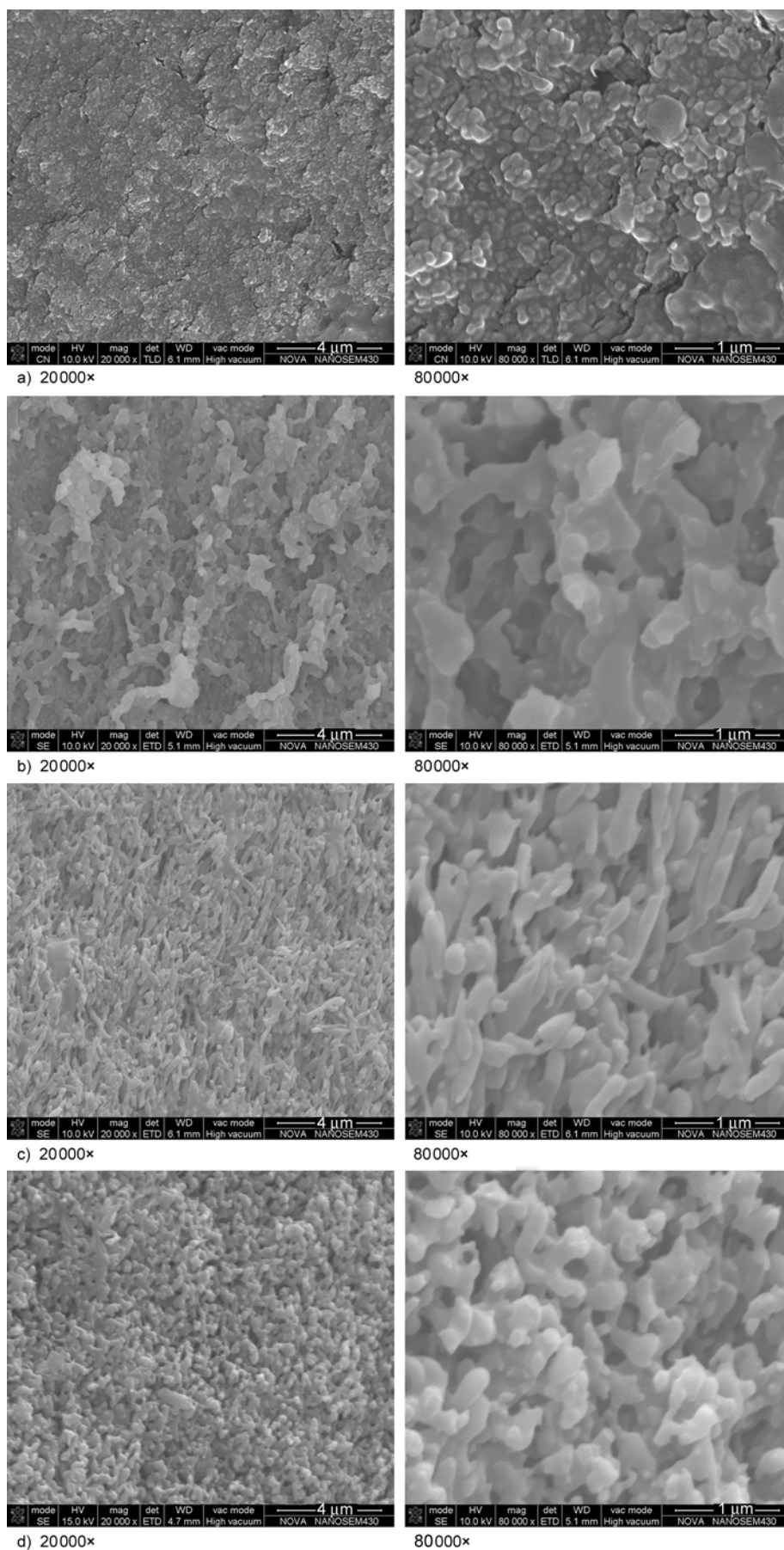


Figure 6. SEM images of the samples etched by toluene (a) *N*-SBR/50lignin, (b) *N*-SBR/50lignin/5F51, (c) *N*-SBR/50lignin/10F51, (d) *N*-SBR/50lignin/15F51

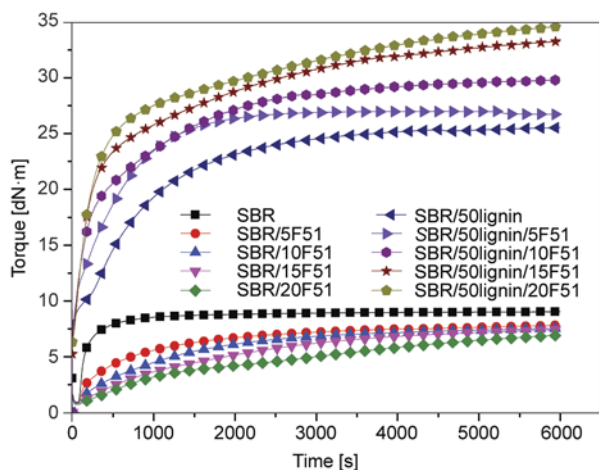


Figure 7. Curing curves of the SBR/F51 and SBR/50lignin/F51 compounds at 160°C

Table 2. Curing parameters of the rubber compounds (160°C)*

Samples	T _{S2} [min]	T ₉₀ [min]	M _L [dN·m]	M _H [dN·m]	ΔM [dN·m]
SBR	1.50	11.18	0.9.	9.03	8.13
SBR/5F51	3.26	46.28	0.85	7.81	6.96
SBR/10F51	7.03	51.12	0.84	7.53	6.69
SBR/15F51	10.32	66.06	0.76	7.44	6.68
SBR/20F51	12.52	78.30	0.70	6.93	6.20
SBR/50lignin	3.00	39.54	8.15	25.57	17.42
SBR/50lignin/5F51	0.44	22.42	7.92	27.02	19.10
SBR/50lignin/10F51	0.48	36.37	7.48	29.84	22.36
SBR/50lignin/15F51	0.45	48.58	7.24	33.30	26.06
SBR/50lignin/20F51	0.43	52.37	6.49	34.64	28.15

M_L: the minimum torque; M_H: the maximum torque; ΔM: the difference between maximum torque and minimum torque; T_{S2}: scorch time; T₉₀: optimum cure time.

F51 [27]. The T₉₀ of SBR and SBR/50lignin is 11.18 and 39.54 min respectively, indicating that incorporation of lignin in rubber matrix delays the vulcanization of rubber matrix, which is ascribed to the adsorption between lignin and vulcanization additives [14]. Compared to SBR/50lignin, the scorch time of SBR/50lignin/F51 are reduced, which is attributed to the reaction between lignin and F51. However, with the increasing loading of F51, T₉₀ of SBR/50lignin/F51 is initially decreased. When the F51 content is higher than 5 phr, T₉₀ starts to rise. There are three factors regulating the values of T₉₀ of SBR/50lignin/F51 compounds. Firstly, the interactions between F51 and lignin actually act as efficient crosslinks in the vulcanizates, resulting in accelerated vulcanization [28]. Secondly, F51 reacts with lignin which would adsorb vulcanization additives, and this two effects tend to promote the vulcanization. Thirdly, F51 consumed rubber additives

as mentioned above. This effect tends to delay the vulcanization. When the F51 content is relatively low (5 phr), the first and second effects play the leading role, resulting in accelerated curing behavior. When the F51 content is high enough (exceeding 5 phr), the consumption of the rubber additives by F51 plays the leading role, resulting in delayed curing behavior. The M_H of the SBR/50lignin/F51 is increased with F51 loading, suggesting more F51, more crosslinks between lignin and F51. While the M_L (the minimum torque) of the SBR/50lignin/F51 is decreased with F51 loading, and this is related to the fact that the F51 acts as a lubrication agent and plasticizer in the rubber compound. As it is known, a relatively low M_L suggested superior flow ability [29]. Therefore it could be concluded that the inclusion of F51 leads to a better processability.

3.3. RPA analysis results

RPA was used to analyze the dynamic viscoelastic properties of SBR/50lignin/F51 composites before and after curing. As shown in Figure 8, it is found that the modulus decreases dramatically with the increase of strain amplitude for all compounds, and this was because filler networks will be destroyed when the strain reaches a high amplitude, and the Storage modulus (G') of all compounds drops to almost the same low-value. This can be explained by the Payne effect [30]. As shown in Figure 8a, the initial modulus of SBR/50lignin uncured compound is higher than that of those uncured compounds adding F51. Moreover, with the increase of F51, the initial modulus of the compounds decreases, and this was because the F51 molecules act as plasticizers and lubricants. This is similar to the article of He et al. [31] that filler network interaction in SBR/rectorite was reduced by adding glycerin or aromatic oil. It indicates that adding F51 could weaken the filler network interaction and reduce the Payne effect, and then enhances the processability of the compounds.

As shown in Figure 8b, in vulcanized compounds, the values of G' are significantly higher than that of uncured material, this is due to formation of lignin-F51 networks and the crosslinked SBR networks after curing process and the networks restricting the mobility of rubber chains. The G' of the compounds increase with the loading of F51, and this can be ascribed to that more F51 lead to a stronger lignin-F51 networks and higher crosslink density, which

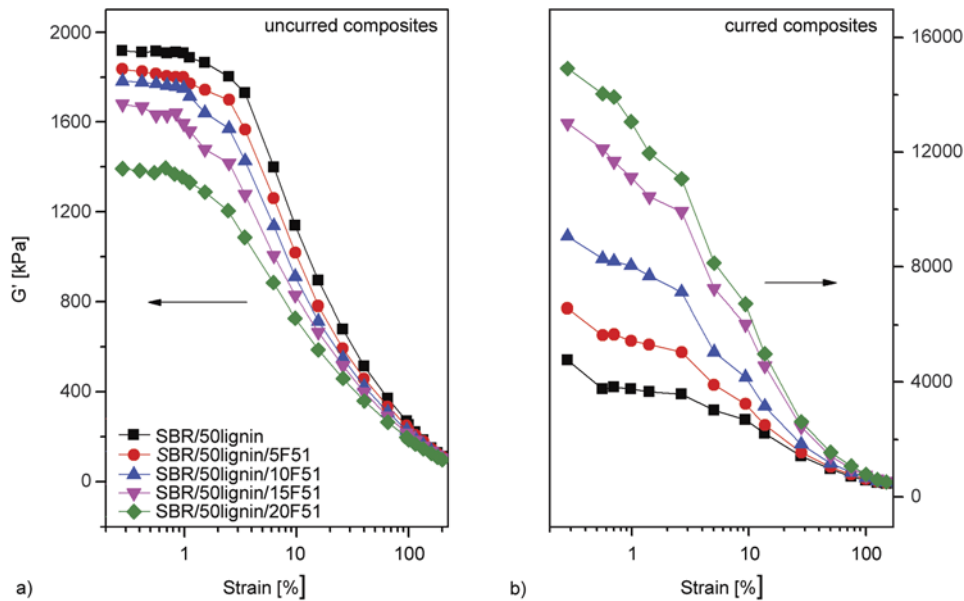


Figure 8. Storage modulus (G')-strain sweeps: (a) the uncured and (b) cured SBR/50lignin/F51 composites

further promote restriction on the mobility of rubber chains, indicating that the formation of the lignin-F51 networks have a significant reinforcement.

3.4. DMA analysis results

The dynamic mechanical properties of the SBR/50lignin/F51 composites were characterized by DMA. As shown in Figure 9a, there is an increase in storage modulus (E') after incorporation of F51, which can be attributed to the formation of strong lignin-F51 networks and the networks have a significant restriction on SBR matrix. E' is widely accepted as directly proportional to the degree of elasticity, which correlates well with crosslink density [30], and this is in accordance with our findings below.

As shown in Figure 9b. DMA studies reveal that the SBR/lignin/F51 composites exhibit two glass tran-

sition temperature: one occurring at low temperature (T_{g1}) is associated to SBR and the second at high temperature (T_{g2}) corresponds to the lignin-F51 networks. The T_{g1} of SBR is shifted from -56.63 to -55.15°C with increasing loading of F51 from 0 to 20 phr. Furthermore, it can be observed that the tan peak values and half-peak width of T_{g1} are decreased with the increase of F51 content, suggesting continuously decrease in rubber chain mobility [24, 32], and this is due to the strong interaction between the rigid lignin-F51 network and SBR matrix. There is an evident T_{g2} after incorporation of F51 at a level above 5 phr, and the tan peak of T_{g2} become increasingly obvious with the increasing loading of F51. It is logical to conclude that the T_{g2} is the glass transition temperature of lignin-F51 [33, 34]. The emergence of T_{g2} further substantiate the existence of the F51-lignin networks.

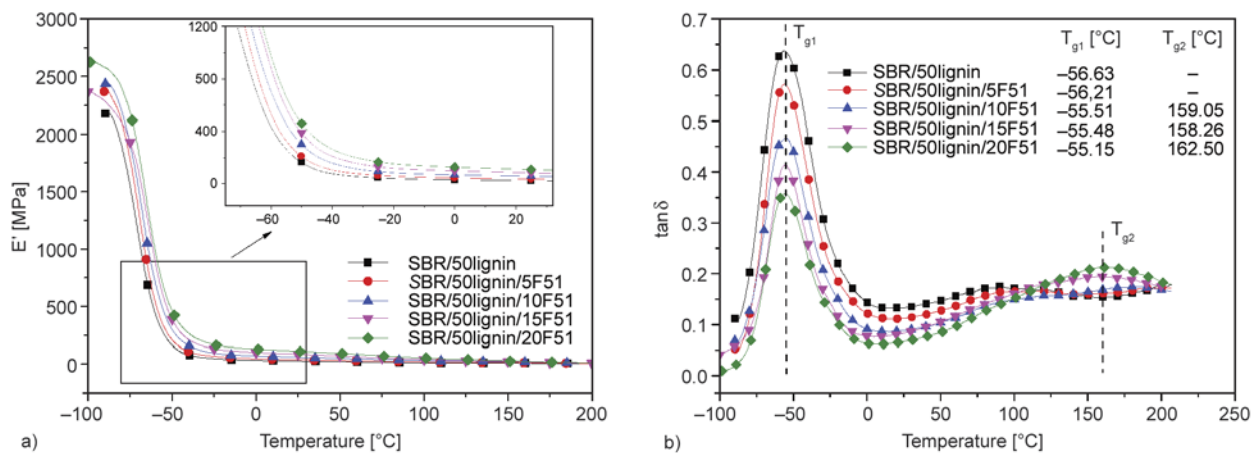


Figure 9. Storage modulus E' (a) and $\tan \delta$ (b) of SBR/50lignin/F51

3.5. TGA analysis results

Figure 10 illustrates the TG and DTG curves of SBR/50lignin/F51 with different F51 loading respectively. Table 3 shows the thermal degradation characteristics of the composites. The thermal degradation behavior of all SBR/50lignin/F51 composites with one main mass loss step are similar. A notable shift of 5, 10% weight loss to higher temperature can be observed with the loading of F51. For instance, the $T_{5\%}$ and $T_{10\%}$ of SBR/50lignin/20F51 is 274.7 and 336.0°C, which are about 25 and 10°C higher than those of SBR/50lignin, and this is attributed to the introduction of novolac epoxy resin with high concentrations of aromatic rings which can improve thermal stability [35] and lignin-F51 networks hindering the diffusion of small molecules generated during the thermal decomposition. Besides, to some extent the improvement of the crosslinking density can promote the thermal stability. However, the peak degradation temperature (T_{\max}) of SBR/50lignin/F51 is slightly lower than the T_{\max} of SBR/50lignin, which is attributed to the possibility of the epoxy resins decomposition at higher temperature.

Table 3. Thermal degradation characteristics of the rubber compounds*

Samples	$T_{5\%}$ [°C]	$T_{10\%}$ [°C]	T_{\max} [°C]	Residue at 700°C [%]
SBR/50lignin	249.4	325.4	456.9	14.2
SBR/50lignin/5F51	253.6	328.1	456.1	14.2
SBR/50lignin/10F51	265.6	334.1	455.9	14.8
SBR/50lignin/15F51	268.6	334.3	453.2	14.2
SBR/50lignin/20F51	274.7	336.0	453.4	14.9

* $T_{5\%}$ – 5% weight loss temperature. $T_{10\%}$ – 10% weight loss temperature. T_{\max} – the peak degradation temperature.

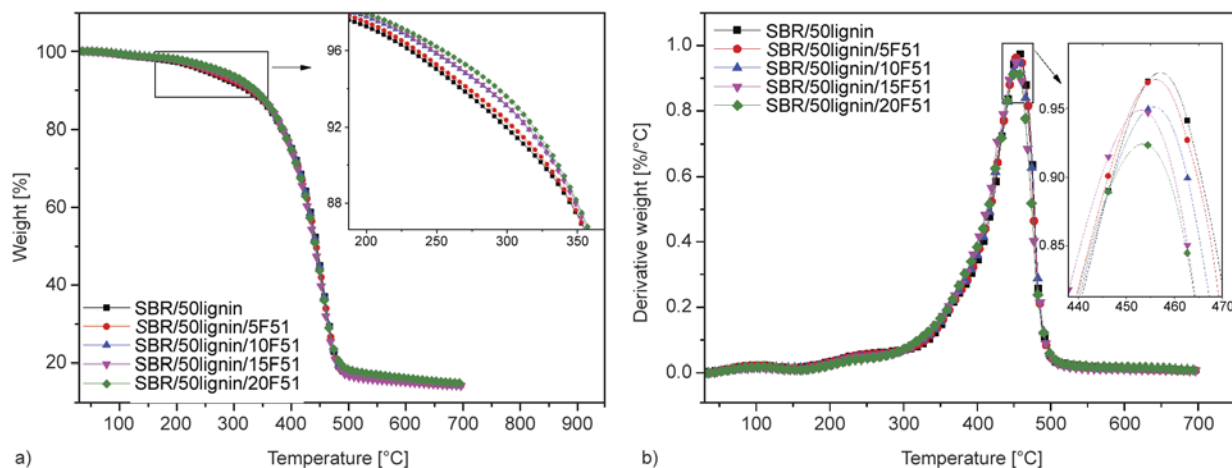


Figure 10. TGA curves (a) and DTG curves (b) of SBR/50lignin/F51

3.6. Crosslink density analysis

Recently, many researchers use Magnetic Resonance Crosslink Density Measurements to determine the crosslink densities in rubber materials [36–39], and not only this method simple to use and time-saving but also this method can provide several more parameters characterizing the molecular dynamics of the network. Such as the average molecular weight of chains between two adjacent crosslinks (M_c), the motion of dangling chain ends and free chain ($A(T_2)$), and the percentage of inter crosslink chain $A(M_c)$, etc. $A(T_2)$ represents the percentage of high-mobile fractions while $A(M_c)$ represents percentage of crosslinking fractions [40]. A less Crosslink Density value usually corresponds to a bigger M_c value [38, 41] and a less $A(T_2)$ value usually corresponds to a bigger $A(M_c)$ value [38]. The network structure characterization of vulcanizate with Magnetic Resonance Crosslink Density Measurements is described in detail in the references [42–44]. The results of crosslinking density are shown in Table 4, it is shown that the crosslink density of SBR vulcanizate is higher than that of SBR/50lignin, this is because that there are abundant acidic OH in lignin since acidic agents have an adverse effect on the vulcanization of the rubber [36]. The $A(T_2)$ of SBR vulcanizate is higher than that of SBR/50lignin. This is because that the addition of lignin could impose extra restriction to the mobility of the SBR and reduce the proportion of activity units. Compared to SBR/50lignin, the crosslink density of SBR/50lignin/F51 shows an increasing trend with the increase of F51, owing to the crosslink reaction between F51 and lignin. As the

Table 4. Crosslink density of SBR/50lignin/F51 compounds*

Properties	Samples(SBR/lignin/F51)					
	100/0/0	100/50/0	100/50/5	100/50/10	100/50/15	100/50/20
XLD [10^{-5} mol/cm ³]	9.33	9.18	9.35	9.43	9.69	10.15
M_c [K·g/mol]	10.18	10.35	10.16	10.07	9.80	9.36
$A(M_c)$ [%]	53.06	57.58	62.01	62.94	68.12	68.21
$A(T_2)$ [%]	46.33	40.60	37.02	35.03	32.90	31.59

*XLD: crosslinking density; M_c : the average molecular weight between two crosslinking point; $A(M_c)$: the motion of inter crosslink chain; $A(T_2)$: the motion of dangling chain ends and free chain.

integrity of crosslink network was improved, $A(M_c)$ increased and $A(T_2)$ decreased [38]. This result shows that the formation of lignin-F51 networks can bring on more crosslinking points, fewer activity units, and lower activity ability. The crosslink density results of SBR/50lignin/F51 is consistent with the maximum torque of curing test, Shore A hardness and tensile modulus.

3.7. Mechanical properties

As shown in Figure 11 and Table 5. It can be observed that the tensile strength of SBR and SBR/10F51 are very poor, indicating that F51 alone shows almost no reinforcing effect. It could be seen that the tear strength, 300% modulus and Shore A hardness of the SBR/50lignin/F51 composites increase with the increase of F51, for instance, the tear strength and 300% modulus are increased from 49.4 kN/m,

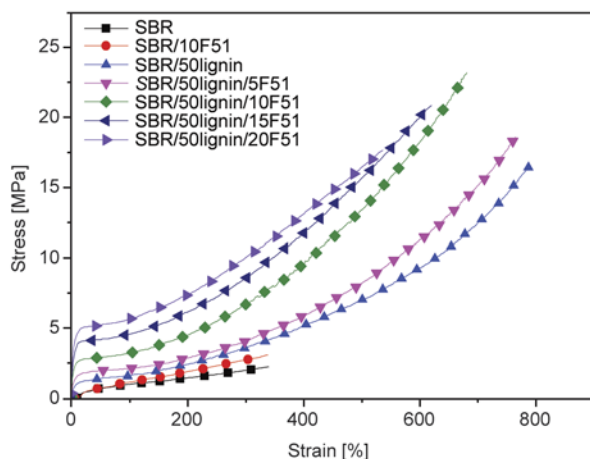


Figure 11. Stress-strain curve of the rubber composites

Table 5. Mechanical properties of rubber compounds

Properties	Samples(SBR/lignin/F51)						
	100/0/0	100/0/10	100/50/0	100/50/5	100/50/10	100/50/15	100/50/20
Modulus at 300% [MPa]	1.9	2.7	3.6	4.0	6.7	8.5	10.0
Tensile strength [MPa]	2.2	3.0	16.4	18.6	23.2	20.8	17.6
Elongation at break [%]	339.7	382.3	787.4	767.1	681.6	620.1	539.7
Permanent set [%]	8.0	8.0	32.0	36.0	60.0	59.0	60.0
Tear strength [kN/m]	10.9	11.9	49.4	52.6	57.6	60.4	62.2
Hardness [Shore A]	40.0	37.9	64.0	66.0	70.0	72.0	76.0

3.6 MPa of SBR/50lignin to 62.2kN/m and 10.0 MPa, respectively, when 20 phr F51 is added. This is because the stress will transfer from SBR molecular chains to the lignin-F51 networks effectively before a catastrophic breakage happens, which demonstrates the good reinforcement by the rigid lignin-F51 network. However, the elongation at break of SBR/50lignin/F51 decreases with the increase of F51content. This is because the lignin-F51 networks decrease the deformation resistance of rubber chains. Additionally, the strong interactions between the rigid lignin-F51 networks and SBR matrix can prevent the recovery of the rubber molecular chains after deformation, resulting in the increased permanent set.

As shown in Figure 12, the tensile fracture surface of SBR/50lignin and SBR/50lignin/20F51 are observed by SEM. It should be noted that the sample of SBR/50lignin/20F51 exhibits much more rugged fracture surfaces than those of SBR/50lignin, indicating that the lignin-F51 networks can bear more external force when an exerted stress is applied to the matrix. This investigation has demonstrated that lignin-F51 networks could be an effective route for the enhancement of SBR.

4. Conclusions

A novel reinforcing strategy for SBR via the lignin-F51 networks in the SBR matrix is proposed. The F51 can form covalent bonds with lignin via the ring-opening reaction between F51 and lignin, which is substantiated by the results of FTIR. The existence

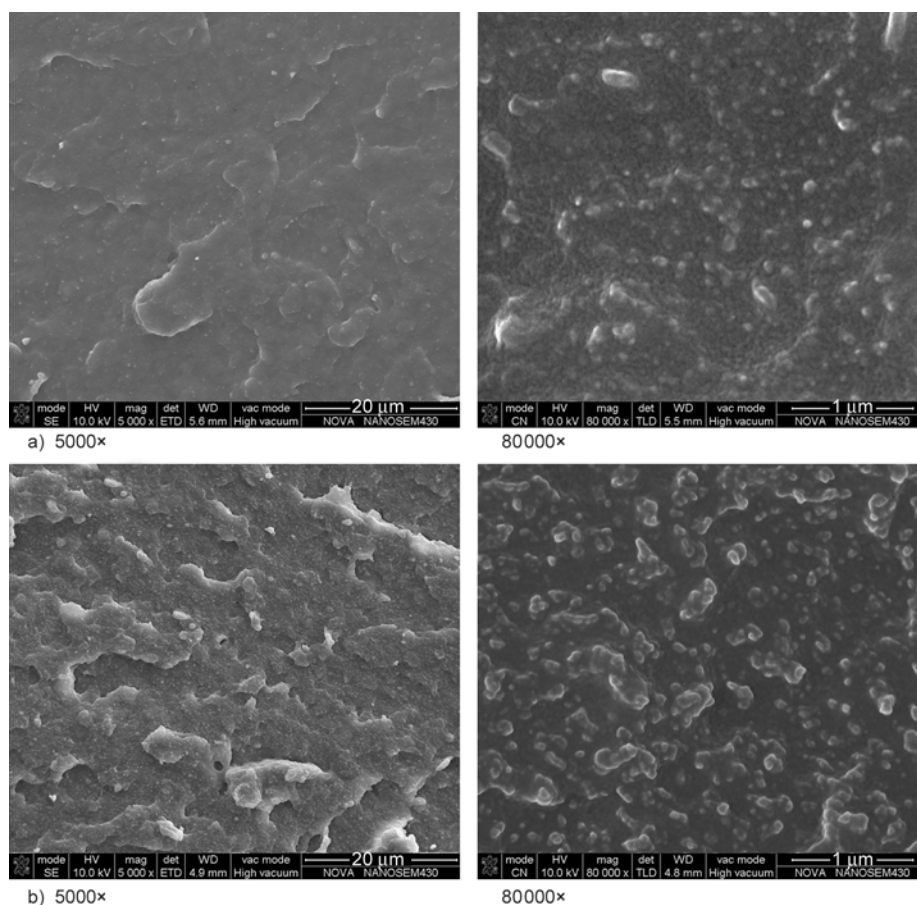


Figure 12. SEM images of the tensile fracture surfaces. (a) SBR/50lignin, (b) SBR/50lignin/20F51

of F51-lignin networks is demonstrated by the results of SEM and its glass transition temperature is observed by DMA. The lignin-F51 networks show good reinforcement towards the SBR compounds and improved initial thermal stability of the rubber composites. This novel reinforcing strategy is suitable for other rubbers, such as natural rubber and nitrile butadiene rubber, theoretically.

Acknowledgements

All the authors gratefully acknowledge National Natural Science Foundation of China (U1134005/L04) for financial supports.

References

- [1] Xiao S., Feng J., Zhu J., Wang X., Yi C., Su S.: Preparation and characterization of lignin-layered double hydroxide/styrene-butadiene rubber composites. *Journal of Applied Polymer Science*, **130**, 1308–1312 (2013). DOI: [10.1002/app.39311](https://doi.org/10.1002/app.39311)
- [2] Sadek E. M., El-Nashar D. E., Ahmed S. M.: Effect of organoclay reinforcement on the curing characteristics and technological properties of styrene-butadiene rubber. *Polymer Composites*, in press (2014). DOI: [10.1002/pc.23034](https://doi.org/10.1002/pc.23034)
- [3] Liu J., Liu H-F., Deng L., Liao B., Guo Q-X.: Improving aging resistance and mechanical properties of waterborne polyurethanes modified by lignin amines. *Journal of Applied Polymer Science*, **130**, 1736–1742 (2013). DOI: [10.1002/app.39267](https://doi.org/10.1002/app.39267)
- [4] Griffith T. R., MacGregor D. W.: Aids in vulcanization of lignin-natural rubber coprecipitates. Lead, copper, and bismuth oxides. *Rubber Chemistry and Technology*, **26**, 716–730 (1953). DOI: [10.5254/1.3539854](https://doi.org/10.5254/1.3539854)
- [5] Kumaran M. G., De S. K.: Utilization of lignins in rubber compounding. *Journal of Applied Polymer Science*, **22**, 1885–1893 (1978). DOI: [10.1002/app.1978.070220711](https://doi.org/10.1002/app.1978.070220711)
- [6] Kumaran M. G., Mukhopadhyay R., De S. K.: Network structure of lignin-filled natural rubber vulcanizate. *Journal of Polymer Science: Polymer Letters Edition*, **17**, 399–404 (1979). DOI: [10.1002/pol.1979.130170701](https://doi.org/10.1002/pol.1979.130170701)
- [7] Košíková B., Gregorová A.: Sulfur-free lignin as reinforcing component of styrene-butadiene rubber. *Journal of Applied Polymer Science*, **97**, 924–929 (2005). DOI: [10.1002/app.21448](https://doi.org/10.1002/app.21448)

- [8] Košíková B., Gregorová A., Osvald A., Krajčovičová J.: Role of lignin filler in stabilization of natural rubber-based composites. *Journal of Applied Polymer Science*, **103**, 1226–1231 (2007).
DOI: [10.1002/app.24530](https://doi.org/10.1002/app.24530)
- [9] Jiang C., He H., Jiang H., Ma L., Jia D. M.: Nano-lignin filled natural rubber composites: Preparation and characterization. *Express Polymer Letters*, **7**, 480–493 (2013).
DOI: [10.3144/expresspolymlett.2013.44](https://doi.org/10.3144/expresspolymlett.2013.44)
- [10] Jiang C., He H., Yu P., Wang D., Zhou L., Jia D. M.: Plane-interface-induced lignin-based nanosheets and its reinforcing effect on styrene-butadiene rubber. *Express Polymer Letters*, **8**, 619–634 (2014).
DOI: [10.3144/expresspolymlett.2014.66](https://doi.org/10.3144/expresspolymlett.2014.66)
- [11] Frigerio P., Zoia L., Orlandi M., Hanel T., Castellani L.: Application of lignin treated with hexamethylenetetramine as a filler for elastomers. *Bioresources*, **9**, 1387–1400 (2014).
- [12] Liao Z., Wang X., Xu Y., Feng J., Zhu J., Su S.: Cure characteristics and properties of NBR composites filled with co-precipitates of black liquor and montmorillonite. *Polymers for Advanced Technologies*, **23**, 1051–1056 (2012).
DOI: [10.1002/pat.2011](https://doi.org/10.1002/pat.2011)
- [13] Cao Z., Liao Z., Wang X., Su S., Feng J., Zhu J.: Preparation and properties of NBR composites filled with a novel black liquor–montmorillonite complex. *Journal of Applied Polymer Science*, **127**, 3725–3730 (2013).
DOI: [10.1002/app.37984](https://doi.org/10.1002/app.37984)
- [14] Bahl K., Jana S. C.: Surface modification of lignosulfonates for reinforcement of styrene–butadiene rubber compounds. *Journal of Applied Polymer Science*, **131**, 40123/1–40123/9 (2014).
DOI: [10.1002/app.40123](https://doi.org/10.1002/app.40123)
- [15] Bahl K., Miyoshi T., Jana S. C.: Hybrid fillers of lignin and carbon black for lowering of viscoelastic loss in rubber compounds. *Polymer*, **55**, 3825–3835 (2014).
DOI: [10.1016/j.polymer.2014.06.061](https://doi.org/10.1016/j.polymer.2014.06.061)
- [16] Abdul Khalil H., Marliana M., Alshammari T.: Material properties of epoxy-reinforced biocomposites with lignin from empty fruit bunch as curing agent. *Bioresources*, **6**, 5206–5223 (2011).
- [17] Yin Q., Yang W., Sun C., Di M.: Preparation and properties of lignin-epoxy resin composite. *Bioresources*, **7**, 5737–5748 (2012).
- [18] Jiang C., He H., Yao X., Yu P., Zhou L., Jia D.: Self-crosslinkable lignin/epoxidized natural rubber composites. *Journal of Applied Polymer Science*, in press (2014).
DOI: [10.1002/app.41166](https://doi.org/10.1002/app.41166)
- [19] Ye L.: Performance and mechanism of epoxy resin for reinforcement of styrene–butadiene rubber. *Journal of Macromolecular Science Part B: Physics*, **50**, 1771–1779 (2011).
DOI: [10.1080/00222348.2010.549062](https://doi.org/10.1080/00222348.2010.549062)
- [20] Tan J. H., Wang X. P., Tai J. J., Luo Y. F., Jia D. M.: Novel blends of acrylonitrile butadiene rubber and polyurethane-silica hybrid networks. *Express Polymer Letters*, **6**, 588–600 (2012).
DOI: [10.3144/expresspolymlett.2012.62](https://doi.org/10.3144/expresspolymlett.2012.62)
- [21] Jiang X. L., Hu K., Yang P., Ren J.: Study on preparation and properties of water swellable rubber modified by interpenetrating polymer networks. *Plastics, Rubber and Composites*, **42**, 327–333 (2013).
DOI: [10.1179/1743289812y.0000000027](https://doi.org/10.1179/1743289812y.0000000027)
- [22] Su C., Zong D., Xu L., Zhang C.: Dynamic mechanical properties of semi-interpenetrating polymer network-based on nitrile rubber and poly(methyl methacrylate-*co*-butyl acrylate). *Journal of Applied Polymer Science*, **131**, in press (2014).
DOI: [10.1002/app.40217](https://doi.org/10.1002/app.40217)
- [23] Imbernon L., Pire M., Oikonomou E. K., Norvez S.: Semi-interpenetrating networks in blends of epoxidized natural rubbers. *Macromolecular Chemistry and Physics*, **214**, 806–811 (2013).
DOI: [10.1002/macp.201200671](https://doi.org/10.1002/macp.201200671)
- [24] Chen W., Wu S., Lei Y., Liao Z., Guo B., Liang X., Jia D.: Interfacial structure and performance of rubber/boehmite nanocomposites modified by methacrylic acid. *Polymer*, **52**, 4387–4395 (2011).
DOI: [10.1016/j.polymer.2011.07.028](https://doi.org/10.1016/j.polymer.2011.07.028)
- [25] Leblanc J. L.: Rubber–filler interactions and rheological properties in filled compounds. *Progress in Polymer Science*, **27**, 627–687 (2002).
DOI: [10.1016/S0079-6700\(01\)00040-5](https://doi.org/10.1016/S0079-6700(01)00040-5)
- [26] Sheng E., Sutherland I., Bradley R. H., Freakley P. K.: Effects of a multifunctional additive on bound rubber in carbon black and silica filled natural rubbers. *European Polymer Journal*, **32**, 35–41 (1996).
DOI: [10.1016/0014-3057\(95\)00107-7](https://doi.org/10.1016/0014-3057(95)00107-7)
- [27] Gong Z-L., Cen L., Wang S-T., Chen F-L.: Synthesis and characterization of maleated glycidyl 3-pentadecenyl phenyl ether as a functionalized plasticizer for styrene–butadiene rubber/carbon black/silica composites. *Journal of Applied Polymer Science*, **131**, in press (2014).
DOI: [10.1002/app.40462](https://doi.org/10.1002/app.40462)
- [28] Du M., Guo B., Lei Y., Liu M., Jia D.: Carboxylated butadiene–styrene rubber/halloysite nanotube nanocomposites: Interfacial interaction and performance. *Polymer*, **49**, 4871–4876 (2008).
DOI: [10.1016/j.polymer.2008.08.042](https://doi.org/10.1016/j.polymer.2008.08.042)
- [29] Gu J., Chen W-J., Lin L., Luo Y-F., Jia D-M.: Effect of nanocrystalline cellulose on the curing characteristics and aging resistance properties of carbon black reinforced natural rubber. *Chinese Journal of Polymer Science*, **31**, 1382–1393 (2013).
DOI: [10.1007/s10118-013-1340-6](https://doi.org/10.1007/s10118-013-1340-6)
- [30] Cao X., Xu C., Wang Y., Liu Y., Liu Y., Chen Y.: New nanocomposite materials reinforced with cellulose nanocrystals in nitrile rubber. *Polymer Testing*, **32**, 819–826 (2013).
DOI: [10.1016/j.polymertesting.2013.04.005](https://doi.org/10.1016/j.polymertesting.2013.04.005)

- [31] He S., Zhang L., Wu X., Lin J., Xi M., Wang Y.: Reduction of the filler network interaction in novel inner liner compound based on SBR/rectorite nanocomposite by glycerin. *Polymer Composites*, **33**, 336–342 (2012).
DOI: [10.1002/pc.22152](https://doi.org/10.1002/pc.22152)
- [32] Laskowska A., Zaborski M., Boiteux G., Gain O., Marzec A., Maniukiewicz W.: Ionic elastomers based on carboxylated nitrile rubber (XNBR) and magnesium aluminum layered double hydroxide (hydrotalcite). *Express Polymer Letters*, **8**, 374–386 (2014).
DOI: [10.3144/expresspolymlett.2014.42](https://doi.org/10.3144/expresspolymlett.2014.42)
- [33] Komiya G., Imai T., Happoya A., Fukumoto T., Sagae H., Sone N., Takahashi A.: Effects of lignin derivatives on cross-link density and dielectric properties in the epoxy-based insulating materials for printed circuit boards. *IEEE Transactions on Components Packaging and Manufacturing Technology*, **3**, 1057–1062 (2013).
DOI: [10.1109/tcpmt.2013.2253836](https://doi.org/10.1109/tcpmt.2013.2253836)
- [34] Shin S., Lim D. G., Kang T., Chun H., Cho J. K.: Thermal and electrical properties of glass fiber reinforced o-cresol novolac epoxy composites cured with allylated phenol novolac hardener. *Polymer International*, **61**, 1411–1416 (2012).
DOI: [10.1002/pi.4224](https://doi.org/10.1002/pi.4224)
- [35] Lin J., Wu X., Zheng C., Zhang P., Li Q., Wang W., Yang Z.: A novolac epoxy resin modified polyurethane acylates polymer grafted network with enhanced thermal and mechanical properties. *Journal of Polymer Research*, **21**, 435/1–435/10 (2014).
DOI: [10.1007/s10965-014-0435-2](https://doi.org/10.1007/s10965-014-0435-2)
- [36] Dong Z.-X., Liu M.-X., Jia D.-M., Zhou Y.-H.: Synthesis of natural rubber-g-maleic anhydride and its use as a compatibilizer in natural rubber/short nylon fiber composites. *Chinese Journal of Polymer Science*, **31**, 1127–1138 (2013).
DOI: [10.1007/s10118-013-1310-z](https://doi.org/10.1007/s10118-013-1310-z)
- [37] Sun X., Zhao F., Zhao S.: Study on dynamic fatigue properties of solution-polymerized styrene butadiene rubber T2000R. *Journal of Elastomers and Plastics*, **43**, 469–480 (2011).
DOI: [10.1177/0095244311402634](https://doi.org/10.1177/0095244311402634)
- [38] Wang X., Feng N., Chang S.: Effect of precured degrees on morphology, thermal, and mechanical properties of BR/SBR/NR foams. *Polymer Composites*, **34**, 849–859 (2013).
DOI: [10.1002/pc.22489](https://doi.org/10.1002/pc.22489)
- [39] Hu M., Zhao S., Li C., Wang B., Yao C., Wang Y.: The influence of different Tween surfactants on biodesulfurization of ground tire rubber by *Sphingomonas* sp. *Polymer Degradation and Stability*, **107**, 91–97 (2014).
DOI: [10.1016/j.polymdegradstab.2014.04.025](https://doi.org/10.1016/j.polymdegradstab.2014.04.025)
- [40] Liu X., Zhao S., Zhang X., Li X., Bai Y.: Preparation, structure, and properties of solution-polymerized styrene-butadiene rubber with functionalized end-groups and its silica-filled composites. *Polymer*, **55**, 1964–1976 (2014).
DOI: [10.1016/j.polymer.2014.02.067](https://doi.org/10.1016/j.polymer.2014.02.067)
- [41] Peng Z., Feng C., Luo Y., Yi Z., Kong L.: Structure and properties of self-assembled natural rubber/multi-walled carbon nanotube composites. *Journal of Wuhan University of Technology-Materials Science Edition*, **26**, 807–811 (2011).
DOI: [10.1007/s11595-011-0315-0](https://doi.org/10.1007/s11595-011-0315-0)
- [42] Grinberg F., Garbarczyk M., Kuhn W.: Influence of the cross-link density and the filler content on segment dynamics in dry and swollen natural rubber studied by the NMR dipolar-correlation effect. *The Journal of Chemical Physics*, **111**, 11222–11231 (1999).
DOI: [10.1063/1.480478](https://doi.org/10.1063/1.480478)
- [43] Garbarczyk M., Grinberg F., Nestle N., Kuhn W.: A novel approach to the determination of the crosslink density in rubber materials with the dipolar correlation effect in low magnetic fields. *Journal of Polymer Science Part B: Polymer Physics*, **39**, 2207–2216 (2001).
DOI: [10.1002/polb.1194](https://doi.org/10.1002/polb.1194)
- [44] Grinberg F., Heidenreich M., Kuhn W.: A new contrast parameter for visualization of the cross-link density in rubber based on the dipolar-correlation effect. *Journal of Magnetic Resonance*, **159**, 87–91 (2002).
DOI: [10.1016/S1090-7807\(02\)00007-1](https://doi.org/10.1016/S1090-7807(02)00007-1)

Enhancing the mechanical properties of electrospun polyester mats by heat treatment

M. Kancheva^{1,2}, A. Toncheva¹, N. Manolova¹, I. Rashkov^{1*}

¹Laboratory of Bioactive Polymers, Institute of Polymers, Bulgarian Academy of Sciences, Acad. G. Bonchev St, bl. 103A, BG-1113 Sofia, Bulgaria

²Technical University of Gabrovo, 4 H. Dimitar St, Gabrovo BG-5300, Bulgaria

Received 31 May 2014; accepted in revised form 9 August 2014

Abstract. Microfibrous materials with a targeted design based on poly(L-lactic acid) (PLA) and poly(ϵ -caprolactone) (PCL) were prepared by electrospinning and by combining electrospinning and electrospraying. Several approaches were used: (i) electrospinning of a common solution of the two polymers, (ii) simultaneous electrospinning of two separate solutions of PLA and PCL, (iii) electrospinning of PLA solution in conjunction with electrospraying of PCL solution, and (iv) alternating layer-by-layer deposition by electrospinning of separate PLA and PCL solutions. The mats were heated at the melting temperature of PCL (60°C), thus achieving melting of PCL fibers/particles and thermal sealing of the fibers. The mats subjected to thermal treatment were characterized by greater mean fiber diameters and reduced values of the water contact angle compared to the pristine mats. Heat treatment of the mats affected their thermal stability and led to an increase in the crystallinity degree of PLA incorporated in the mats, whereas that of PCL was reduced. All mats were characterized by enhanced mechanical properties after thermal treatment as compared to the non-treated fibrous materials.

Keywords: *nanomaterials, electrospinning, poly(L-lactic acid), poly(ϵ -caprolactone), thermal sealing*

1. Introduction

During the last decade nanotechnologies have made a remarkable progress in the development of novel materials with a design and properties which have been unknown until now. Electrospinning and electrospraying are two particularly attractive processes for the preparation of micro- and nano-structured polymeric materials. Electrospinning is a technology used for the preparation of micro- and nanofibers with a length of up to several tens of meters. Because of the various morphologies, large specific surface area and porous structure, mats find application in medicine (mats with antitumor, antibacterial or hemostatic activity), pharmacy (drug carriers), for immobilization of enzymes for water purification or for the preparation of fibrous materials with magnetic properties [1–6]. Electrospraying allows

the fabrication of micro- and nanoparticles, which can serve as drug carriers for the preparation of micro- and nanofilms for electroencapsulation, in direct electrowriting, etc. [7–9]. The possibility for combining the two processes with the purpose of creating a novel generation of fibrous materials decorated with micro- or nanoparticles is particularly attractive [10, 11]. The combination of the two methods is still scarcely reported.

Despite the above-described advantages of the fibrous materials it is known that they are characterized by poor mechanical properties. One of the possible routes for enhancement of the strength of the mats is based on heating them at temperatures close to and above the melting temperature (T_m) of the polymer(s) they are composed of. In the majority of cases the thermal treatment of the mats enables the

*Corresponding author, e-mail: rashkov@polymer.bas.bg

preparation of polymeric materials, in which the fibrous structure is partially or completely lost, and the pristine fibers are interconnected forming a network. A limited number of studies on the enhancement of the mechanical properties of fibrous materials by thermal treatment exist in the literature. Improvement of the mechanical properties of polysulfonic fibers [12], poly(L-lactic acid) (PLA) fibers [13] or fibers from PLA with incorporated multi-wall carbon nanotubes [14] has been achieved by heat treatment. Lee *et al.* [15] have prepared poly(ϵ -caprolactone) (PCL)/Pluronic F127 scaffolds with enhanced mechanical properties after heat treatment suitable for tissue engineering applications. Based on the literature review it can be concluded that up to date no data is available about the preparation of mats from two or more polymers with enhanced mechanical parameters after heat treatment and by combining the electrospinning and electrospaying techniques.

In the present study the preparation of mats with a desired structural hierarchy on a micro- and nano-level by combining the electrospinning and electrospaying processes has been discussed. Two biodegradable and biocompatible polymers with versatile medical applications: PLA with a high melting temperature ($T_m = 165^\circ\text{C}$) and PCL with a lower melting temperature ($T_m = 60^\circ\text{C}$) were used. It was the difference in the thermal behavior of the polymers that allowed the preparation of fibrous materials with an original design and desired mechanical characteristics. Fibrous materials were fabricated by: (i) electrospinning of a common solution of the two polymers, (ii) simultaneous electrospinning of two separate solutions of PLA and PCL, (iii) simultaneous electrospinning (PLA) and electrospaying (PCL) of two separate solutions, and (iv) alternating, layer-by-layer deposition by electrospinning of PLA and PCL solutions. The obtained materials are further designated as PLA/PCL mats, PLA_{elspin}/PCL_{elspin} mats, PLA_{elspin}/PCL_{elspray} mats, and 'sandwich'-type mats. The electrospun mats were heated at T_m of PCL (60°C), thus enabling the thermal sealing of the fibers by molten PCL fibers/particles. Special attention has been paid to the structure-properties relationship of the fibrous material before and after heat treatment. The morphology and topology of the mats was assessed by scanning electron microscopy (SEM) and fluorescence microscopy.

The hydrophilic/hydrophobic properties of the mats were evaluated by measuring the water contact angle. The crystallinity degree of the polymers and the thermal stability of the mats before and after heat treatment were determined by differential scanning calorimetry (DSC) and thermogravimetric analysis (TGA). The tensile behavior of the mats was also assessed.

2. Experimental section

2.1. Materials

Poly(L-lactic acid) (PLA, Sigma-Aldrich, Germany) with a $\bar{M}_w = 96\,000$ g/mol and $\bar{M}_w/\bar{M}_n = 1.75$; poly(ϵ -caprolactone) (PCL, CAPA 6800, Perstorp, Sweden) of mean molecular weight 80 000 g/mol; and fluorescein (F-free acid, Sigma-Aldrich, Germany) were used. Dichloromethane (DCM) and dimethylformamide (DMF) were supplied by Merck, Germany and dimethylsulfoxide (DMSO) was purchased from Sigma-Aldrich, Germany.

2.2. Preparation of fibrous materials

2.2.1. Preparation of fibrous materials by electrospinning of a single solution

In the present study PLA, PCL mats and mats composed of fibers containing PLA and PCL in various weight ratios – 75/25, 60/40 or 50/50 wt/wt (PLA₇₅/PCL₂₅, PLA₆₀/PCL₄₀ and PLA₅₀/PCL₅₀ mats) were fabricated by electrospinning a single spinning solution using one syringe. Fibrous materials with a 'sandwich' type structure were prepared, as well. This was achieved by consecutive electrospinning of PLA or PCL solutions onto one and the same collector followed by electrospinning of a PCL or PLA solution, respectively. The 'sandwich' type mats composed of initially deposited PLA fibers and a PCL fiber layer on top are denoted as 'sandwich' PLA+PCL. In the case when PLA fibers are deposited on top of PCL fibers the mats are designated as 'sandwich' PCL+PLA. A schematic of the electrospinning setup used for preparation of the described fibrous materials is presented in Figure 1a.

PLA and PCL fibers, as well as 'sandwich' type mats were prepared from 9 wt% polymer solutions of PLA in DCM/DMSO (75/25 wt/wt) and of PCL in DCM/DMF (93/7 wt/wt). PLA/PCL fibers were obtained after dissolving the respective amounts of polymers in the required volume of DCM/DMSO (75/25 wt/wt) with a total polymer concentration of 9 wt%.

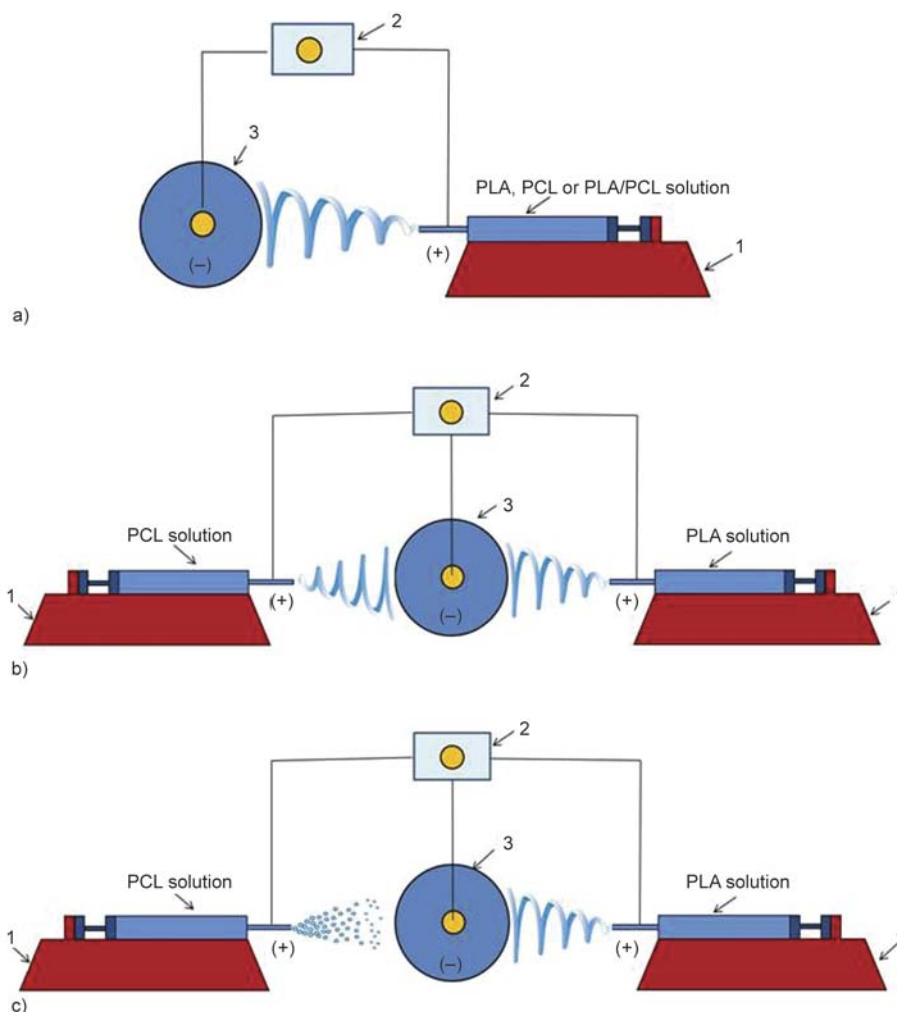


Figure 1. Schematic representation of the setup used for electrospinning of a single solution [PLA, PCL, PLA/PCL or ‘sandwich’ type (PLA+PCL or PCL+PLA) mats] (a); for simultaneous electrospinning of two separate solutions (PLA_{elspin}/PCL_{elspin} mats) (b) or for simultaneous electrospinning and electro spraying of two separate solutions (PLA_{elspin}/PCL_{elspray} mats) (c); 1 – pump, 2 – high voltage power supply and 3 – rotating collector

2.2.2. Preparation of fibrous materials by simultaneous electrospinning of two separate solutions

Microfibrous materials were prepared by simultaneous electrospinning of two separate PLA and PCL spinning solutions using two separate syringes (Figure 1b). The mats are denoted as PLA_{elspin}/PCL_{elspin} and depending on the flow rate of the solutions they are designated as: PLA_{elspin(3)}/PCL_{elspin(1)} (3 mL/h for PLA solution and 1 mL/h for PCL solution), PLA_{elspin(3)}/PCL_{elspin(2)} (3 mL/h and 2 mL/h) and PLA_{elspin(3)}/PCL_{elspin(3)} (3 mL/h and 3 mL/h). The polymer concentration of the PLA and PCL spinning solutions was 9 wt% and DCM/DMSO (75/25 wt/wt) and DCM/DMF (93/7 wt/wt) solvent systems were used, respectively.

2.2.3. Preparation of fibrous materials by simultaneous electrospinning and electro spraying of two separate solutions

Mats were prepared by simultaneous electrospinning of a PLA solution and electro spraying of a PCL solution using two separate syringes (Figure 1c). The fibrous materials are denoted as PLA_{elspin}/PCL_{elspray}. Depending on the flow rate of the solutions the mats are marked as: PLA_{elspin(3)}/PCL_{elspray(1)} (3 mL/h for PLA solution and 1 mL/h for PCL solution), PLA_{elspin(3)}/PCL_{elspray(2)} (3 mL/h and 2 mL/h) and PLA_{elspin(3)}/PCL_{elspray(3)} (3 mL/h and 3 mL/h). In this case the concentration of the PLA solution was 9 wt% (DCM/DMSO = 75/25 wt/wt), and that of PCL – 0.4 wt% (DCM/DMF = 93/7 wt/wt). Regardless of the method used for preparation of the mats (electrospinning or electro spraying) the

collector rotation rate was 600 rpm. The conditions employed for preparation of PLA and PLA/PCL mats were: applied voltage of 17 kV, tip-to-collector distance – 10 cm and solution feed rate of 3 mL/h. In the case of the PCL mat the applied voltage was 20 kV, the distance from the capillary tip to the collector – 15 cm and the solution feed rate – 1 mL/h. The PLA+PCL and PCL+PLA ‘sandwich’ type mats were prepared by electrospinning a PLA solution at a voltage of 17 kV, tip-to-collector distance of 10 cm and a solution feed rate of 3 mL/h, and a PCL solution at a voltage of 20 kV, distance from the capillary tip to the collector – 15 cm and a solution feed rate of 1 mL/h. For the preparation of a PLA_{elspin}/PCL_{elspin} mat a PLA solution was electrospun at a voltage of 17 kV, tip-to-collector distance of 10 cm and a solution feed rate of 3 mL/h, and a PCL solution – at a voltage of 20 kV, a working distance of 15 cm and a feed rate of 1, 2 or 3 mL/h. In the case of PLA_{elspin}/PCL_{elspray} non-woven textile a PLA solution was electrospun under the same conditions used for preparation of the PLA_{elspin}/PCL_{elspin} mats, whereas the PCL solution was subjected to electro-spraying at a voltage of 20 kV, tip-to-collector distance of 10 cm and a solution flow rate of 1, 2 or 3 mL/h.

2.3. Heat treatment of the fibrous materials

The electrospun mats were placed in a vacuum oven (Laboratory vacuum oven Binder, Germany) and heated at 60±0.1°C for 15 min with the purpose of achieving thermal sealing of the fibers by the molten PCL fibers/particles. The fibrous materials were heated without removing the aluminum foil onto which they were electrospun in order to prevent folding of the mats during their thermal treatment.

2.4. Characterization of the electrospun materials

The morphology of the mats before and after heat treatment was assessed by scanning electron microscopy (SEM). The samples were vacuum-coated with gold and subsequently observed by SEM (Jeol JSM-5510, Jeol Ltd., Tokyo, Japan and Philips SEM 515, Netherlands). The mean fiber diameter was determined by measuring at least 20 fibers from a SEM micrograph using Image J software [16]. Further evidence for the melting of the PCL fibers/particles was provided by incorporation of fluores-

cein (F) in the PCL solution (PCL^F) and subsequent observation of the fibrous materials by fluorescence microscopy (NU-2, Carl Zeiss Jena, Germany). Micrographs of one and the same sample fragment were taken before and after turning a fluorescence light source on. For the sake of comparison the mats were observed prior to heating them at 60°C, as well. The thermal behavior of the obtained fibrous materials was evaluated by differential scanning calorimetry (DSC). The samples were heated in the temperature range from –80 to 250°C at heating rate of 10°C/min under nitrogen (TA Instruments, DSC Q2000, USA). The crystallinity degree (χ_c) of the polymers χ_c^{PLA} for PLA and χ_c^{PCL} for PCL in the fibrous materials was calculated using Equations (1) and (2):

$$\chi_c^{\text{PLA}} [\%] = \frac{\Delta H_m^{\text{PLA}} - \Delta H_{cc}^{\text{PLA}}}{\Delta H_m^{\text{PLA},0} \cdot W^{\text{PLA}}} \cdot 100 \quad (1)$$

$$\chi_c^{\text{PCL}} [\%] = \frac{\Delta H_m^{\text{PCL}} - \Delta H_{cc}^{\text{PCL}}}{\Delta H_m^{\text{PCL},0} \cdot W^{\text{PCL}}} \cdot 100 \quad (2)$$

where W^{PLA} is the weight fraction of PLA, and W^{PCL} – the weight fraction of PCL; ΔH_m^0 is the melting enthalpy when the respective polymer is in a 100% crystalline state: $\Delta H_m^{\text{PLA},0} = 93.0$ J/g [17]; $\Delta H_m^{\text{PCL},0} = 139.5$ J/g [18]; $\Delta H_{cc}^{\text{PLA}}$ and $\Delta H_{cc}^{\text{PCL}}$ is the enthalpy at the temperature of cold crystallization of the respective polymer. Thermogravimetric analysis (TGA, TA Instruments TGA Q5000, USA) of the mats was performed by heating the samples up to 800°C.

The water contact angles of the fibrous materials were measured using an Easy Drop DSA20E KRÜSS GmbH apparatus, Germany. Drops of distilled water with a volume of 10 μL were deposited on the surface of the test specimens (cut in the direction of the collector rotation). The mean contact angle value was determined after averaging at least 10 measurements for each specimen.

2.5. Mechanical behaviour of the fibrous materials

The tensile characteristics of the fibers were evaluated using a Zwick/Roell Z 2.5 apparatus, Germany load cell 2 mV/V, type Xforce P, nominal force 2.5 kN, test Xpert II. Strain rate – 20 mm/min and room temperature – 21°C. All samples were cut in the direction of collector rotation with dimensions of 20×60 mm and a thickness of ca. 200 μm . For the

sake of statistical significance 10 specimens of each sample were tested, after which the average values of Young’s modulus, the ultimate stress and maximum deformation at break were determined.

3. Results and discussion

3.1. Morphology and topological alterations in the electrospun mats before and after heat treatment

3.1.1. Morphology and topology of the fibers prepared by electrospinning of a single solution

The electrospinning of the solutions resulted in the preparation of randomly deposited defect-free fibers, and in the case of electrospinning – of particles. SEM micrographs of the fibrous materials (before and after heat treatment) are shown in Figure 2. The mean diameter of the PLA fibers was ca. 1170 ± 220 nm, and that of PCL fibers before heating was twice as small (515 ± 125 nm). The smaller

average diameter of the PCL fibers can be attributed to the lower feed rate of the spinning solution (1 mL/h) as compared to the PLA solution – 3 mL/h. The heat treatment of the PCL mat led to substantial alterations in the fiber morphology and the mat topology (Figure 2), whereat the fibers lost their cylindrical shape. The single melted PCL fibers were connected by zones of PCL fusion. The size of the sites of merging and the voids in the material can be controlled by heating of mats with a different thickness.

SEM micrographs of mats prepared by electrospinning of common PLA/PCL solutions are presented in Figure 2. In these cases interconnecting of the PLA fibers was attained by thermal sealing in the intersections, whereat a continuous network was formed (Figure 2, after heating). It was found that on increasing the PCL content in the pristine PLA/PCL mats, a denser network of interconnected fibers was formed after thermal treatment. The mean fiber diameter

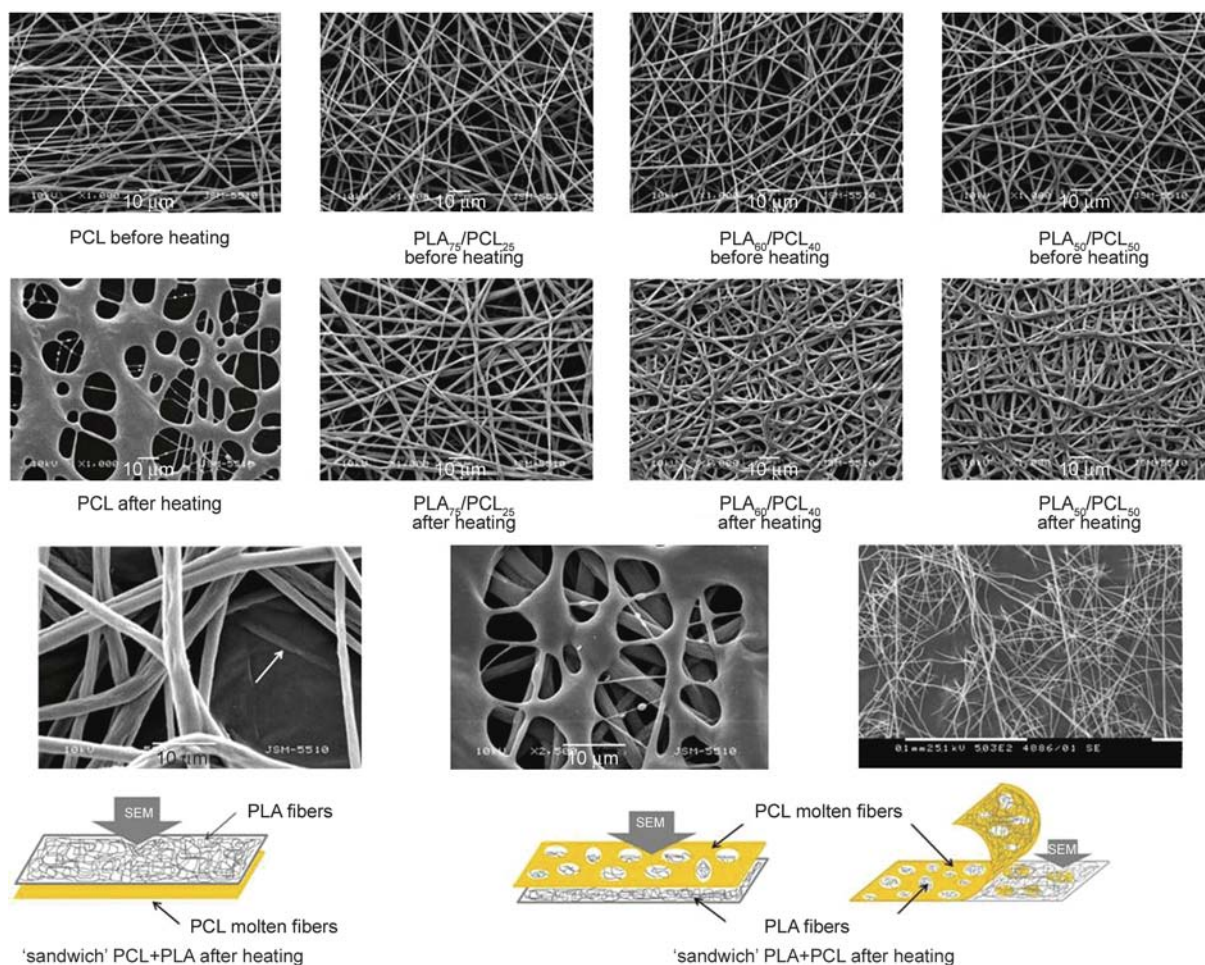


Figure 2. SEM micrographs of PCL, PLA/PCL and ‘sandwich’ type PCL+PLA and PLA+PCL mats before and after heating at 60°C; magnification $\times 1000$. For ‘sandwich’ type fibrous materials the position of taking the micrographs (the surface or the bulk of the mat) is schematically presented. The arrow in the SEM micrograph of the ‘sandwich’ PCL+PLA after heating indicates a PLA fiber submerged in the molten PCL fibers.

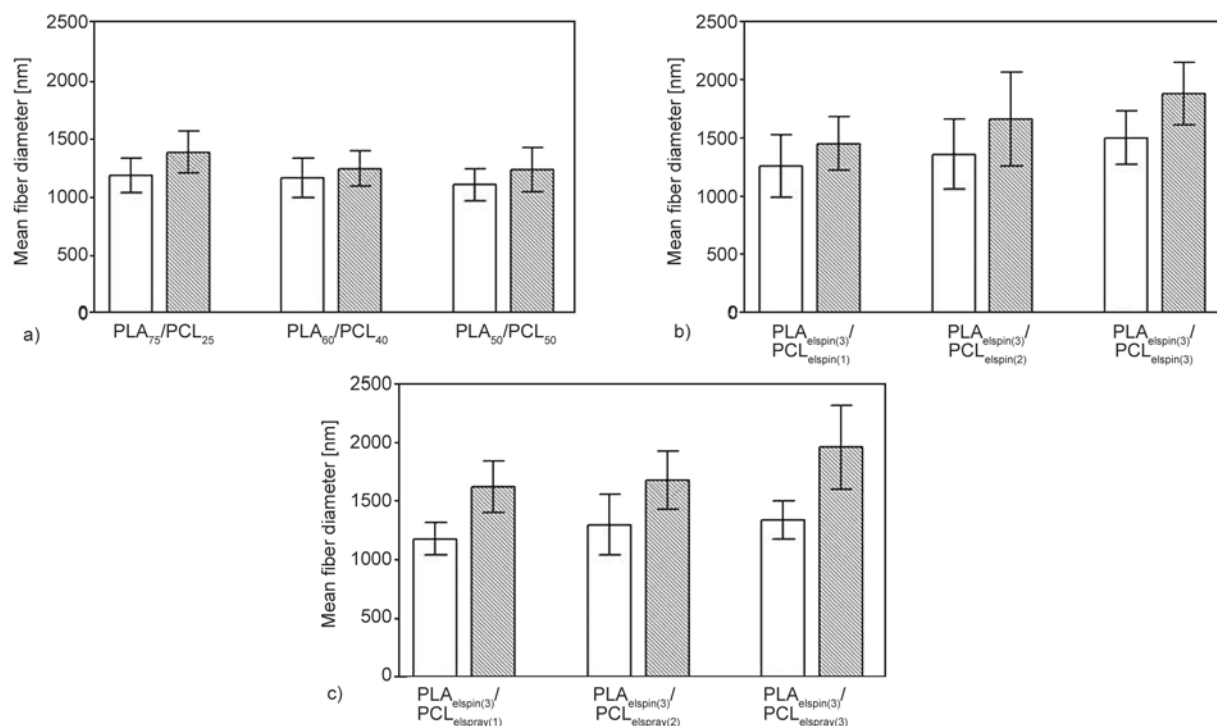


Figure 3. Mean fiber diameters of: PLA/PCL (a), PLA_{elspin}/PCL_{elspin} (b) and PLA_{elspin}/PCL_{elsspray} (c); empty bars – before heating, hatched bars – after heating

before heat treatment did not vary significantly for PLA₇₅/PCL₂₅, PLA₆₀/PCL₄₀ and PLA₅₀/PCL₅₀ fibers and it was ca. 1150 nm, and after heating its value was 1300 nm (Figure 3a). The increase in the mean fiber diameter was attributed to the interconnection of the fibers.

The possibility for preparation of mats with a ‘sandwich’-type design was studied. These novel materials were prepared by alternating electrospinning of a PCL and a PLA solution, terminating by deposition of PLA or PCL fibers on top of the prepared mats. The two ‘sandwich’-type mats are schematically represented in Figure 2. The morphological alterations in the mats after heating indicate that in the case of ‘sandwich’ PCL+PLA the PLA fibers are submerged in the molten PCL fibers. A more interesting phenomenon was observed in the case of ‘sandwich’ PLA+PCL mats, where after melting of PCL fibers a filter-like structure was obtained.

3.1.2. Morphology and topology of fibers prepared by simultaneous electrospinning of two separate solutions

The simultaneous electrospinning of PLA and PCL solutions resulted in the preparation of PLA_{elspin}/PCL_{elspin} mats composed also of defect-free fibers. It was found that with increase in the flow rate of the

PCL solution the average fiber diameter in the mats increased: 1260±270 nm for PLA_{elspin(3)}/PCL_{elspin(1)}, 1360±300 nm for PLA_{elspin(3)}/PCL_{elspin(2)} and 1500±230 nm for PLA_{elspin(3)}/PCL_{elspin(3)}. After heating the diameter of PLA fibers in the PLA_{elspin}/PCL_{elspin} mats was larger than that in PLA mats: 1450±230, 1660±400 and 1880±270 nm for PLA_{elspin(3)}/PCL_{elspin(1)}, PLA_{elspin(3)}/PCL_{elspin(2)} and PLA_{elspin(3)}/PCL_{elspin(3)}, respectively. The larger diameter may be attributed to coating of the PLA fibers with molten PCL. As seen from the SEM micrographs shown in Figure 4, after heating the PLA fibers were thermally sealed through molten PCL. The PLA_{elspin(3)}/PCL_{elspin(3)} fibers were sealed to the greatest extent because in this case the amount of the melting polymer was the highest.

3.1.3. Morphology and topology of fibers fabricated by simultaneous electrospinning and electrospaying of two separate solutions

PLA_{elspin}/PCL_{elsspray} mats have been fabricated by simultaneous electrospinning of a PLA solution and electrospaying of a PCL solution. It is evident from the SEM micrographs of the fibrous materials (Figure 5) that the defect-free and cylindrical PLA fibers are decorated with PCL particles. It was found that

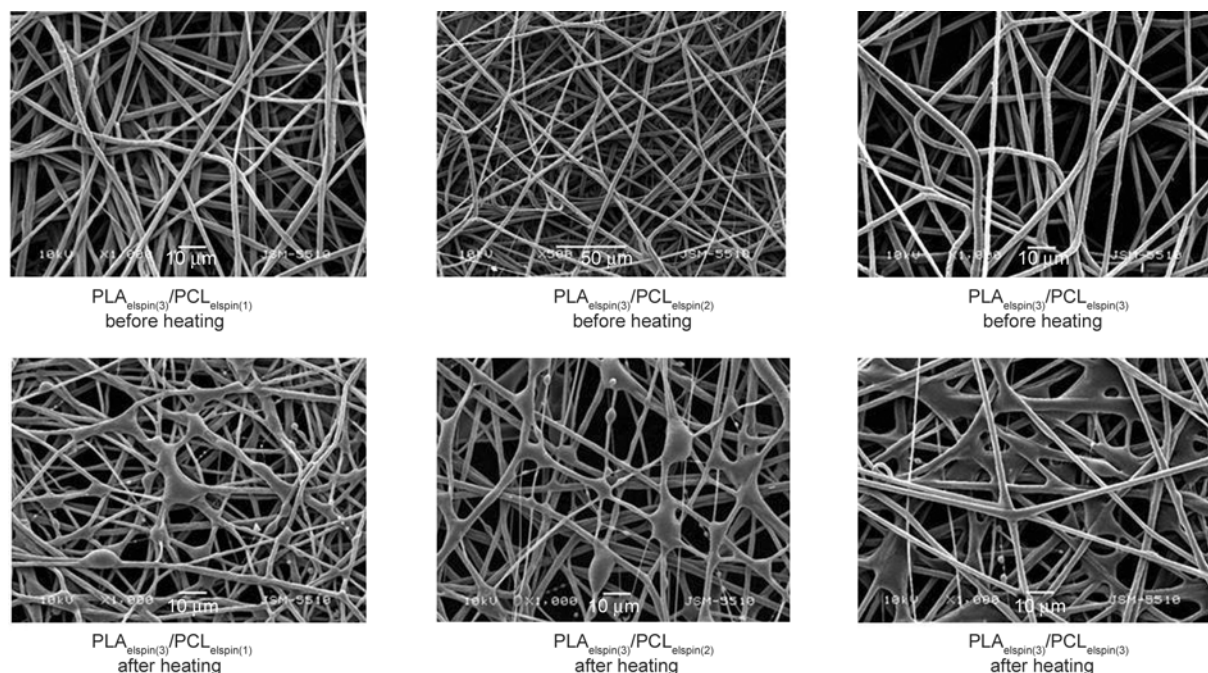


Figure 4. SEM micrographs before and after heating (60°C) of PLA_{elspin}/PCL_{elspin} fibers prepared at various feed rates of the PCL_{elspin} solution – 1, 2, or 3 mL/h; magnification ×1000

with the increase in the feed rate of the PCL solution the mean diameter of the particles increased. It was ca. 900±180, 1150±170 and 1300±170 nm at an electrospinning rate of the solution of 1, 2 and 3 mL/h, respectively.

The heat treatment of the mats led to melting of PCL particles, whereupon the PLA fibers were sealed in the sites where the particles were located.

It was found that with the increase in the feed rate during electrospinning a greater number of particles were deposited on the PLA fibers. This explains why the greatest number of sealed fibers are observed in the case of the PLA_{elspin(3)}/PCL_{elspray(3)} system. The diameter of the PLA fibers in the PLA_{elspin}/PCL_{elspray} mats before heating was close to that of the fibers of a PLA mat – ca. 1250 nm.

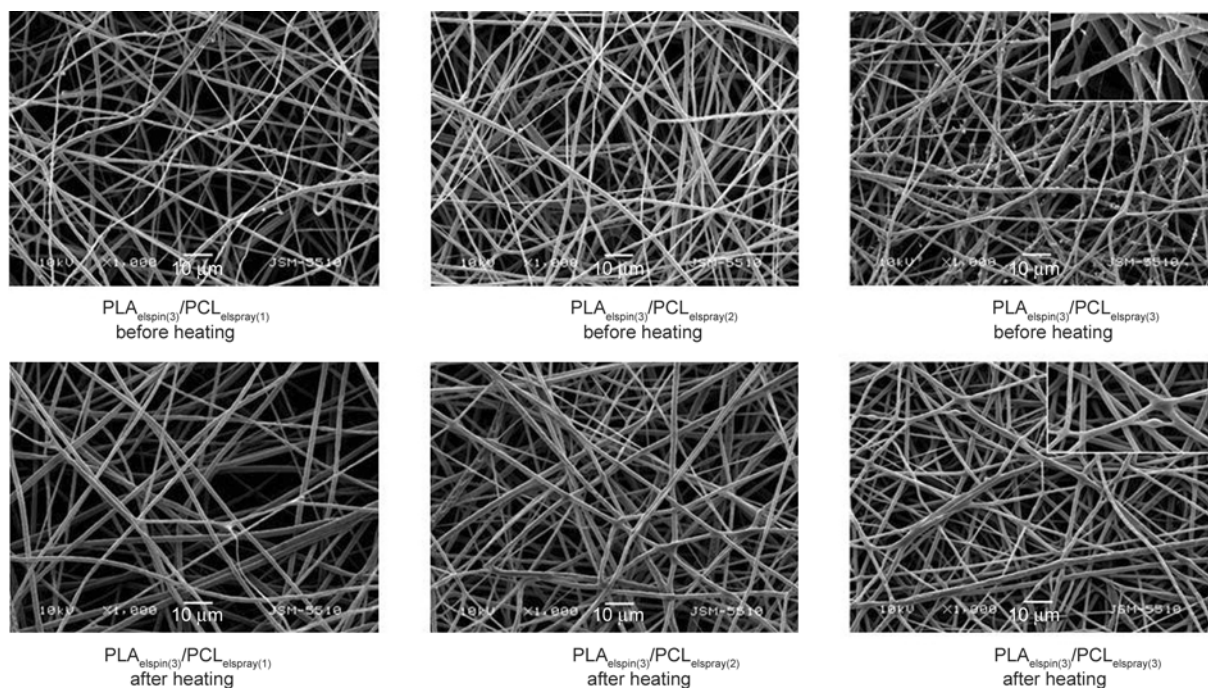


Figure 5. SEM micrographs of PLA_{elspin}/PCL_{elspray} fibers prepared at various feed rates of the PCL_{elspray} solution – 1, 2 and 3 mL/h before and after heat treatment (60°C); magnification ×1000, insets – ×1400

After heating it increased to 1700 nm as a result of coating of the fibers with the molten PCL particles (Figure 3).

The obtained results indicate that after heating the mats at the melting temperature of PCL, only the part of the material which is composed of PCL melts (PLA melting temperature – ca. 165°C). As already discussed and as evident from Figures 2, 4 and 5, after thermal treatment the fibrous structure of the mats is preserved but the PLA fibers are thermally sealed by the molten PCL fibers/particles. A different case is observed when the polymer scaffold is composed of one polymer and after heat treatment the individual fibers do not retain their initial morphology and the material obtains film-like morphology [13, 14]. It is evident from the obtained results that the porous structure of the mats (the voids between the fibers) depends both on the architecture of the fibrous materials and on their thermal treatment. It was found that after heating the porosity of the PLA₅₀/PCL₅₀ mats was reduced as compared to the pristine mats. This finding held true for PLA_{elspin(3)}/PCL_{elspin(3)} fibers, as well, but the tendency was expressed to a smaller extent. In contrast, in the case of PLA_{elspin(3)}/PCL_{elspray(3)} mats the voids between the fibers after melting the PCL particles increased. This indicates that fibrous materials with desired porous structure can be prepared after heating depending both on the mat architecture

(mats composed of fibers only or fibers and particles) and on the PCL content in the pristine material. In the case of all types of mats no shrinking of the fibrous structure was observed after heat treatment. Supplementary information about the distribution of the sites and the manner of sealing of the fibers with the molten PCL fibers/particles was obtained after incorporation of fluorescein (F) in the PCL spinning/spraying solution. The fluorescein-loaded PCL fibers or particles participating in mat formation are further denoted as PCL^F. In Figure 6 micrographs taken of one and the same fragment of the fibrous materials before and after turning a fluorescence light source on are presented. This juxtaposition allowed us to take into account the morphological changes occurring in the the fibrous materials after heating them at 60°C. As seen from Figure 6, the PCL^F fibers before heating were characterized by an intensive fluorescence signal along their length, thus indicating that F was well dispersed in the fibers. After thermal treatment of the PCL^F mat, a layer composed of molten fibers was observed and the fluorescence signal was emitted by the entire material (image not shown). Formation of such a molten fibers layer was observed in the case of ‘sandwich’ type PLA+PCL^F mats after heating, as well (Figure 6). Comparing the images of the PLA_{elspin(3)}/PCL^F_{elspin(3)} and PLA_{elspin(3)}/PCL^F_{elspray(3)} mats (Figure 6) before and after turning a fluorescence

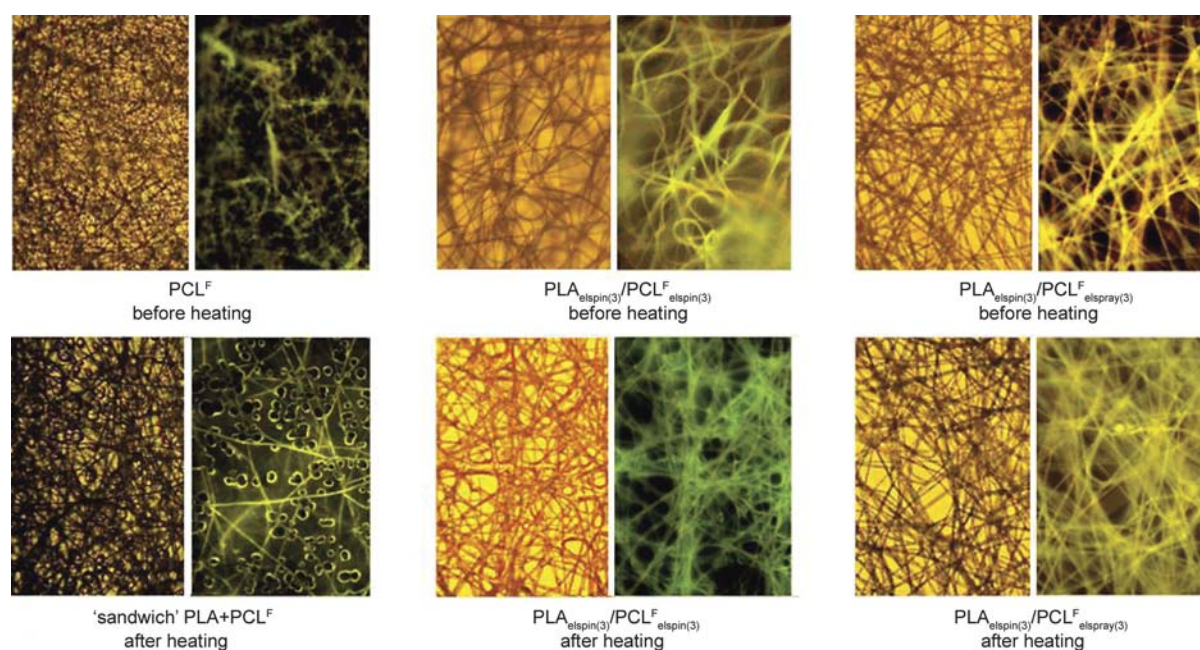


Figure 6. Optical micrographs of one and the same fragment of PCL^F, ‘sandwich’ type PLA+PCL^F mat, PLA_{elspin(3)}/PCL^F_{elspin(3)} and PLA_{elspin(3)}/PCL^F_{elspray(3)} fibrous materials before and after turning a fluorescence light source on; magnification $\times 25$

light source on allowed to distinguish clearly the PLA fibers from the PCL^F fibers/particles. After heat treatment in these mats a change in the distribution of the fluorescence signal, corresponding to sealing of the fibers by means of molten PCL^F fibers/particles (Figure 6) was observed.

3.2. Degree of crystallinity and thermal stability of the mats

The PLA, PCL, PLA₅₀/PCL₅₀, PLA_{elspin(3)}/PCL_{elspin(3)} and PLA_{elspin(3)}/PCL_{elspray(3)} mats were subjected to DSC analysis. It was found that the crystallinity degree of PLA was affected both by the composition and the thermal treatment of the fibrous material (Table 1). For the PLA, PLA₅₀/PCL₅₀ and PLA_{elspin(3)}/PCL_{elspray(3)} mats before heating the crystallinity degree of the polyester was ca. 30%, and for PLA_{elspin(3)}/PCL_{elspin(3)} mats – ca. 20% (Table 1). After heat treatment of the fibrous materials it increased, its values being 43, 22 and 45% for PLA₅₀/PCL₅₀, PLA_{elspin(3)}/PCL_{elspin(3)} and PLA_{elspin(3)}/PCL_{elspray(3)} mats, respectively (Table 1). This result can be explained by the formation of an additional PLA crystalline phase in the fibers after heating the mats. This is evidenced by the absence of a cold crystallization peak in the thermograms of the mats subjected to thermal treatment. The results we have obtained are consistent with the literature data for increase in the crystallinity degree of PLA after thermal treatment [19]. Unlike the case of PLA, the crystallinity degree of PCL was found to decrease after heating the mats, which was observed for the PLA₅₀/PCL₅₀, and PLA_{elspin(3)}/PCL_{elspray(3)} systems (Table 1). In the fibrous materials before or after their heating cold crystallization for PCL was not detected.

The thermal stability of the fibrous materials was estimated by TGA analysis. The thermograms of PLA, PCL, PLA₅₀/PCL₅₀, PLA_{elspin(3)}/PCL_{elspin(3)} and PLA_{elspin(3)}/PCL_{elspray(3)} mats before and after heating are shown in Figure 7 and the degradation temperature (T_d) of PLA and PCL in the mats is presented in the Table 2. As seen, the PLA mats were characterized by a degradation temperature (T_d) of approximately 355°C. PCL fibers before heating degraded at 405°C. The results indicate that the PCL fibers possess greater thermal stability.

It was found that the material obtained from the PCL fibers molten at 60°C degraded at a temperature close to that for a PCL mat – 402°C. Melting of PCL in the PLA₅₀/PCL₅₀ and PLA_{elspin(3)}/PCL_{elspin(3)} mats led to the obtaining of materials with greater thermal stability (as compared to the non-heated mats), which were characterized by 50% weight loss at around 350–360°C. The presence of the particles in PLA_{elspin(3)}/PCL_{elspray(3)} when not preliminarily heat-treated had no impact on the thermal sta-

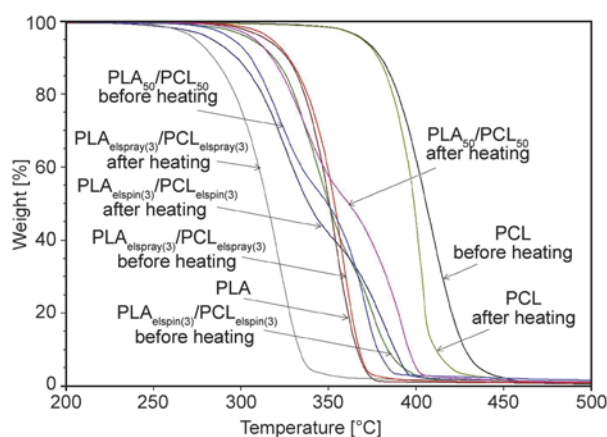


Figure 7. TGA thermograms of PLA, PCL, PLA₅₀/PCL₅₀, PLA_{elspin(3)}/PCL_{elspin(3)}, PLA_{elspin(3)}/PCL_{elspray(3)} fibers before and after heating at 60°C

Table 1. Values of ΔH_{cc}^* , ΔH_m , χ_c for PLA and χ_c for PCL in the PLA, PLA₅₀/PCL₅₀, PLA_{elspin(3)}/PCL_{elspin(3)}, PLA_{elspin(3)}/PCL_{elspray(3)} mats before and after heating them at 60°C

Mat	ΔH_{cc}^{PLA} [J/g]	ΔH_m^{PLA} [J/g]	ΔH_m^{PCL} [J/g]	χ_c^{PLA} [%]	χ_c^{PCL} [%]
PCL before heating			78.7		56.4
PCL after heating			78.1		56.0
PLA	14.9	44.2		31.5	
PLA ₅₀ /PCL ₅₀ before heating	5.0	20.8	41.6	33.9	59.6
PLA ₅₀ /PCL ₅₀ after heating	*	19.9	37.8	42.8	54.3
PLA _{elspin(3)} /PCL _{elspin(3)} before heating	10.1	28.1	18.0	19.4	12.9
PLA _{elspin(3)} /PCL _{elspin(3)} after heating	*	20.6	37.8	22.2	27.1
PLA _{elspin(3)} /PCL _{elspray(3)} before heating	14.0	42.8	0.8	30.9	0.6
PLA _{elspin(3)} /PCL _{elspray(3)} after heating	*	41.7	0.5	44.8	0.4

*no cold crystallization was detected

Table 2. Degradation temperature (T_d) of PLA and PCL in the electrospun fibrous materials

Sample	T_d of PCL [°C]	T_d of PLA [°C]
PCL before heating	405	
PCL after heating	402	
PLA		355
PLA ₅₀ /PCL ₅₀ before heating	372	322
PLA ₅₀ /PCL ₅₀ after heating	392	336
PLA _{elspin(3)} /PCL _{elspin(3)} before heating	375	345
PLA _{elspin(3)} /PCL _{elspin(3)} after heating	383	325
PLA _{elspin(3)} /PCL _{elspray(3)} before heating	*	358
PLA _{elspin(3)} /PCL _{elspray(3)} after heating	*	322

* T_d not observed

bility of the fibrous materials as compared to those composed of PLA, whereas the degradation temperature of the mats after heating was lower (322°C). This result might be attributed to the difference in the concentrations of the starting PCL solutions subjected to electrospinning (0.4 wt%) and electrospinning (9 wt%), thus indicating that the PCL amount in PLA_{elspin(3)}/PCL_{elspray(3)} was not sufficient to improve the thermal stability of this material.

3.3. Water contact angle of the fibrous materials

During recent years an increasing interest has been paid to the development of superhydrophobic self-cleaning surfaces with properties similar to those of the lotus leaves which surface is uniformly covered with micro-sized protrusions and recesses decorated with nano-sized particles of a wax-like material. By combining the biomimetic approaches and modern nanotechnologies such as electrospinning and electrospinning the development of surfaces with specific hydrophobic behavior can be achieved. A 3D architecture with micro- and nanohierarchical arrangement lies in the basis of these properties. In

the present study a relationship was found between the 3D micro- and nanoarchitecture of the mats and their hydrophobic behaviour. The average value of the water contact angle of a PCL mat before heating was ca. 121°, and that of a PLA mat – 125°. These values for a PLA and PCL mat were in conformity with already reported data [20, 21]. The thermal treatment of the PCL fibrous material led to a significant decrease in the water contact angle values – 68° (Figure 8). This result is also consistent with the data obtained from water contact angle studies of a PCL film conducted by other authors [22]. Before heat treatment the contact angle of PLA₅₀/PCL₅₀ and PLA_{elspin(3)}/PCL_{elspin(3)} mats remained close to that of a PCL mat, but after heating it was reduced to 88 and 79° (Figure 8). The PLA_{elspin(3)}/PCL_{elspray(3)} fibrous materials represented some peculiarities. In that case the melting of the PCL particles did not exert any effect on the hydrophobic character of the mats: the contact angle values were ca. 120° after and ca. 124° before heating for a PLA_{elspin(3)}/PCL_{elspray(3)} mat (Figure 8).

It is noteworthy that in the determination of the hydrophobic characteristics of the fibrous materials apart from the polymer nature, a key part is played by the micro- and nanohierarchy in architectural aspect similarly to superhydrophobic structures occurring in nature. For that reason the mats characterized by a higher number of hierarchic levels (fibers – PCL, fibers/fibers – PLA_{elspin}/PCL_{elspin} or fibers/particles – PLA_{elspin}/PCL_{elspray}) before heat treatment showed higher water contact angle values than the materials obtained after heat treatment regardless of the fact that the polymer composition was one and the same (fibers – PCL, partially molten fibers – PLA_{elspin}/PCL_{elspin} or fibers thermally sealed by molten PCL particles – PLA_{elspin}/PCL_{elspray}).

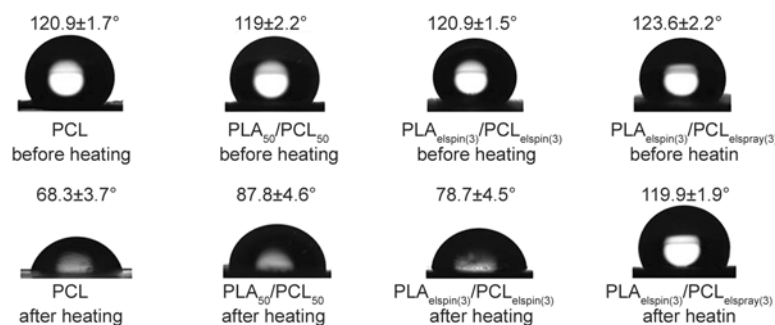


Figure 8. Digital photographs of water droplets deposited onto PCL, PLA₅₀/PCL₅₀, PLA_{elspin(3)}/PCL_{elspin(3)} and PLA_{elspin(3)}/PCL_{elspray(3)} mats before and after heat treatment at 60°. The fibrous materials were cut in the collector rotation direction.

This also accounted for the small difference in the water contact angle of the PLA_{elspin(3)}/PCL_{el spray(3)} mats after heating, where the fibrous structure of the mat was preserved and only thermal sealing of the fibers by melting of PCL particles occurred. This impact of the surface topology of the mats indicates that the hydrophobic characteristics of the fibrous materials can be influenced more easily after heat treatment of the fibrous materials prepared by electrospinning of a common PLA/PCL solution or by simultaneous electrospinning of two separate solutions of PLA and PCL.

On the other hand it was found that the polymer scaffold composition also affects the hydrophobic characteristics of the fibrous materials. The trend for a decrease in the water contact angle value of thermally sealed mats is observed in the case of fibers prepared by electrospinning of a common PLA/PCL solution (Figure 9). It was found that with increase in the PCL content in the fibers the water contact angle values decreased after thermal sealing: 107.5±2.3° for PLA₇₅/PCL₂₅, 91.9±3.3° for PLA₆₀/PCL₄₀ and 87.8±4.6° for PLA₅₀/PCL₅₀ (Figure 9). In this case this was also attributed to the PCL melting part which was accompanied by reduction in the levels of architectural hierarchy. Before the thermal sealing the PLA/PCL materials were hydrophobic and no considerable difference in the water contact angle values of the mats – 120°, was observed (Figure 9).

For the PLA_{elspin}/PCL_{el spin} systems a relationship was found indicating that with the increase in the amount of the deposited PCL fibers (i.e. higher flow rate of the PCL spinning solution) the contact angle values were lower after thermal sealing (113.8±3.6°, 91.3±5.8 and 78.7±4.5° for PLA_{el spin(3)}/PCL_{el spin(1)}, PLA_{el spin(3)}/PCL_{el spin(2)} and PLA_{el spin(3)}/PCL_{el spin(3)}, respectively) compared to those before the thermal

treatment of the mats: 122° (Figure 9). The decrease in the water contact angle values after thermal sealing might be attributed to melting of the PCL fibers. In the case of the ‘sandwich’ type PLA+PCL mats before heat treatment the contact angle acquired values characteristic of PCL – 121°, since these fibers were deposited on the mat surface, and after heating – ca. 94°. ‘Sandwich’ PCL+PLA mats represented a different case where no significant difference in the values of the contact angle before and after heating the mat (125°) was observed. These values were close to those of the PLA fibers and this could be explained by the fact that the PCL fibers are located beneath those of PLA and upon melting they do not affect significantly the topology of the mat surface.

3.4. Mechanical testing of the fibrous materials

The mechanical properties of the fibrous materials obtained by electrospinning depend on a number of parameters, such as: fiber diameter [23], presence of defects (bead-like, spindle-like defects) along the fiber length [24] or on the crystallinity degree of the polymer constituting the fibers [the amorphous phase of the fibers accounts for their elastic properties (elastomeric properties)], and the crystalline phase imparts strength (dimensional stability to the array of molecules) [25]. Some electrospinning conditions, such as the air humidity also have an impact on the mechanical properties of the mats [26]. The architecture of the micro- and nanoscale fibrous materials is of importance, as well: when they are composed of oriented fibers the mat is stronger compared to mats composed of randomly deposited fibers [27, 28]. It is possible to prepare fibrous materials possessing desired strength by varying the weight ratios of the two polymers [29]. Interconnected fibers also improve the mechanical proper-

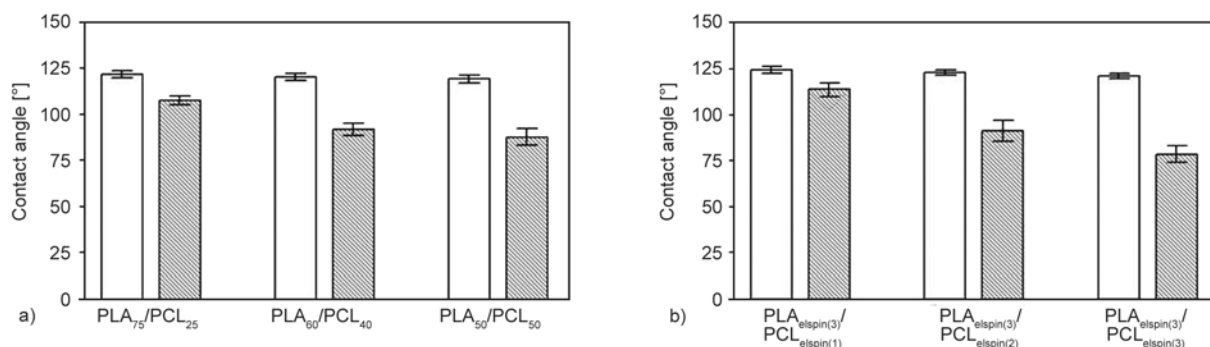


Figure 9. Contact angle values measured upon water droplet deposition onto PLA/PCL (a) and PLA_{el spin}/PCL_{el spin} (b) mats; empty bars – before heating, hatched bars – after heating. The mats were cut in the collector rotation direction.

ties of the fibrous materials [30], which are influenced by the structure of the fibers and the interactions between them, as well [31]. Enhancement of the mechanical parameters (tensile strength, yield stress, and Young's modulus) can be achieved in the presence of finer fibers (a nano-network) among the main fibers [32].

A major problem regarding the mechanical testing of electrospun micro- and nanofibrous materials is the lack of reliable standards for the performance of these tests. An issue of great significance which has been barely discussed in scientific literature is the determination of the mechanical characteristics of micro- and nanofibrous non-woven textile and the direction in which the test specimens should be cut: parallel (0°) or at a definite angle with respect to the collector rotation direction (45° , 90° or others). In the process of cutting the test specimens from the electrospun mats mechanical disruption of the fibers takes place. In the majority of cases the fibers have a tendency to wind around the collector in the direction of its rotation. Depending on the manner in which the fibers are deposited, mats composed of fibers aligned along the collector rotation axis or randomly deposited fibers are prepared. The experiments we have performed have demonstrated that the mats cut in the collector rotation direction (0°) display better mechanical properties compared to those cut at an angle of 90° . Intermediate mechanical properties are manifested by test specimens cut

at an angle of 45° (Figure 10). These results can be explained by the amount of fibers caught by the grips of the tensile testing apparatus. That is why for samples cut in the collector rotation direction it is more probable that a greater number of fibers will be clamped by their both extremities between the grips as compared to samples cut at angle of 45° or 90° . This leads to the manifestation of better mechanical parameters in the case of fibers cut at an angle of 0° as compared to those cut at angle of 45° or 90° .

The possibility for enhancement of the mechanical characteristics of the mats (PLA/PCL, 'sandwich' type (PLA+PCL and PCL+PLA), PLA_{elspin}/PCL_{elspin} and PLA_{elspin}/PCL_{elspray}) by subjecting them to thermal treatment was studied. All mats were cut along the rotational direction of the collector and heated at the melting temperature of PCL (60°C). The purpose was to achieve thermal sealing of the fibers by the molten PCL fibers or particles. The results from the performed mechanical tests of the fibrous materials before and after heating are presented in Figure 11.

3.4.1. Mechanical assays of mats prepared by electrospinning of a single solution or by simultaneous electrospinning of two separate solutions

The determination of the mechanical characteristics of the control samples (before thermal sealing) revealed that PLA fibers had higher values of Young's

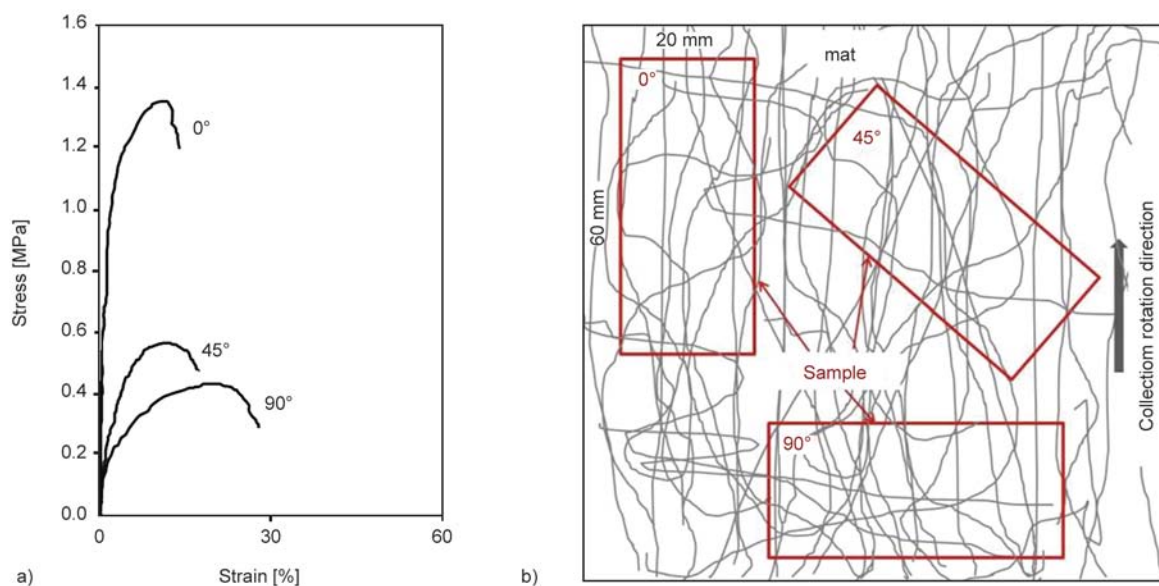


Figure 10. Impact of the direction of cutting of mats (0 , 45 or 90°) with respect to the collector rotation direction on the mechanical behavior of the PLA_{elspin(3)}/PCL_{elspin(3)} mat after heating (a) and schematic representation of the different directions of cutting (b)

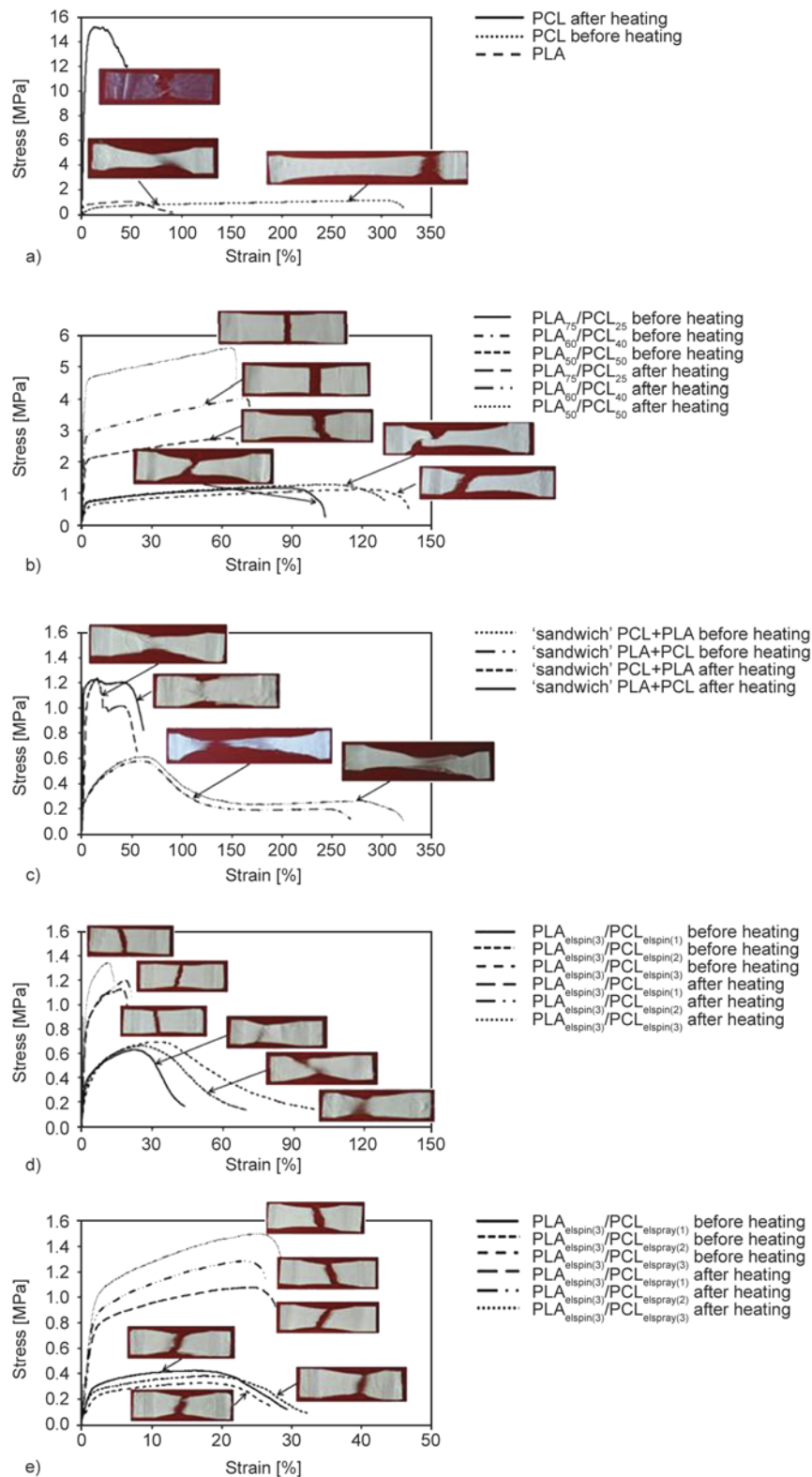


Figure 11. Mechanical stress/strain curves of PLA and PCL mats (a), PLA/PCL (b), ‘sandwich’ type mats (PLA+PCL or PCL+PLA) (c), PLA_{elspin}/PCL_{elspin} mats (d) and PLA_{elspin}/PCL_{elspray} (e) before and after heat treatment

modulus – 46 MPa as compared to PCL fibers – 5 MPa (Figure 11a). It was found that the difference in the strength of the mats exerted an effect on the degree of their deformation before breaking. It was smaller for a PLA mat (100%) as compared to that

for a PCL mat before heat treatment (330%). The ultimate stress values of the two mats prior to heat treatment did not show any significant difference: ca. 0.19 and 0.52 MPa, for PLA and PCL, respectively (Figure 11a). Melting of the PCL fibers at

60°C led to a substantial change in the mechanical behavior of the obtained PCL material. A considerable increase in the strength; Young's modulus values – ca. 330 MPa, and ultimate stress – 12 MPa (Figure 11a) was recorded. The material composed of molten PCL fibers demonstrated poorer plastic properties as compared to the PCL fibrous materials and breaking occurred at a smaller deformation of 50%. This is an indication that melting of the polyester fibers results in the obtaining of PCL material with enhanced mechanical characteristics.

In Figure 11b the results obtained from the tensile tests of PLA/PCL mats before and after thermal sealing are displayed. It is noteworthy that before heat treatment the fibrous materials manifested similar behaviour with regard to the elastic deformations: the value of Young's modulus for all fibers was ca. 30 MPa. It was found that with the increase in the PCL content the materials underwent greater deformation before breaking. It was ca. 98% for PLA₇₅/PCL₂₅, 125% for PLA₆₀/PCL₄₀ and 135% for PLA₅₀/PCL₅₀ (Figure 11b). These results were in accordance with the results obtained from the tensile tests for PLA and PCL mats (before heat treatment), showing that the deformation of PCL before breaking was greater than that of PLA. The ultimate stress of the mats before heat treatment was ca. 0.6 MPa. Heating of the PLA/PCL materials resulting in PCL melting led to the obtaining of more robust fibrous materials. The PLA₅₀/PCL₅₀ mats which were characterized by the highest degree of fiber interconnectivity exhibited the greatest strength (Young's modulus – 325 MPa and ultimate stress – 4.8 MPa, Figure 11b). In contrast to them the PLA₆₀/PCL₄₀ had Young's modulus of ca. 185 MPa and ultimate stress of ca. 3.5 MPa, and the PLA₇₅/PCL₂₅ fibers were the most brittle ones (Young's modulus – 100 MPa and ultimate stress – 2.6 MPa), characterized by the lowest degree of interconnectivity of the fibers (Figure 11b). After thermal treatment breaking of the PLA/PCL mats took place at a smaller deformation degree (70%) as compared to non-heated fibers, and this phenomenon occurred regardless of the PCL content (Figure 11b).

The curve profiles of the 'sandwich' type PLA+PCL and PCL+PLA mats before heat treatment indicated a behavior of the mats characteristic of each of the polymers. In the case of these materials regardless of the mat design (deposition of the layer of PCL fibers beneath or on top of that of PLA fibers) when

tensile tests were performed with the specimens breaking occurred in the PLA fibers first (deformation ca. 100%) followed by breaking of PCL fibers (deformation ca. 300%). These changes in the length of the mats were consistent with the results for the deformational changes in the PLA and PCL fibrous materials before heating (Figure 11c). Young's modulus was ca. 22 MPa and the ultimate stress of the fibrous materials – ca. 0.13 MPa. In this case the thermal sealing of the mats resulted in enhancement of the mechanical properties, as well. When breaking thermally treated mats, first the layer of molten PCL fibers broke, and then followed by breaking of the PLA fibers. As shown in Figure 3, in the case of 'sandwich' type PLA+PCL mats submerging of the PLA fibers in the molten PCL fibers was observed, whereas in the case of the 'sandwich' PCL+PLA mats the PCL molten fibers penetrate in the bulk of the layer of PLA fibers. This new distribution of the polymers in the bulk of the mats after heating exerts an effect on the mechanical behavior of the mats. As evident from Figure 11c, in the course of breaking of 'sandwich' PCL+PLA mats two well defined maxima were observed. The first one corresponded to breaking of the PCL molten fibers (maximum deformation of 20%), and the second one – to breaking of the PLA fibers (50%). The two peaks characteristic of each of the polyesters are less clearly distinguished in the course of the stress/strain curves of the heated 'sandwich' PLA+PCL mats. The values of the deformation at break of the two polymers were close to those recorded after heating of 'sandwich' PCL+PLA mats. After heat treatment the two types of fibrous materials ('sandwich' PLA+PCL and PCL+PLA) were characterized by values of Young's modulus of ca. 68 MPa and ultimate stress of ca. 0.7 MPa.

3.4.2. Mechanical testing of mats prepared by simultaneous electrospinning of two separate solutions

PLA_{elspin}/PCL_{elspin} mats before heat treatment were characterized by values of Young's modulus and ultimate stress, of ca. 15 and 0.10 MPa, respectively (Figure 11d). A relationship was found according to which with the increase in the amount of deposited PCL fibers in the mat (i.e with the increase in the feed rate of the PCL spinning solution), the maximum deformation before breaking of the material increased. The PLA_{elspin(3)}/PCL_{elspin(3)} mats (100%)

underwent the greatest deformation followed by PLA_{elspin(3)}/PCL_{elspin(2)} (70%) and PLA_{elspin(3)}/PCL_{elspin(1)} mats (40%, Figure 11d). After heat treatment the fibrous PLA_{elspin}/PCL_{elspin} materials became stronger and higher values for Young's modulus (50 MPa) and ultimate stress (1.0 MPa, Figure 11d) were recorded. The greater strength of the mats after heat treatment was attributed to thermal sealing of the fibers with the molten PCL fibers. The greatest strength was demonstrated by the PLA_{elspin(3)}/PCL_{elspin(3)} mats which contained the highest PCL content and thus thermal sealing occurred to the highest degree.

3.4.3. Mechanical testing of mats prepared by simultaneous electrospinning and electrospaying of two separate solutions

The results for PLA_{elspin}/PCL_{elspray} fibers indicated that in this case heat treatment led to the obtaining of materials with enhanced strength. That was attributed to thermal sealing of the PLA fibers with the molten PCL particles. It was found that the greatest strength was manifested by PLA_{elspin(3)}/PCL_{elspray(3)} mats where sealing took place to the greatest extent, because the material before heat treatment contained the greatest amount of particles. The values of Young's modulus (38 MPa) and the ultimate stress (1.00 MPa) for the mats after heat treatment were twice as high as the values obtained for these parameters prior to heat treatment of the mats – ca. 17 MPa for Young's modulus and 0.13 MPa – for the ultimate stress (Figure 11d). Another characteristic feature of the PLA_{elspin}/PCL_{elspray} materials was breaking at one and the same degree of deformation – 30% before and after heat treatment (Figure 11d).

To summarize, in the present study we used two biodegradable and biocompatible polymers with different thermal behavior: PLA with melting temperature of 165°C and PCL with lower melting temperature ($T_m = 60^\circ\text{C}$). The thermal treatment of the mats at the T_m of PCL led to improvement of their mechanical properties. The heating of the PLA/PCL, PLA_{elspin}/PCL_{elspin} and PLA_{elspin}/PCL_{elspray} mats, at the T_m of PCL, allowed us to obtain fibrous materials of interconnected fibers (PLA/PCL mats) or PLA fibers thermally sealed by molten PCL fibers or particles (PLA_{elspin}/PCL_{elspin}, PLA_{elspin}/PCL_{elspray}). In the case of the 'sandwich'-type mats we observed PLA fibers submerged in molten PCL fibers ('sand-

wich' PCL+PLA after heating) or filter-like structure ('sandwich' PLA+PCL after heating). This morphological change of the fibrous materials was the primary cause of their mechanical properties improvement. The most durable heat treated fibrous materials were obtained in the case of the PLA/PCL mats produced by electrospinning of a single solution. The obtained results indicate that depending on the architecture of the fibrous materials after heat treatment mats with various degrees of sealing of the fibers, with enhanced strength and deformability before breaking can be fabricated.

4. Conclusions

In the present study new fibrous materials of various composition and architecture were prepared from PLA and PCL using electrospinning and electrospaying. Mats were obtained by electrospinning of a common solution, or using two separate solutions for concurrent electrospinning, or for layer-by-layer deposition on the collector, as well as for using electrospinning in conjunction with electrospaying. Thermal treatment at the melting temperature of PCL enabled the sealing of the fibers thus enhancing the mechanical properties of the mats. The fibrous materials are of interest for a variety of applications such as drug delivery systems, tissue engineering scaffolds, wound dressings or filter membranes.

Acknowledgements

AT thanks Prof. Ph. Dubois (University of Mons – UMONS, Belgium) for providing the possibility to perform internship at the Laboratory of Polymeric and Composite Materials and Dr. R. Mincheva for assistance in performing mechanical tests – carried out during the internship. The internship of AT is financially supported by the POLINNOVA project FP7-REGPOT-2012-2013-1, Grant 316086.

References

- [1] Bhardwaj N., Kundu S. C.: Electrospinning: A fascinating fiber fabrication technique. *Biotechnology Advances*, **28**, 325–347 (2010). DOI: [10.1016/j.biotechadv.2010.01.004](https://doi.org/10.1016/j.biotechadv.2010.01.004)
- [2] Ignatova M., Manolova N., Rashkov I.: Electrospun antibacterial chitosan-based fibers. *Macromolecular Bioscience*, **13**, 860–872 (2013). DOI: [10.1002/mabi.201300058](https://doi.org/10.1002/mabi.201300058)
- [3] Ignatova M., Rashkov I., Manolova N.: Drug-loaded electrospun materials in wound-dressing applications and in local cancer treatment. *Expert Opinion on Drug Delivery*, **10**, 469–483 (2013). DOI: [10.1517/17425247.2013.758103](https://doi.org/10.1517/17425247.2013.758103)

- [4] Toncheva A., Spasova M., Paneva D., Manolova N., Rashkov I.: Polylactide (PLA)-based electrospun fibrous materials containing ionic drugs as wound dressing materials: A review. *International Journal of Polymeric Materials and Polymeric Biomaterials*, **63**, 657–671 (2014).
DOI: [10.1080/00914037.2013.854240](https://doi.org/10.1080/00914037.2013.854240)
- [5] Stoilova O., Manolova N., Gabrovska K., Marinov I., Godjevargova T., Mita D. G., Rashkov I.: Electrospun polyacrylonitrile nanofibrous membranes tailored for acetylcholinesterase immobilization. *Journal of Bioactive and Compatible Polymers*, **25**, 40–57 (2010).
DOI: [10.1177/0883911509353680](https://doi.org/10.1177/0883911509353680)
- [6] Mincheva R., Stoilova O., Penchev H., Ruskov T., Spirov I., Manolova N., Rashkov I.: Synthesis of polymer-stabilized magnetic nanoparticles and fabrication of nanocomposite fibers thereof using electrospinning. *European Polymer Journal*, **44**, 615–627 (2008).
DOI: [10.1016/j.eurpolymj.2007.11.001](https://doi.org/10.1016/j.eurpolymj.2007.11.001)
- [7] Jaworek A., Sobczyk A. T.: Electro spraying route to nanotechnology: An overview. *Journal of Electrostatics*, **66**, 197–219 (2008).
DOI: [10.1016/j.elstat.2007.10.001](https://doi.org/10.1016/j.elstat.2007.10.001)
- [8] Bock N., Woodruff M. A., Huttmacher D. W., Dargaville T. R.: Electro spraying, a reproducible method for production of polymeric microspheres for biomedical applications. *Polymers*, **3**, 131–149 (2011).
DOI: [10.3390/polym3010131](https://doi.org/10.3390/polym3010131)
- [9] Bock N., Dargaville T. R., Woodruff M. A.: Electro spraying of polymers with therapeutic molecules: State of the art. *Progress in Polymer Science*, **37**, 1510–1551 (2012).
DOI: [10.1016/j.progpolymsci.2012.03.002](https://doi.org/10.1016/j.progpolymsci.2012.03.002)
- [10] Korina E., Stoilova O., Manolova N., Rashkov I.: Multifunctional hybrid materials from poly(3-hydroxybutyrate), TiO₂ nanoparticles, and chitosan oligomers by combining electrospinning/electro spraying and impregnation. *Macromolecular Bioscience*, **13**, 707–716 (2013).
DOI: [10.1002/mabi.201200410](https://doi.org/10.1002/mabi.201200410)
- [11] Korina E., Stoilova O., Manolova N., Rashkov I.: Poly(3-hydroxybutyrate)-based hybrid materials with photocatalytic and magnetic properties prepared by electrospinning and electro spraying. *Journal of Materials Science*, **49**, 2144–2153 (2014).
DOI: [10.1007/s10853-013-7907-3](https://doi.org/10.1007/s10853-013-7907-3)
- [12] Zhang L., Liu L-G., Pan F-L., Wang D-F., Pan Z-J.: Effects of heat treatment on the morphology and performance of PSU electrospun nanofibrous membrane. *Journal of Engineered Fibers and Fabrics*, **7**, 7–16 (2012).
- [13] You Y., Lee S. W., Lee S. J., Park W. H.: Thermal inter-fiber bonding of electrospun poly(L-lactic acid) nanofibers. *Materials Letters*, **60**, 1331–1333 (2006).
DOI: [10.1016/j.matlet.2005.11.022](https://doi.org/10.1016/j.matlet.2005.11.022)
- [14] Ramaswamy S., Clarke L. I., Gorga R. E.: Morphological, mechanical, and electrical properties as a function of thermal bonding in electrospun nanocomposites. *Polymer*, **52**, 3183–3189 (2011).
DOI: [10.1016/j.polymer.2011.05.023](https://doi.org/10.1016/j.polymer.2011.05.023)
- [15] Lee S. J., Oh S. H., Liu J., Soker S., Atala A., Yoo J. J.: The use of thermal treatments to enhance the mechanical properties of electrospun poly(ϵ -caprolactone) scaffolds. *Biomaterials*, **29**, 1422–1430 (2008).
DOI: [10.1016/j.biomaterials.2007.11.024](https://doi.org/10.1016/j.biomaterials.2007.11.024)
- [16] Spasova M., Mincheva R., Paneva D., Manolova N., Rashkov I.: Perspectives on: Criteria for complex evaluation of the morphology and alignment of electrospun polymer nanofibers. *Journal of Bioactive and Compatible Polymers*, **21**, 465–479 (2006).
DOI: [10.1177/0883911506068495](https://doi.org/10.1177/0883911506068495)
- [17] Henton D. E., Gruber P., Lunt J., Randall J.: Polylactic acid technology. in ‘Natural fibers, biopolymers, and biocomposites’ (eds.: Mohanty A. K., Misra M., Drzal L. T.) Taylor and Francis, Boca Raton, 527–578 (2005).
- [18] Skoglund P., Fransson A.: Continuous cooling and isothermal crystallization of polycaprolactone. *Journal of Applied Polymer Science*, **61**, 2455–2465 (1996).
DOI: [10.1002/\(SICI\)1097-4628\(19960926\)61:13<2455::AID-APP25>3.0.CO;2-1](https://doi.org/10.1002/(SICI)1097-4628(19960926)61:13<2455::AID-APP25>3.0.CO;2-1)
- [19] Smyth M., Poursorkhabi V., Mohanty A. K., Gregori S., Misra M.: Electrospinning highly oriented and crystalline poly(lactic acid) fiber mats. *Journal of Materials Science*, **49**, 2430–2441 (2014).
DOI: [10.1007/s10853-013-7899-z](https://doi.org/10.1007/s10853-013-7899-z)
- [20] Toncheva A., Paneva D., Manolova N., Rashkov I.: Electrospun poly(L-lactide) membranes containing a single drug or multiple drug system for antimicrobial wound dressings. *Macromolecular Research*, **19**, 1310–1319 (2011).
DOI: [10.1007/s13233-011-1206-0](https://doi.org/10.1007/s13233-011-1206-0)
- [21] Paneva D., Manolova N., Argirova M., Rashkov I.: Antibacterial electrospun poly(ϵ -caprolactone)/ascorbyl palmitate nanofibrous materials. *International Journal of Pharmaceutics*, **416**, 346–355 (2011).
DOI: [10.1016/j.ijpharm.2011.06.032](https://doi.org/10.1016/j.ijpharm.2011.06.032)
- [22] Yan D., Jones J., Yuan X., Xu X., Sheng J., Lee J. C-M., Ma G., Yu Q.: Plasma treatment of random and aligned electrospun PCL nanofibers. *Journal of Medical and Biological Engineering*, **33**, 171–178 (2013).
DOI: [10.5405/jmbe.1072](https://doi.org/10.5405/jmbe.1072)
- [23] Chen Z., Wei B., Mo X., Lim C. T., Ramakrishna S., Cui F.: Mechanical properties of electrospun collagen–chitosan complex single fibers and membrane. *Materials Science and Engineering: C*, **29**, 2428–2435 (2009).
DOI: [10.1016/j.msec.2009.07.006](https://doi.org/10.1016/j.msec.2009.07.006)
- [24] Huang Z-M., Zhang Y. Z., Ramakrishna S., Lim C. T.: Electrospinning and mechanical characterization of gelatin nanofibers. *Polymer*, **45**, 5361–5368, (2004).
DOI: [10.1016/j.polymer.2004.04.005](https://doi.org/10.1016/j.polymer.2004.04.005)

- [25] Wong S-C., Baji A., Leng S.: Effect of fiber diameter on tensile properties of electrospun poly(ϵ -caprolactone). *Polymer*, **49**, 4713–4722 (2008).
DOI: [10.1016/j.polymer.2008.08.022](https://doi.org/10.1016/j.polymer.2008.08.022)
- [26] Pelipenko J., Kristl J., Janković B., Baumgartner S., Kocbek P.: The impact of relative humidity during electrospinning on the morphology and mechanical properties of nanofibers. *International Journal of Pharmaceutics*, **456**, 125–134 (2013).
DOI: [10.1016/j.ijpharm.2013.07.078](https://doi.org/10.1016/j.ijpharm.2013.07.078)
- [27] Lee J., Deng Y.: Increased mechanical properties of aligned and isotropic electrospun PVA nanofiber webs by cellulose nanowhisker reinforcement. *Macromolecular Research*, **20**, 76–83 (2012).
DOI: [10.1007/s13233-012-0008-3](https://doi.org/10.1007/s13233-012-0008-3)
- [28] Chen F., Su Y., Mo X., He C., Wang H., Ikada Y.: Biocompatibility, alignment degree and mechanical properties of an electrospun chitosan–P(LLA-CL) fibrous scaffold. *Journal of Biomaterials Science, Polymer Edition*, **20**, 2117–2128 (2009).
DOI: [10.1163/156856208X400492](https://doi.org/10.1163/156856208X400492)
- [29] Bianco A., Calderone M., Cacciotti I.: Electrospun PHBV/PEO co-solution blends: Microstructure, thermal and mechanical properties. *Materials Science and Engineering: C*, **33**, 1067–1077 (2013).
DOI: [10.1016/j.msec.2012.11.030](https://doi.org/10.1016/j.msec.2012.11.030)
- [30] Newton D., Mahajan R., Ayres C., Bowman J. R., Bowlin G. L., Simpson D. G.: Regulation of material properties in electrospun scaffolds: Role of cross-linking and fiber tertiary structure. *Acta Biomaterialia*, **5**, 518–529 (2009).
DOI: [10.1016/j.actbio.2008.06.016](https://doi.org/10.1016/j.actbio.2008.06.016)
- [31] Cha D. I., Kim K. W., Chu G. H., Kim H. Y., Lee K. H., Bhattarai N.: Mechanical behaviors and characterization of electrospun polysulfone/polyurethane blend nonwovens. *Macromolecular Research*, **14**, 331–337 (2006).
DOI: [10.1007/BF03219090](https://doi.org/10.1007/BF03219090)
- [32] Zhou C., Chu R., Wu R., Wu Q.: Electrospun polyethylene oxide/cellulose nanocrystal composite nanofibrous mats with homogeneous and heterogeneous microstructures. *Biomacromolecules*, **12**, 2617–2625 (2011).
DOI: [10.1021/bm200401p](https://doi.org/10.1021/bm200401p)

Effect of carbon black on electrical and rheological properties of graphite nanoplatelets/poly(ethylene-butyl acrylate) composites

H. Oxfall^{1,2*}, G. Ariu^{1,3}, T. Gkourmpis⁴, R. W. Rychwalski¹, M. Rigdahl¹

¹Department of Materials and Manufacturing Technology, Chalmers University of Technology, SE-412 96 Gothenburg, Sweden

²Swerea IVF AB, SE-431 22 Mölndal, Sweden

³Department of Materials Engineering and Industrial Technologies, University of Trento, I-38050 Trento, Italy

⁴Borealis AB, Innovation & Technology, SE-444 86 Stenungsund, Sweden

Received 27 May 2014; accepted in revised form 10 August 2014

Abstract. The effect of adding carbon black on the electrical and rheological properties of graphite nanoplatelets/poly(ethylene-butyl acrylate) copolymer composites produced via melt or solution mixing was studied. By adding a small amount of low- or high-structured carbon black to the nanocomposite, the electrical percolation threshold decreased and the final conductivity (at higher filler contents) increased. The effect on the percolation threshold was significantly stronger in case of the high-structured carbon black where replacing 10 wt% of the total filler content with carbon black instead of graphite nanoplatelets reduced the electrical percolation threshold from 6.9 to 4.6 vol%. Finally, the solution mixing process was found to be more efficient leading to a lower percolation threshold. For the composites containing high-structured carbon black, graphite nanoplatelets and their hybrids there was a quite reasonable correlation between the electrical and rheological percolation thresholds.

Keywords: nanocomposites, hybrid composites, electrical properties, rheology, melt mixing

1. Introduction

Polymer nanocomposites combine the properties of the polymeric matrix with those of the filler. Traditionally carbon black (CB) has been the filler of choice due to the simplicity of its preparation methods that lead to low prices coupled with good overall performance [1]. The introduction of carbonaceous fillers into the polymer matrix can lead to electrical conductivity, whose level is tightly dependent on the type of filler and polymer used. Depending on the filler and the conductivity level required a large array of materials suited for electrochemical devices and other applications (e.g. fuel cells, batteries, supercapacitors, power cable shielding, auto-

motive boards, chemical vapor sensors, pipe applications etc.) can be designed [2, 3]. The conductivity level required for industrial applications varies, but can be quite high leading to an increase of the overall viscosity, thus leading to processing and performance problems [4].

High aspect ratio fillers based on carbon allotropes like graphene and carbon nanotubes (CNT) offer distinct advantages in comparison with more traditional fillers like carbon black mainly originating from their sheer size [5]. Ever since the first observations of graphene in 2004 [6], graphene-containing polymer nanocomposites have triggered a significant interest. A large number of research groups

*Corresponding author, e-mail: henrik.oxfall@gmail.com

have published a variety of results indicating superior electrical and thermal conductivity, mechanical and rheological properties, gas barrier properties and crystallization behavior of nanocomposites based on high aspect ratio carbon allotropes [5, 7–9].

Hybrid composites of mixtures between different carbonaceous fillers have been seen to exhibit synergistic effects. Fan *et al.* [10] noted a decrease of the percolation threshold and a higher electrical conductivity by combining CB with graphite nanoplatelets (GNP). Similar positive effects have been observed in carbon nanotube (CNT)/graphite nanoplatelet hybrids [11–13] and CNT/GNP/CB hybrids [14]. Furthermore, by combining CNT with CB or GNP the viscosity of the composite melt has been reported to decrease in comparison to single filler composite melt at the same filler loading [15]. This effect was observed already at a content of 1 wt% CNT.

Published results on GNP-CB hybrids are often based on thermosetting polymer systems and high-structured carbon black. With the term high-structured CB we are referring to systems made by fusion of the primary particles into an extended three dimensional structure. The overall dimensions and density of this structure (it can be chain or cluster-like) depend on the preparation method of the CB [16]. There is a need to further explore possible synergistic effects of these hybrids in thermoplastic polymers and study the effect of the CB structure. In the present work, the effects of adding low- and high-structured carbon black, on electrical and rheological properties of a composite based on GNP/poly(ethylene-butyl acrylate) copolymer (EBA) are reported. Different mixing methods are employed with the solvent processing route used as reference. Electrical conductivity and rheological properties were measured along with characterization of the composites using differential scanning calorimetry (DSC) and scanning electron microscopy (SEM). Hybridization of carbon fillers is particularly applicable to extruded materials, where nanoplatelets tend to orient, leading to a need to create conductive paths/bridges between the different filler particles as to maintain the integrity of the conductive network. Due to this fact and since extrusion is a major processing technique, the electrical conductivity measurements and the SEM studies were performed on extruded specimens.

2. Experimental

2.1. Materials

The polymer used was a poly(ethylene-butyl acrylate) random copolymer (EBA) with 17 wt% butyl acrylate (BA), MFR of 7 g/10 min at 190°C and a density of 0.925 g/cm³ (Borealis AB, Sweden).

A high-structured carbon black (HS-CB), Ketjenblack EC 600JD (AKZO Nobel, the Netherlands), with an aggregate size of 10–50 nm, density 1.8 g/cm³, BET surface area 1250 m²/g, according to the supplier, was used. Also a low-structured furnace carbon black (LS-CB) with a surface area of 100–200 m²/g and a density of 1.8 g/cm³ was used. The graphite nanoplatelets (GNP) used were xGnP M5 (XG Sciences, USA), with a thickness of 6–8 nm, diameter of 5 μm, density of 2.2 g/cm³ and surface area of 120–150 m²/g, as given by the manufacturer.

2.2. Compounding

A series of composites containing pure fillers and hybrids in which GNPs were combined with CB (both low- and high-structured) were manufactured. The hybrid compositions used were 90-10, 80-20 and 70-30 for the high-structured CB and 80-20, 70-30 and 60-40 for the low-structured CB. The first number in the hybrid composition denotes the wt% of GNP of the total filler content and the second the wt% of CB. The filler contents used were in the range of 0.5-6.5 volume-% (vol%) for the HS-CB system, 5–14 vol% for the GNP systems, 2–9 vol% for the HS-CB/GNP hybrids and 6–18 vol% for the LS-CB materials and its hybrids.

A Brabender mixing chamber, with a volume of 50 cm³, was used to compound the composites. The mixing was performed at 180°C at 100 rpm for 10 minutes.

Xylene (AnalaR Normapur, VWR Prolabo) was used in a solvent mixing technique. EBA and xylene, 1:15 weight concentration, were stirred at 120°C until the polymer was completely dissolved after 2 hours. GNP and xylene, 1:50 weight concentration, were first stirred at room temperature for 15 minutes, and then sonicated for 4 h in a Branson 1510 E-MTH bath (70 W), Branson Ultrasonic. Every 30 minutes the sonication was shortly stopped and the mixture was stirred for 1 minute. After sonication, the GNP-xylene mixture was heated and added to the EBA-xylene mixture and stirred for an additional 30 min-

utes. After the stirring, the solution was poured into wide bowls in order to evaporate the solvent overnight followed by a final drying in a vacuum oven at 70°C for 12 h. This mixing technique was only used for the high structured CB hybrids and the pure GNP at a filler content of 10 wt%.

2.3. Scanning electron microscopy (SEM)

Scanning electron micrographs were obtained using a low vacuum JSM-6610 LV from Jeol, Japan, with an acceleration voltage of 8 kV and a JSM-7800F from Jeol with an acceleration voltage of 3 kV. The specimens, taken from extruded strings, were ion polished, perpendicular to the flow direction, with a broad ion beam (Gatan Iliant model 693, USA) at 4 kV at –60°C, in order to obtain a smooth surface for SEM studies.

2.4. Differential scanning calorimetry (DSC)

For the DSC measurements, a TG-DTA/DSC STA 449 F1 Jupiter, Netzsch-Gerätebau GmbH, Germany, equipped with a thermocouple Type K, was used. The melting behavior was recorded during heating from 30–200°C under argon atmosphere at a heating rate of 10°C/min. Specimens were taken from extruded strings, similar to the ones used for the electrical measurements.

2.5. Electrical measurements

Electrical measurements were performed using the two-point technique [17]. The specimens were extruded in a capillary rheometer, Ceast Rheoscope 1000 6742/00, Ceast SpA, Pianezza, Italy, using a die with a length/diameter (L/D) ratio of 10/1 [mm/mm] at 170°C. A low piston speed, 2 mm/min, corresponding to a shear rate of 24.3 s⁻¹, as well as a higher piston speed, 20 mm/min (243 s⁻¹) were used, but only two of the systems were subjected to the higher shear rate. The extrudates were then cryo-fractured in liquid nitrogen to a length, l , of 2.5 cm and the fracture surfaces were painted with conductive silver paint. A voltage was applied over the length of the extrudate and the current was measured with a Fluke 8846A Digital multimeter and the resistance, R , was evaluated. The diameter of the extrudates were measured using a digital caliper and the cross section area, A , was calculated. The electrical conductivity, σ , could then be obtained from Equation (1):

$$\sigma = \frac{A}{Rl} \quad (1)$$

Three different voltage levels were used; 10 V for materials with a conductivity higher than 10⁻³ S/cm, 100 V for materials with a conductivity between 10⁻⁵ and 10⁻³ S/cm and 300 V for conductivities lower than 10⁻⁵ S/cm. For each system, ten specimens were employed, and the average values are reported. The standard deviation was below 20% for materials with conductivities higher than 10⁻³ S/cm and it then increased with decreasing conductivity. Since a two-point method was used one cannot fully exclude the existence of surface currents. This could to some extent affect the measured conductivity.

2.6. Rheological measurements

A stress-controlled rotational rheometer, Rheometrics SR200, was used at 180°C under N₂ atmosphere for evaluating the viscoelastic properties of the materials. A parallel plate fixture was employed into which compression molded discs, produced in Bucher press in a frame-like mold at 180°C and a total melting time of 10 minutes, with a diameter of 25 mm and a thickness of 2 mm were inserted. All measurements started with a dynamic time sweep conducted at 0.5 Hz using a low stress until stabilization of the storage modulus G' was attained, as suggested by Kim and Macosko [18, 19]. Dynamic stress sweeps were conducted in order to determine the limit of the linear viscoelastic region and dynamic frequency sweeps were then performed well below this limit from 10 Hz down to 0.002 Hz. For each system two or three measurements were performed and the average values are reported.

3. Results and discussion

3.1. Scanning electron micrographs

Figures 1, 2 and 3 show scanning electron micrographs of the extruded 80-20 hybrid based on GNP and HS-CB at a filler content 5.6 vol%. The micrographs were taken close to the surface of the extrudate. In Figure 1 it can be seen that needle-like GNP stacks were oriented in the flow direction and parallel to the surface of the extrudate. The existence of large needle-like agglomerates indicates poor mixing and that the effective surface area of the filler was decreased compared to the initial surface area. At a higher magnification, Figure 2, it is

evident that large agglomerates consist of thinner GNP platelets while thinner platelets with a thickness smaller than 50 nm were present in the material. At even higher magnification, Figure 3, platelets with a thickness smaller than 20 nm can be observed. Also in Figures 2 and 3, HS-CB particles can be

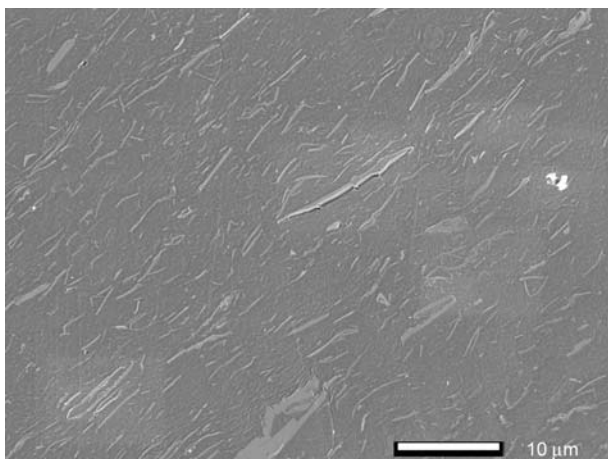


Figure 1. Scanning electron micrograph of the 80-20 GNP HS-CB hybrid at a magnification of 2000×

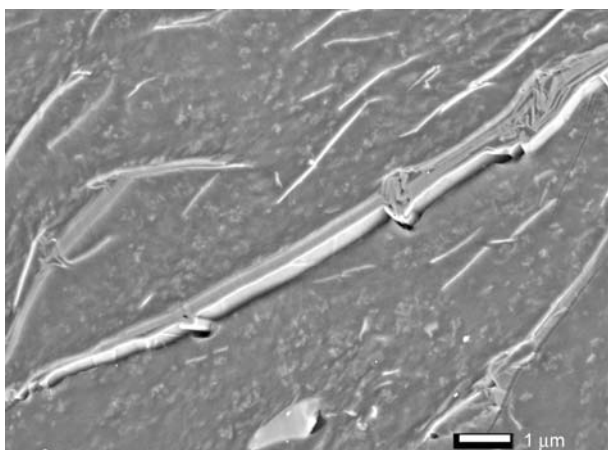


Figure 2. Scanning electron micrograph of the 80-20 GNP HS-CB hybrid at a magnification of 10 000×

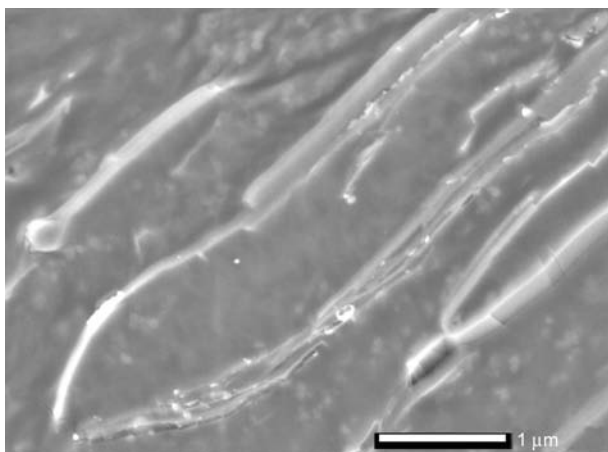


Figure 3. Scanning electron micrograph of the 80-20 GNP HS-CB hybrid at a magnification of 25 000×

observed between the GNP-stacks homogeneously dispersed in the matrix. It is expected that the well dispersed CB particles could provide a physical bridge between the GNP stacks.

An identical orientation effect was observed also in the pure extruded GNP composite, both melt and solvent mixed. No clear differences could be observed with regard to the agglomerate size between the different mixing methods. In the HS-CB composite a good level of dispersion was noted with only few smaller agglomerates present.

3.2. Thermal analysis

The DSC measurements did not indicate clear differences in the crystallinity of the composites as compared to the pure polymer. There was a slight tendency towards higher crystallinity for the materials containing GNP and a slightly lower crystallinity for the materials containing CB compared to the unfilled EBA. A slightly narrower melting endotherm for the composite materials, especially the GNP composites, was observed and indicates that the crystals were thinner than in the unfilled EBA, see Figure 4. This can be attributed to the spatial arrangement of the filler particles that limit the possibility of polymer crystallization, as a number of nucleating sites become available for crystallization initiation. The existence of these different nucleation sites has been reported to lead to a decrease in crystallization rate [20, 21] The reason for such behavior has been attributed to the two-dimensional nature of the GNP platelets that makes lattice matching the dominant force in the crystallization process. The polymer chains need to be absorbed on the graphitic surface and this will force them to undergo conformational changes that subsequently lead to longer crystal-

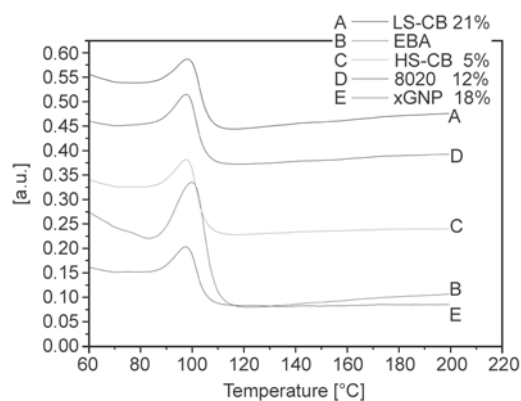


Figure 4. DSC thermograms for nanocomposites and matrix material

lization times. Furthermore, due to the flat surface available for crystallization the polymer crystals can grow at multiple points and with multiple orientations. It has been speculated that the growth of adjacent crystals under these conditions might cause interference between them, leading to the overall suppression of the crystallization kinetics [21]. A similar behavior has been observed with GNP in polypropylene by Kalaitizidou *et al.* [22].

3.3. Electrical conductivity

Figure 5 shows the electrical conductivity as a function of the filler volume fraction for the GNP, the high-structured CB and its hybrids. The onset of electrical conductivity for the CB system was found to be the lowest, just below 2.1 vol%, and the ‘pure’ GNP composite had the highest percolation threshold, just below 6.9 vol%. The conductivity corresponding to the plateau value approached at higher filler contents was several orders of magnitude higher for the CB composites than for those containing GNP. In the work of Strååt *et al.* [23] the same kind of CB was mixed with both polypropylene (PP) and high density polyethylene (HDPE) and despite the fact that both processing and electrical measurements were conducted in a similar manner as in the present work, they report a lower percolation threshold for both polymer systems, being of the order 1 vol%. The percolation threshold of 6.9 vol% (15 wt%) found in this work for the pure melt mixed GNP composite is rather low compared to published results. Polyolefins containing GNP have usually a rather high percolation threshold, e. g. between 12 and 15 wt% in linear low density polyethylene and 14–16 wt% in an ethylene-vinyl acetate copolymer, both prepared by

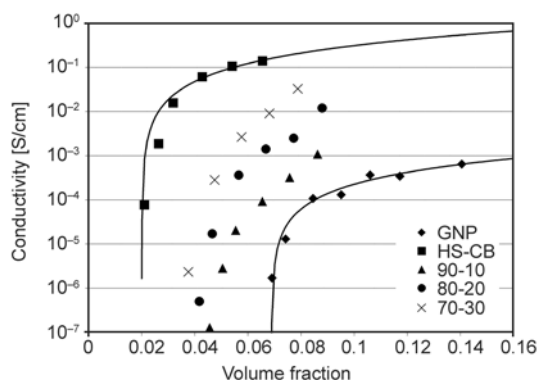


Figure 5. The electrical conductivity as a function of the filler content for composites containing GNP, HS-CB and hybrids. Solid lines represent fitting to the percolation theory Equation (2).

a solution mixing method which is more effective compared to melt-mixing [24, 25]. For polypropylene, a percolation threshold of 7 vol% has been found in a melt mixed material [26].

By replacing only 10 wt% of the total filler content with HS-CB instead of GNP, the electrical percolation was dramatically reduced, from 6.9 to 4.6 vol%, whereas the conductivity plateau above the threshold increased (Figure 5). The same effect was observed when larger amounts of the overall filler content were replaced with CB. The effect of hybridization with CB has been studied earlier by Fan *et al.* [10] in epoxy-based composites, where by replacing 10% of the total filler content (GNP) with a high-structured carbon black the conductivity increased three orders of magnitude compared to the case with GNP alone when the total filler content was 1 wt%. They also observed a decrease in the percolation threshold from 0.75 to 0.5 wt%. This effect can be attributed to the existence of conductive bridges between the individual GNP agglomerates created by the CB particles. The reasoning for this is that high-structured CB being smaller and of significantly lower aspect ratio than GNP has a tendency of dispersing in a more efficient manner. This dispersion can act like a physical bridge between the GNP-rich areas in the matrix while at the same time restricts their dispersion and reagglomeration (see Figure 2). In the work by Wei *et al.* [14] carbon nanotubes were introduced in a similar system resulting in a three-filler-hybrid composite, and an even lower percolation threshold of 0.2 wt% was reported. These effects were also attributed to the ability of the spherical CB particles and the long flexible CNTs to form effective links between the more rigid GNPs.

The orientation in the flow direction of the anisotropic fillers will influence the electrical properties. An extended level of orientation of the platelets could be expected to result in a higher percolation threshold due to a decreased particle-particle interaction [5, 9]. Therefore it is expected that the extruded strands used in this study will exhibit a higher percolation threshold than the corresponding non-oriented composites. For the pure GNP system and the 80-20 hybrid a higher piston speed (20 mm/min) was used to enhance the orientation of the fillers. This increased the onset of electrical conductivity to approximately 7.4 and 4.7 vol%, respectively, and can be compared with the results for 2 mm/min where the onset was 6.9 and 4.2 vol%, respectively.

The experimental data was fitted to the classical percolation theory (Equation (2)):

$$\sigma = \kappa(\omega - \omega_c)^\beta \quad (2)$$

where σ is the conductivity of the composite, ω is the filler content, ω_c the filler content at the percolation threshold, κ and β are fitting parameters where κ is related to the conductivity of the filler and β is connected to the systems dimensionality [27]. Here it must be noted that Equation (2) is derived for ideal conditions where all filler particles are of equal size, not agglomerated and non-oriented.

The percolation behavior of the pure CB and GNP systems could be fitted to Equation (2) as shown in Figure 5. The hybrid systems could not be fitted due to the lack of a clear conductivity plateau at higher loadings resulting in an unrealistic high value of κ . The lack of conductivity plateau is believed to originate from the increasing amount of CB with increasing filler content.

The conductivity results for the low-structured CB, the pure GNP and their hybrids are shown in Figure 6. The pure CB-based composite was seen to have a higher percolation threshold (12.1 vol%) and conductivity plateau at high loadings than its GNP-based equivalent. In a similar study using poly(ethyl-vinyl acetate) copolymer as matrix, the higher level of the conductivity plateau for CB-based systems in comparison with the GNP-based ones was attributed to the extended agglomeration of the GNPs and the subsequent overall aspect ratio reduction [5]. The substantially higher percolation threshold of the LS-CB compared to the HS-CB is likely associated

with the much lower BET surface area of the former particles.

For the low-structured CB hybrids, the percolation threshold decreased when some of the GNP was replaced by CB, at least in the case of the 80-20 and 70-30 hybrids. In the 60-40 hybrid the percolation threshold is slightly higher compared to the pure GNP but the conductivity plateau was, as for the other hybrids, higher than for the pure GNP system. This latter behavior can be discussed in a similar manner as for the HS-CB systems. Even though the percolation threshold was higher for the LS-CB compared to the GNP, the CB particles were effective in the building up a conductive network by connecting the 2-dimensional oriented GNPs with each other. A synergistic effect, not as strong as in the HS-CB hybrids, was observed resulting in a decrease of the percolation threshold.

Figure 7 shows the electrical conductivity of the solvent-mixed materials as a function of the filler content. For the melt-mixed materials, the percolation threshold for the pure GNP systems was approximately 6.9 vol%. Here it must be noted that the 10 wt% (4.5 vol%) solution-mixed composition had similar conductivity as the 7.4 vol% melt-mixed composition indicating a significant decrease in the percolation threshold. The same pattern can be seen for the hybrid formulations where for example the solution-mixed 80-20 hybrid at 10 wt% (4.7 vol%) had similar conductivity level as the 7.7 vol% melt mixed composition. Based on these results, the solution-mixing process was more efficient in terms of filler dispersion in comparison with the melt-mixing one for this specific combination of polymer

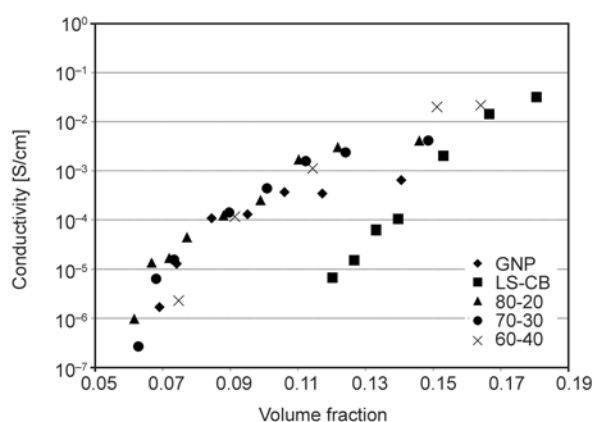


Figure 6. The electrical conductivity as a function of the filler content for composites containing GNP, LS-CB and hybrids

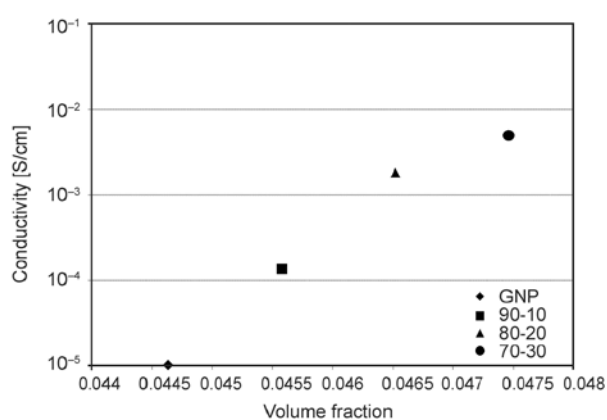


Figure 7. The electrical conductivity for solvent-mixed composites based on GNP or GNP/HS-CB containing 10 wt% filler

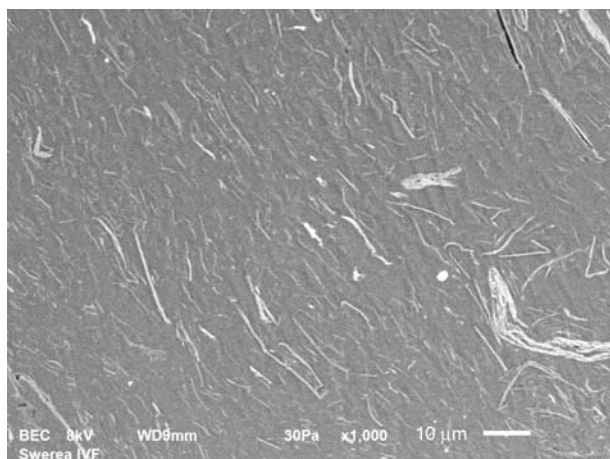


Figure 8. Scanning electron micrograph of the solvent-mixed material containing 10 wt% GNP at a magnification of 1000×

and filler, something that has been seen in earlier works of many authors [26, 28–30]. In the work by Oxfall *et al.*, [28] GNP was mixed with polystyrene (PS), and it was observed that relatively large agglomerates were present in the composite after the melt mixing process. However when a solution-mixing method was employed, the number of large agglomerates was dramatically reduced resulting in a higher conductivity. In the present study, no differences could be discerned between the solvent and melt mixed systems with respect to the overall agglomerate size, see Figure 8. The decrease in percolation threshold observed when the solution-mixing method is used is thought to originate from the more efficient formation of thin graphite stacks [28]. Persson *et al.* [31] have shown that thin graphene stacks, consisting of mainly three layers and not more than five layers, are formed when employing solution mixing and these are likely to contribute to

Table 1. Electrical percolation thresholds for the different materials

System	Percolation threshold [vol%]	Piston speed at extrusion [mm/min]
GNP	$6.4 < \omega_c < 6.9$	2
GNP	$6.9 < \omega_c < 7.4$	20
HS-CB	$1.8 < \omega_c < 2.1$	2
GNP/HS-CB, 90-10	$4.0 < \omega_c < 4.6$	2
GNP/HS-CB, 80-20	$3.7 < \omega_c < 4.2$	2
GNP/HS-CB, 80-20	$4.2 < \omega_c < 4.7$	20
GNP/HS-CB, 70-30	$3.3 < \omega_c < 3.8$	2
LS-CB	$11.4 < \omega_c < 12.0$	2
GNP/LS-CB, 80-20	$5.6 < \omega_c < 6.2$	2
GNP/LS-CB, 70-30	$5.8 < \omega_c < 6.3$	2
GNP/LS-CB, 60-40	$6.9 < \omega_c < 7.5$	2

the lower percolation threshold in case of the equivalent systems observed in the present study.

Table 1 is a summary of the electrical percolation thresholds reported in this work and at which extrusion speeds the specimens were produced.

3.4. Rheological properties

Figures 9 and 10 show the storage modulus, G' , as a function of frequency for the systems containing GNP, high-structured CB. Typically, there is a correlation between the plateau of G' at the lower frequencies (solid-like response) and the onset of the electrical conductivity (see references [5, 7, 9 and 32] for further discussion). Another way of analyzing the rheological data is to find when G' becomes larger than the loss modulus G'' at low frequencies. This can also constitute a measure of the rheological percolation [33]. In the present work, the filler concentration where the cross-over between G' and G''

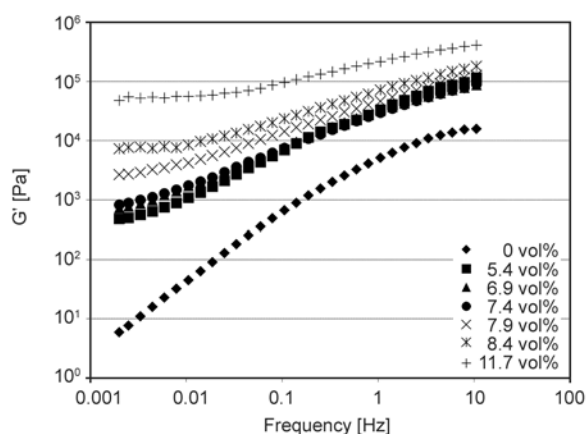


Figure 9. The storage modulus G' vs frequency for the GNP/EBA composites at different filler contents measured at 180°C

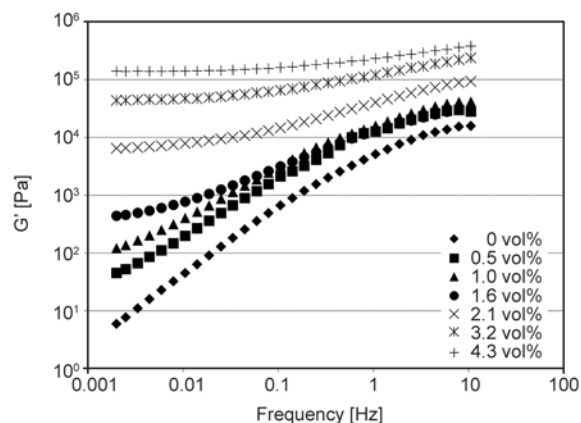


Figure 10. The storage modulus G' vs frequency for the HS-CB/EBA composites at different filler contents measured at 180°C

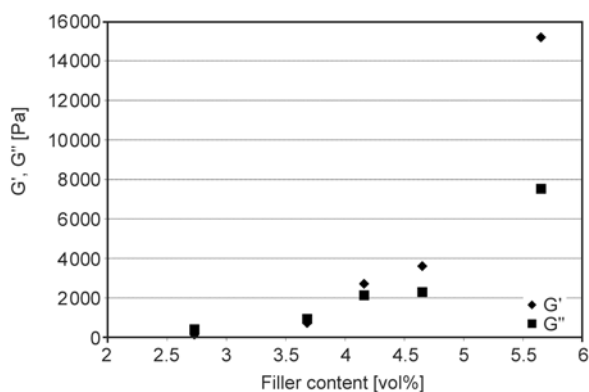


Figure 11. G' and G'' as a function of the filler content of the 80-20 hybrid containing GNP and HS-CB measured at 180°C

took place was evaluated assuming a linear dependence of the moduli as functions of the filler content. The moduli G' and G'' as function of filler content for the 80-20 hybrid are shown in Figure 11. Table 2 shows the filler content at which the cross-over of the two moduli occurs. It should be made clear that an exact relation between the rheological and the electrical percolations are not expected in this case since the two types of test specimens differ in the degree of orientation; i.e. the rheological studies were conducted with non-oriented melts whereas the conductivity was measured using extruded strands. However similar trends can be noted when comparing the results in Tables 1 and 2.

The filler content at which the cross-over occurred was significantly higher for the GNP-based composite in comparison with the HS-CB-based system. As shown in Table 2, even small amounts of the high-structured CB reduced the cross-over concentration significantly in case of the HS-CB based hybrids. In the case of the LS-CB systems the rheological percolation (for the same filler content) was observed to be of similar order to the one observed for the GNP-composite. Replacing some of the GNP with

Table 2. The filler content at the G'/G'' crossover (rheological percolation)

System	G'/G'' cross over [vol%]
GNP	7.4
HS-CB	1.5
GNP/HS-CB, 90-10	5.2
GNP/HS-CB, 80-20	3.8
GNP/HS-CB, 70-30	3.2
LS-CB	7.3
GNP/LS-CB, 80-20	8.3
GNP/LS-CB, 70-30	8.6
GNP/LS-CB, 60-40	8.1

the low structured CB actually produced an increase of the onset of rheological percolation.

Although it is not expected that there would be a very close agreement between the threshold values from the rheology and conductivity measurements, due to the orientation and possibly to the crystallization behavior, it is worthwhile to comment on this. First it can be noted that all composites exhibited a solid-like behavior at higher filler contents as manifested by the plateau in the storage modulus in the low frequency region. This can be associated with the formation of a filler network. The filler concentration at the G'/G'' cross-over was higher for the GNP composite (no CB) than the electrical percolation threshold, (Tables 1 and 2). In Figure 9 it can be seen that the flattening of G' at lower frequencies took place between 7.4 and 7.9 vol% which is in correspondence with the G'/G'' cross-over. In the case of the HS-CB, the G'/G'' cross-over concentration was lower than the electrical percolation threshold. The cross-over concentration corresponded again reasonably well with the flattening of G' at 1.6 vol% (Figure 10). Based on this we can see that the GNP and the HS-CB systems behave in an opposite manner when the different percolation thresholds are compared.

With increasing amounts of HS-CB in the hybrid systems, the rheological threshold shifted from above the electrical threshold below it for the 70-30 hybrid. The correlation between the two thresholds is quite reasonable for the HS-CB/GNP systems considering the difference in orientation between the specimens. Strååt *et al.* [23] reported a good agreement between the electrical and the rheological thresholds in the case of PP and PE containing the same type of high-structured CB as used in this study. The conductivity measurements reported in this case [23] were also performed using extruded strands.

For the LS-CB systems the correlation between the rheological and the electrical percolation was clearly poorer. In Figure 12, G' as a function of frequency is shown for the LS-CB/EBA materials and it is evident that the flattening of G' at lower frequencies started already at 7.1 vol% compared to the onset of electrical conductivity between 11.4 and 12 vol%. The G'/G'' cross-over indicated a similar low value of 7.3 vol%. The hybrids containing LS-CB exhibited, in similarity with the GNP/EBA material, a higher G'/G'' cross-over compared to the

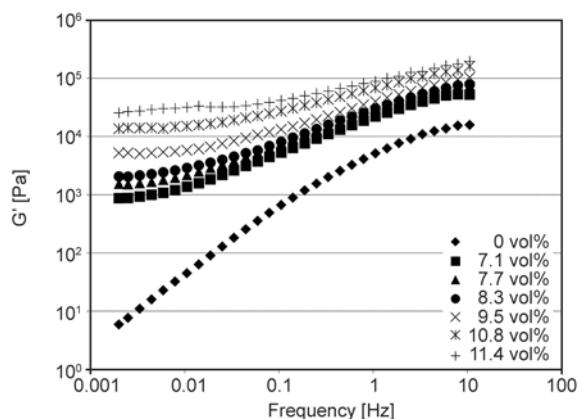


Figure 12. The storage modulus G' vs frequency for the LS-CB EBA composites at different filler contents measured at 180°C

electrical percolation. The difference between the two decreased however with increasing amounts of LS-CB, (Table 2).

4. Conclusions

The effect of both low- and high-structured carbon black on the electrical and the rheological properties of graphite nanoplatelet/poly(ethylene-butyl acrylate) composite have been assessed. It was found that the presence of both high- and low-structured CB in the matrix lead to a decrease of the electrical percolation threshold, with the effect being more pronounced in the case of the high-structured carbon black. This synergistic effect has been attributed to the creation of conductive bridges between the two different fillers.

In the extruded specimens used for electrical measurements a significant orientation of the filler particles in the flow direction was observed. The orientation had a significant effect on the overall conductivity of the composites.

Both melt and solution mixing methods were employed when producing the composite materials and the solution-based systems are seen to exhibit lower percolation threshold than the melt-mixed ones. This was attributed to the enhanced dispersion that is achieved by the solution process.

The presence of CB and GNP in the matrix affects the overall morphology of the system leading to thinner crystals and slight changes in the degree of crystallinity, evident by the slightly narrower melting endotherm and the shifted melting point.

Even though two types of test specimens that differed in the degree of orientation were used for the electrical and rheological measurements similar

trends can be noted when comparing the electrical and rheological percolation thresholds. The composites containing high-structured carbon black, graphite nanoplatelets and their hybrids showed a quite reasonable correlation between the two types of percolation values. For the composites containing the low-structured carbon black, the correlation between the rheological and the electrical percolation thresholds was clearly poorer.

Acknowledgements

The authors thank Lars Eklund, Swerea IVF, for helping with the SEM studies, Christer Svanberg and Davide Tranchida, Borealis AB, for valuable discussions. Finally we would like to thank the anonymous reviewers whose comments and suggestions greatly enhanced the manuscript. Financial support from the Swedish Foundation for Strategic Research (SSF) is gratefully acknowledged.

References

- [1] Chodák I., Omastová M., Pionteck J.: Relation between electrical and mechanical properties of conducting polymer composites. *Journal of Applied Polymer Science*, **82**, 1903–1906 (2001). DOI: [10.1002/app.2035](https://doi.org/10.1002/app.2035)
- [2] Lewis T. J.: Nanometric dielectrics. *IEEE Transactions on Dielectrics and Electrical Insulation*, **1**, 812–825 (1994). DOI: [10.1109/94.326653](https://doi.org/10.1109/94.326653)
- [3] Tanaka T., Montanari G. C., Mülhaupt R.: Polymer nanocomposites as dielectrics and electrical insulation-perspectives for processing technologies, material characterization and future applications. *IEEE Transactions on Dielectrics and Electrical Insulation*, **11**, 763–784 (2004). DOI: [10.1109/TDEI.2004.1349782](https://doi.org/10.1109/TDEI.2004.1349782)
- [4] Jeong K-U., Lim J. Y., Lee J-Y., Kang S. L., Nah C.: Polymer nanocomposites reinforced with multi-walled carbon nanotubes for semiconducting layers of high-voltage power cables. *Polymer International*, **59**, 100–106 (2010). DOI: [10.1002/pi.2696](https://doi.org/10.1002/pi.2696)
- [5] Gkourmpis T.: Carbon-based high aspect ratio polymer nanocomposites. in 'Nanoscience and computational chemistry: Research progress' (eds.: Mercader G. A., Castro E. A., Haghi A. K.) Apple Academic Press, Toronto, Vol 1, 85–124 (2014).
- [6] Novoselov K. S., Geim A. K., Morozov S. V., Jiang D., Zhang Y., Dubonos S. V., Grigorieva I. V., Firsov A. A.: Electric field effect in atomically thin carbon films. *Science*, **306**, 666–669 (2004). DOI: [10.1126/science.1102896](https://doi.org/10.1126/science.1102896)
- [7] Potts J. R., Dreyer D. R., Bielawski C. W., Ruoff R. S.: Graphene-based polymer nanocomposites. *Polymer*, **52**, 5–25 (2011). DOI: [10.1016/j.polymer.2010.11.042](https://doi.org/10.1016/j.polymer.2010.11.042)

- [8] Sengupta R., Bhattacharya M., Bandyopadhyay S., Bhowmick A. K.: A review on the mechanical and electrical properties of graphite and modified graphite reinforced polymer composites. *Progress in Polymer Science*, **36**, 638–670 (2011).
DOI: [10.1016/j.progpolymsci.2010.11.003](https://doi.org/10.1016/j.progpolymsci.2010.11.003)
- [9] Kim H., Abdala A. A., Macosko C. W.: Graphene/polymer nanocomposites. *Macromolecules*, **43**, 6515–6530 (2010).
DOI: [10.1021/ma100572e](https://doi.org/10.1021/ma100572e)
- [10] Fan Z., Zheng C., Wei T., Zhang Y., Luo G.: Effect of carbon black on electrical property of graphite nanoplatelets/epoxy resin composites. *Polymer Engineering and Science*, **49**, 2041–2045 (2009).
DOI: [10.1002/pen.21445](https://doi.org/10.1002/pen.21445)
- [11] Ren P-G., Di Y-Y., Zhang Q., Li L., Pang H., Li Z-M.: Composites of ultrahigh-molecular-weight polyethylene with graphene sheets and/or MWCNTs with segregated network structure: Preparation and properties. *Macromolecular Materials and Engineering*, **297**, 437–443 (2012).
DOI: [10.1002/mame.201100229](https://doi.org/10.1002/mame.201100229)
- [12] Li J., Wong P-S., Kim J-K.: Hybrid nanocomposites containing carbon nanotubes and graphite nanoplatelets. *Materials Science and Engineering: A*, **483–484**, 660–663 (2008).
DOI: [10.1016/j.msea.2006.08.145](https://doi.org/10.1016/j.msea.2006.08.145)
- [13] Kumar S., Sun L. L., Caceres S., Li B., Wood W., Perugini A., Maguire R. G., Zhong W. H.: Dynamic synergy of graphitic nanoplatelets and multi-walled carbon nanotubes in polyetherimide nanocomposites. *Nanotechnology*, **21**, 105702/1–105702/10 (2010).
DOI: [10.1088/0957-4484/21/10/105702](https://doi.org/10.1088/0957-4484/21/10/105702)
- [14] Wei T., Song L., Zheng C., Wang K., Yan J., Shao B., Fan Z-J.: The synergy of a three filler combination in the conductivity of epoxy composites. *Materials Letters*, **64**, 2376–2379 (2010).
DOI: [10.1016/j.matlet.2010.07.061](https://doi.org/10.1016/j.matlet.2010.07.061)
- [15] Via M. D., Morrison F. A., King J. A., Beach E. A., Wiese K. R., Bogucki G. R.: Effects of multiple carbon fillers on the rheology of polycarbonate-based composites. *Polymer Composites*, **33**, 306–316 (2012).
DOI: [10.1002/pc.22149](https://doi.org/10.1002/pc.22149)
- [16] Hess W. M., Herd C. R.: Microstructure, morphology and general physical properties. in ‘Carbon black science and technology’ (eds.: Donnet J-B., Bansal R. C., Wang M-J.) Taylor and Francis, London, 89-160 (1993).
- [17] Heaney M. B.: Electrical conductivity and resistivity. in ‘Electrical Measurement, Signal Processing and Displays’ (ed.: Webster J. G.) CRC Press, Vol 1, 7/1–7/14 (2003).
- [18] Kim H., Macosko C. W.: Processing-property relationships of polycarbonate/graphene composites. *Polymer*, **50**, 3797–3809 (2009).
DOI: [10.1016/j.polymer.2009.05.038](https://doi.org/10.1016/j.polymer.2009.05.038)
- [19] Kim H., Macosko C. W.: Morphology and properties of polyester/exfoliated graphite nanocomposites. *Macromolecules*, **41**, 3317–3327 (2008).
DOI: [10.1021/ma702385h](https://doi.org/10.1021/ma702385h)
- [20] Xu J-Z., Chen T., Yang C-L., Li Z-M., Mao Y-M., Zeng B-Q., Hsiao B. S.: Isothermal crystallization of poly(L-lactide) induced by graphene nanosheets and carbon nanotubes: A comparative study. *Macromolecules*, **43**, 5000–5008 (2010).
DOI: [10.1021/ma100304n](https://doi.org/10.1021/ma100304n)
- [21] Xu J-Z., Chen C., Wang Y., Tang H., Li Z-M., Hsiao B. S.: Graphene nanosheets and shear flow induced crystallization in isotactic polypropylene nanocomposites. *Macromolecules*, **44**, 2808–2818 (2011).
DOI: [10.1021/ma1028104](https://doi.org/10.1021/ma1028104)
- [22] Kalaitzidou K., Fukushima H., Askeland P., Drzal L. T.: The nucleating effect of exfoliated graphite nanoplatelets and their influence on the crystal structure and electrical conductivity of polypropylene nanocomposites. *Journal of Materials Science*, **43**, 2895–2907 (2008).
DOI: [10.1007/s10853-007-1876-3](https://doi.org/10.1007/s10853-007-1876-3)
- [23] Strååt M., Toll S., Boldizar A., Rigdahl M., Hagström B.: Melt spinning of conducting polymeric composites containing carbonaceous fillers. *Journal of Applied Polymer Science*, **119**, 3264–3272 (2011).
DOI: [10.1002/app.32882](https://doi.org/10.1002/app.32882)
- [24] Kim S., Do I., Drzal L. T.: Multifunctional xGnP/LLDPE nanocomposites prepared by solution compounding using various screw rotating systems. *Macromolecular Materials and Engineering*, **294**, 196–205 (2009).
DOI: [10.1002/mame.200800319](https://doi.org/10.1002/mame.200800319)
- [25] Kim S., Drzal L. T.: Comparison of exfoliated graphite nanoplatelets (xGnP) and CNTs for reinforcement of EVA nanocomposites fabricated by solution compounding method and three screw rotating systems. *Journal of Adhesion Science and Technology*, **23**, 1623–1638 (2009).
DOI: [10.1163/156856109X440984](https://doi.org/10.1163/156856109X440984)
- [26] Kalaitzidou K., Fukushima H., Drzal L. T.: A new compounding method for exfoliated graphite–polypropylene nanocomposites with enhanced flexural properties and lower percolation threshold. *Composites Science and Technology*, **67**, 2045–2051 (2007).
DOI: [10.1016/j.compscitech.2006.11.014](https://doi.org/10.1016/j.compscitech.2006.11.014)
- [27] Bauhofer W., Kovacs J. Z.: A review and analysis of electrical percolation in carbon nanotube polymer composites. *Composites Science and Technology*, **69**, 1486–1498 (2009).
DOI: [10.1016/j.compscitech.2008.06.018](https://doi.org/10.1016/j.compscitech.2008.06.018)
- [28] Oxfall H., Rondin J., Bouquey M., Muller R., Rigdahl M., Rychwalski R. W.: Elongational flow mixing for manufacturing of graphite nanoplatelet/polystyrene composites. *Journal of Applied Polymer Science*, **128**, 2679–2686 (2013).
DOI: [10.1002/app.38439](https://doi.org/10.1002/app.38439)

- [29] Shen J-W., Chen X-M., Huang W-Y.: Structure and electrical properties of grafted polypropylene/graphite nanocomposites prepared by solution intercalation. *Journal of Applied Polymer Science*, **88**, 1864–1869 (2003).
DOI: [10.1002/app.11892](https://doi.org/10.1002/app.11892)
- [30] Kim H., Macosko C.: Morphology and properties of exfoliated graphite/thermoplastic polyurethane nanocomposites. in '2009 Annual Technical Conference – ANTEC Conference Proceedings'. Chicago, USA, Vol 1, 122–125 (2009).
- [31] Persson H., Yao Y., Klement U., Rychwalski R. W.: A simple way of improving graphite nanoplatelets (GNP) for their incorporation into a polymer matrix. *Express Polymer Letters*, **6**, 142–147 (2012).
DOI: [10.3144/expresspolymlett.2012.15](https://doi.org/10.3144/expresspolymlett.2012.15)
- [32] Alig I., Pötschke P., Lellinger D., Skipa T., Pegel S., Kasaliwal G. R., Villmow T.: Establishment, morphology and properties of carbon nanotube networks in polymer melts. *Polymer*, **53**, 4–28 (2012).
DOI: [10.1016/j.polymer.2011.10.063](https://doi.org/10.1016/j.polymer.2011.10.063)
- [33] Kotsilkova R.: Thermoset nanocomposites for engineering applications. Rapra, Shawbury (2007).

Studies on the selective localization of multi-walled carbon nanotubes in blends of poly(vinylidene fluoride) and polycaprolactone

L. Li^{1,2}, W.-H. Ruan^{2*}, M.-Q. Zhang², M.-Z. Rong²

¹Materials Science Institute, The School of Chemistry and Chemical Engineering, Zhongshan University, 510275 Guangzhou, P. R. China

²National Engineering Laboratory for Plastic Modification and Processing, National-certified Enterprise Technology Center, Kingfa Science and Technology Co. LTD., 510275 Guangzhou, P. R. China.

Received 22 May 2014; accepted in revised form 17 August 2014

Abstract. A ternary system based on blends of poly(vinylidene fluoride)(PVDF) and polycaprolactone (PCL) and made the multi-walled carbon nanotubes (MWNT) selective distribution in PCL phases via melt blending has been studied. The studies on conductivity of MWNT/PCL/PVDF composites with different proportions of PVDF and PCL showed that the conductivity was good in the mass ratio range of PVDF/PCL from 70/30 to 40/60 and that of other matching was poor. The scanning electron microscope (SEM) observation of the composites revealed co-continuous morphologies of PVDF and PCL were formed in composites under suitable proportion of PVDF to PCL. The interfacial tensions of PVDF and PCL melts was tested at mixing temperature of 200°C, the calculated wetting coefficient indicated that MWNT would selectively distribute in PCL phase owing to interfacial effects. Transmission electron microscope (TEM) observation further confirmed that co-continuous morphologies of PVDF and PCL could appear with the increase of PCL content, as indicated by MWNT selective localization in PCL. As the result, the desired structure of double percolation was built in MWNT/PCL/PVDF composites, which have much higher conductivity than that of PVDF or PCL composites with the same MWNT content. Through a strategy of selective localization of MWNT, PVDF based material with low percolation threshold (<0.5 wt%) was acquired which held promise for potential use in large-scale industrial applications.

Keywords: polymer composites, poly(vinylidene fluoride), multi-walled carbon nanotubes, double percolation, low percolation threshold

1. Introduction

Conductive and dielectric materials based on PVDF have attracted considerable interests from the scientific community and industry, owing to their wide use in electrical and electronic industry [1–3]. The main advantages of PVDF-based composites are good mechanical flexibility and tunable properties for making different types of devices. Due to the insulating properties of PVDF, conductive fillers, especially nanoparticles such as CNT, carbon black, graphene and metal particles, need to be added to the

matrix. CNT/PVDF composites are one of the most important types of conductive materials because of the excellent electric and mechanical properties of CNT [4–7]. Solution mixing CNT with PVDF, involving sonication, is usually preferred in the lab studies of CNT/PVDF composites and relatively low percolation threshold of CNT could be achieved. But solution mixing is a solvent-consuming process, which is not suitable for industrial production. CNT/PVDF nanocomposites prepared by melt compounding, which is a feasible way for large-scale pro-

*Corresponding author, e-mail: cesrwh@mail.sysu.edu.cn
© BME-PT

duction, have been reported with the manufacture of MWNT reaching industrial scale in recent years [8–10]. However the percolation thresholds are much higher (>2.5 wt%) than those of solution mixing ones, indicating that the major problem of melt compounding CNT/PVDF composites is the poor dispersion of CNT in polymer matrices. Many studies were carried out to deal with the problem [11–14]. The design of double percolation structure in composites is one of the methods to reduce the percolation threshold of conductive fillers [15–21]. The concept of double percolation was first proposed by Sumita *et al.* [21] in immiscible blends that were filled with carbon black. Two requirements are needed to realize the double percolation structure in composites. One requires co-continuous blend morphologies, the other needs selective filling of only one of the blend phases (double percolation). Preferential localization of conductive filler in one of the phases is commonly explained by the differences in interfacial energies of the filler and the corresponding polymer, which originates from the different polarities and surface energies. Some of the authors compared the prediction of the wetting coefficient or equivalent equations that described the localization of fillers in blends to their experimental observations [22–24]. However, it was very difficult to get the interfacial tensions of polymer melt at the processing temperature. The interfacial tensions of polymer at room temperature were used to predict the wetting coefficient [22, 23, 25], but sometimes results deviating from actual situation might be obtained. There are a few reports about CNT/PVDF composites prepared by double percolation concept [23, 26]. But the interfacial effect for predicting the localization of conductive fillers was not studied at all. To understand the interfacial effect on selective distribution of MWNT, the interfacial tensions of PVDF melt at processing temperature should be investigated.

In order to prepare PVDF based conductive material with low percolation threshold by melt blending, a ternary system of MWNT/PCL/PVDF for double percolation was designed in this paper. The pendant drop method [27, 28] was applied to measure the interfacial tensions of polymer melts at processing melt for selective localization of MWNT. Formation of co-continuous morphologies in composites by adjusting the proportions of PVDF to PCL were investigated. The study should contribute to acquir-

ing a basic knowledge of the development of low electrically percolated MWNT/PVDF composites on industrial scale.

2. Experimental section

2.1. Materials

The PVDF resin (solef1010) with an average molecular weight of 45 000 was purchased from the Solvay Company (Brussels, Belgium). The multi-walled carbon nanotubes (MWNT) with a length of 10–30 μm and an outer diameter of 10–20 nm were obtained from the Chengdu Institute of Organic Chemistry (China). PCL resin with an average molecular weight of 80 000 was purchased from the Esun Company (Shenzhen, China).

2.2. Sample preparations

The PVDF matrix and MWNT were dried in the vacuum oven at 90°C and PCL was dried at 50°C for 12 h before being mixed. The PCL and MWNT were first mixed in the Haake mixer at 110°C for 10 min and MWNT/PCL composites with different concentrations of MWNT were obtained. Then MWNT/PCL composites were added into PVDF according to pre-fixed proportions of PVDF to PCL. The MWNT/PCL/PVDF blends were mixed in the Haake mixer at 200°C for 10 min.

2.3. Characterization

Conductive properties of MWNT/PCL/PVDF composites were tested by a high-resistance meter (Agilent 4339B, United States of America). The granules of MWNT/PCL/PVDF blends were pressed with a fixed pressure in a hydraulic machine and the sheets of MWNT/PCL/PVDF composites were obtained. The sample size is 20 mm×20 mm×0.2 mm at least. The wide measurement range is 10^3 to $1.6 \cdot 10^{16} \Omega$ with a 10 ms high-speed measurement.

The interfacial tensions of PCL and PVDF melt were tested by the Krüss DSA 100 (Krüss Company, Ltd., Germany) apparatus with the pendant drop method at 200°C, respectively.

The phase structure of the PVDF and PCL was characterized by a scanning electron microscope (SEM, JEOL JSM-5400, Japan) with an accelerating voltage of 7.0 kV. The samples were held in liquid nitrogen for 40 min and then impact fractured for SEM analysis. The fractured surface was etched by acetic acid in order to dissolve the PCL phase. The samples were gold sputtered before SEM observation. The

dispersion of MWNT in PVDF/PCL was observed with a transmission electron microscope (TEM, FEITecnai G2 Spirit) with an accelerating voltage of 120 kV. Ultrathin sections of the samples were prepared in liquid nitrogen before TEM observation.

3. Results and discussion

Conductive properties of the composites with different mass ratio of PVDF and PCL contained 1.5 wt% of MWNT were shown in Figure 1. It is clear to see that conductivity of the composites changed with the increase of PCL content. There was an abrupt increase in conductivity above PVDF/PCL of 90/10, a plateau from PVDF/PCL of 70/30 to 40/60, and a sharp decrease after PVDF/PCL of 40/60. The results indicated that the phase morphologies of the composites changed through adjusting the content of PCL, leading to the changes of the conductive properties.

SEM images of 1.5 wt% MWNT/PCL/PVDF composites were given in Figure 2. In order to distinguish PCL phase from PVDF phase, the samples were etched by acetic acid to remove PCL in the cross-section. Figure 2a and 2b are photos of PVDF/PCL = 90/10 system before and after being etched, respectively. The pits in the fractured surface of etched 90/10 sample indicated that the PVDF and PCL showed the sea-island morphology. When the content of PCL increased, gullies appeared in the photo of etched 83/17 sample. It was clear that co-continuous phase morphologies presented in the photo of etched 62/38 sample. By recalling the results of Figure 1, It suggested that the conductivity of composites became much better with the phase morphologies changing from sea-island to co-continuous. It meant that co-continuous phase enabled the formation of conductive pathways with MWNT net-

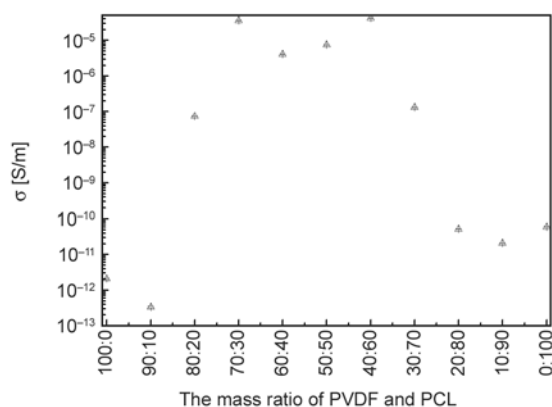


Figure 1. Conductive properties of 1.5 wt% MWNT/PCL/PVDF with different mass ratio of PVDF and PCL

work. The sharp decrease after PVDF/PCL of 40/60 was attributed to decrease of the relative concentration of MWNT in PCL since MWNT content was fixed to 1.5 wt% of the whole component.

The distribution of MWNT is another important factor in this ternary system. The wetting parameter (ω_a) can predict the selective distribution of MWNT in those immiscible polymer blends [29, 30]. For MWNT/PCL/PVDF composites, it can be described by Equation (1):

$$\omega_a = \frac{\gamma_{MWNT-PVDF} + \gamma_{MWNT-PCL}}{\gamma_{PVDF-PCL}} \quad (1)$$

where $\gamma_{MWNT-PVDF}$, $\gamma_{MWNT-PCL}$ and $\gamma_{PVDF-PCL}$ represented the interfacial tensions between MWNT and PVDF matrix, between MWNT and PCL matrix, and between PVDF and PCL. If $\omega_a > 1$, MWNT will preferentially distribute in PCL. If $\omega_a < -1$, MWNT will preferentially distribute in PVDF. And if $-1 < \omega_a < 1$, MWNT are distributed in the interface between PVDF and PCL. The interfacial tension is calculated by the surface energies of the components including their dispersive and polar parts. According to the theory of Wu [31], the interfacial tensions between two phases (γ_{12}) can be estimated by the harmonic-mean equation (Equation (2)) and geometric-mean equation ((Equation (3))):

Harmonic-mean equation

$$\gamma_{12} = \gamma_1 + \gamma_2 - 4 \left(\frac{\gamma_{1d}\gamma_{2d}}{\gamma_{1d} + \gamma_{2d}} + \frac{\gamma_{1p}\gamma_{2p}}{\gamma_{1p} + \gamma_{2p}} \right) \quad (2)$$

Geometric-mean equation

$$\gamma_{12} = \gamma_1 + \gamma_2 - 2(\sqrt{\gamma_{1d}\gamma_{2d}} + \sqrt{\gamma_{1p}\gamma_{2p}}) \quad (3)$$

where γ represents the surface tension and the subscripts 1 and 2 stand for phases 1 and 2, respectively. γ_d is the dispersion component of surface tension, and γ_p is the polar component. The relationship of γ , γ_d and γ_p can be expressed by the equation: $\gamma = \gamma_d + \gamma_p$. The Geometric-mean equation is suitable to estimate the interfacial energy between low-energy materials and high-energy materials, such as mercury, silica, metallic oxide, etc. [31]. Compared to geometric-mean equation, the harmonic-mean equation is more suitable to the interfacial energy between low-energy materials, such as polymers, organic liquids, water, etc. [31]. Thus, harmonic-mean equa-

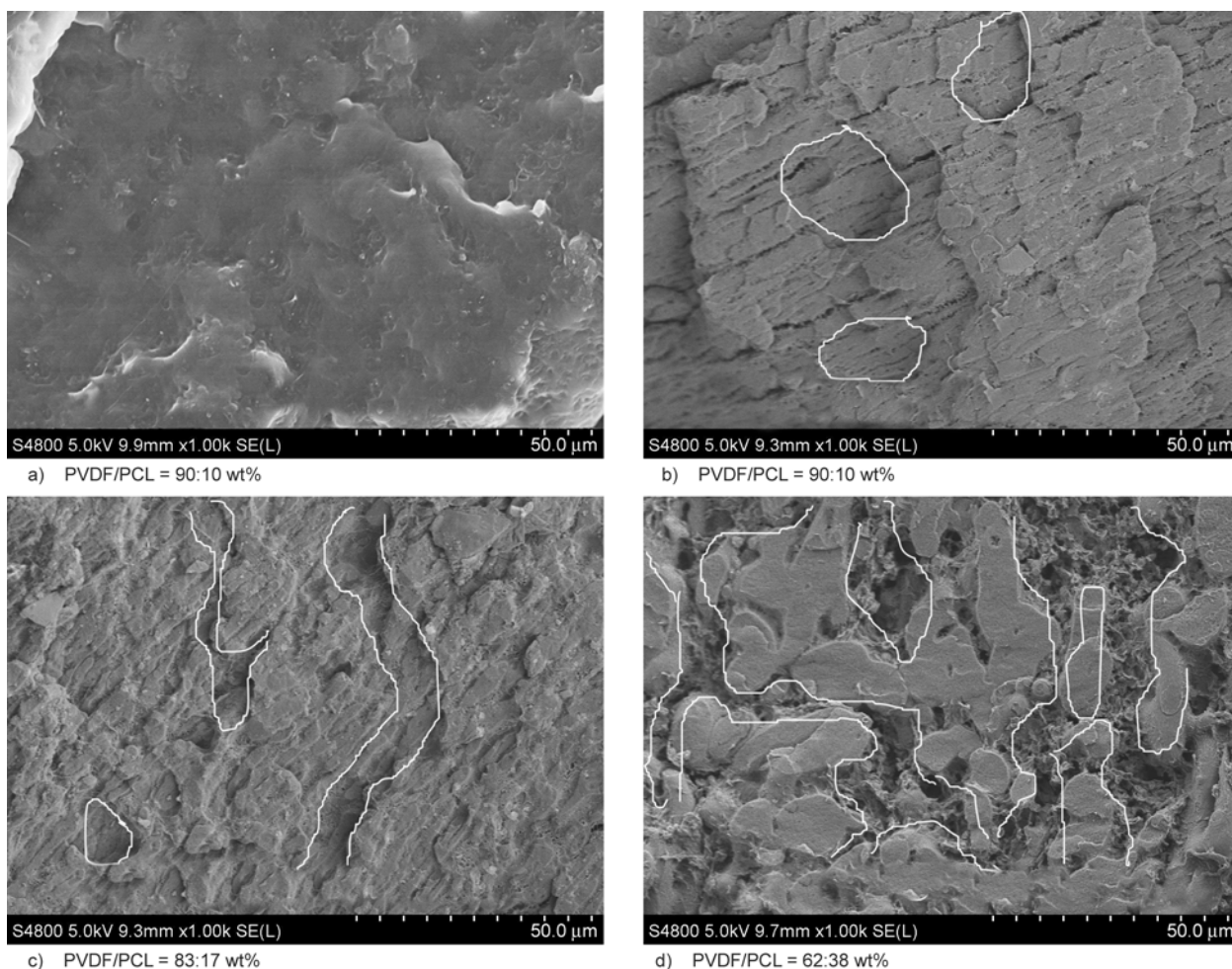


Figure 2. Morphology of the 1.5 wt% MWNT/PCL/PVDF with different concentration of PVDF: (a) PVDF/PCL = 90/10, (b) PVDF/PCL = 90/10(after being etched), (c) PVDF/PCL = 83/17 (after being etched), (c) PVDF/PCL = 62/38 (after being etched)

tion is utilized here to evaluate the interfacial energy between MWNT and polymers.

In order to understand the interfacial effect of polymer melts during processing, the interfacial ten-

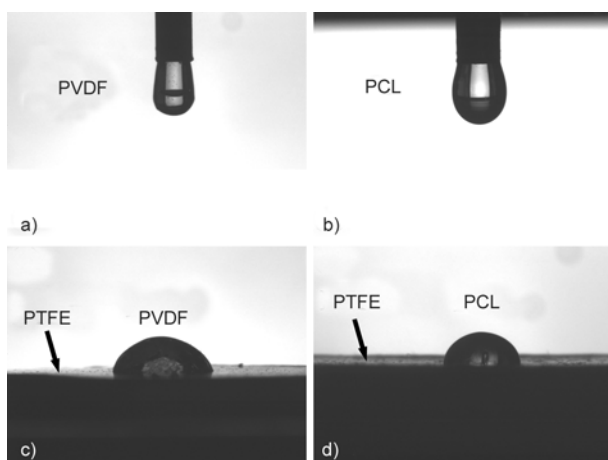


Figure 3. The drops of PVDF and PCL at 200°C: (a) and (b) pendant drops, (c) and (d) sessile drops on PTFE

sions of the polymer melts at processing temperature need to be tested. The pendant drop method is the effective method to measure the interfacial tensions of polymer melts [27, 28]. Images of pendant drops of PVDF and PCL melt were shown in Figure 3. Basing on the Young-Laplace theory, the interfacial tensions can be calculated by the size parameters. The results are calculated by fitting and listed in Table 1. The γ_d and γ_p cannot be obtained directly by this method and it can be measured by a known and stable material at testing temperature. Nonpolar PTFE was chosen as the base plate to measure the γ_d of PVDF and PCL. The γ_d of PVDF and PCL at 200°C is calculated by Equation (4):

$$\sigma^d = \frac{\sigma^2}{4\sigma_{PTFE}}(1 + \cos\theta)^2 \quad (4)$$

where σ^d represents the dispersion component of surface tension of the polymer melt, σ is the surface tension of the polymer melt, σ_{PTFE} is the surface

Table 1. Surface tensions results of PVDF and PCL at 200°C using the pendant drops method

	γ [mJ·m ⁻²]	γ_d [mJ·m ⁻²]	γ_p [mJ·m ⁻²]
PCL	29.81	21.10	8.71
PVDF	29.16	26.11	3.05

tension of the PTFE base plate. γ_p can be calculated by the equation: $\gamma_p = \gamma - \gamma_d$.

The surface tension of MWNT is obtained from related references [23, 25]. The γ , γ_d , γ_p values of MWNT are 45.3, 18.4, 26.9 mJ·m⁻² respectively. Then the interfacial energies between MWNT and polymers at 200°C were calculated by using the harmonic-mean equation: $\gamma_{MWNT-PVDF} = 20.33$ mJ·m⁻², $\gamma_{MWNT-PCL} = 9.48$ mJ·m⁻² and $\gamma_{PVDF-PCL} = 3.26$ mJ·m⁻². From Equation (1), ω_a value of 3.33 is obtained. Because of $\omega_a > 1$, these calculations provide an explanation for the selective distribution of MWNT in the PCL phase by interfacial effects when thermodynamic equilibrium is reached.

To further observe the dispersion of MWNT in composites, TEM micrographs of 1.5 wt% MWNT/PCL/PVDF were shown in Figure 4. PVDF and PCL phase cannot be distinguished by the TEM images all alone, but the dispersion of WMTNT in MWNT/PCL/PVDF composite is easy to be seen in TEM images. The dispersion of MWNT could indicate the distribution of PCL phase since studies on interfacial effect confirmed the selective localization of MWNT in PCL. It can be seen that MWNT formed large aggregates in the PVDF/PCL = 90/10 system (Figure 4a), which demonstrated sea-island morphology of the composites. With the increase of PCL content, the phase morphology of PVDF/PCL began to change from sea-island to the co-continuous as dis-

persion of MWNT was improved (Figure 4b). Well-developed co-continuous morphologies are clearly visible in 62/38 system, MWNT selectively filled the zonal PCL phase and formed a network (Figure 4c). As the result, co-continuous blend phase (first percolation) in combination with the formation of MWNT networks by selectively filling the blend phase (second percolation) built the desired structure of double percolation in MWNT/PVDF/PCL composites.

Conductive properties of different proportions of PVDF and PCL with different concentration of MWNT were displayed in Figure 5. There was no percolation threshold below the MWNT concentration of 2.5 wt% in MWNT/PVDF composites, similar to the reported studies on MWNT/PVDF prepared by melt blending method [9, 10, 32]. The percolation threshold of MWNT/PCL is about 1.5 wt% owing to better compatibility between PCL and MWNT. The conductivity of MWNT/PVDF/PCL =

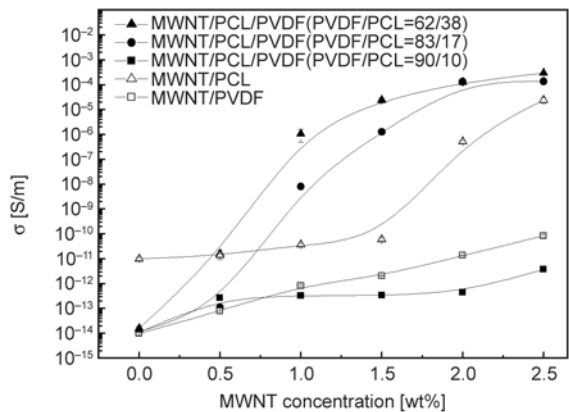


Figure 5. Conductive properties of different proportions of PVDF and PCL matrixes with different concentration of MWNT through melt blending

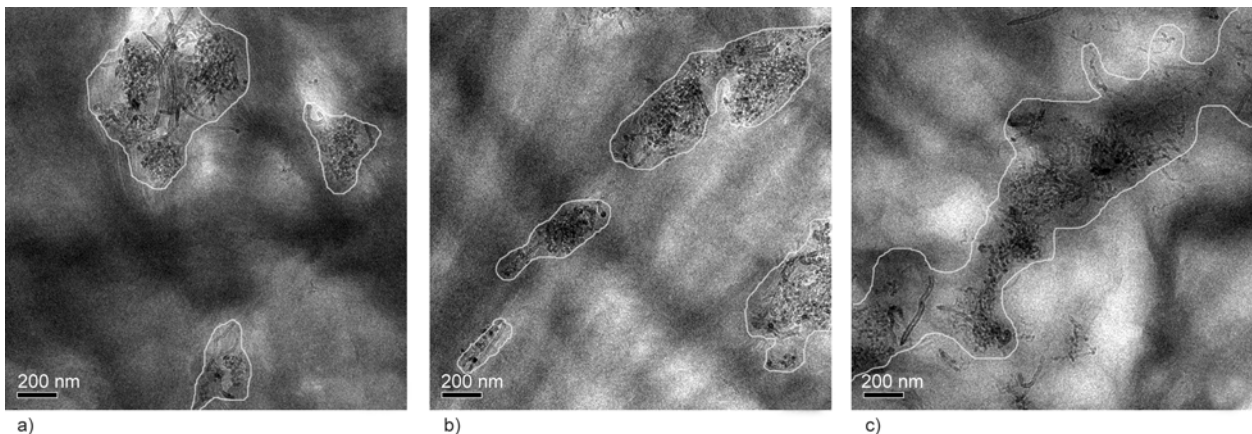


Figure 4. TEM micrographs of 1.5 wt% MWNT/PCL/PVDF: (a) PVDF/PCL = 90/10, (b) PVDF/PCL = 83/17, (c) PVDF/PCL = 62/38

90/10 system was poorer than that of MWNT/PVDF because MWNT concentrated in island-phase of PCL and conductive route could not be formed, as demonstrated by TEM observation. The conductivity of MWNT/PVDF/PCL = 83/17 and MWNT/PVDF/PCL = 62/38 system showed the significantly lower electrical percolation threshold (<0.5 wt%). Comparing conductivity of composites with co-continuous phase to those of MWNT/PCL, MWNT/PVDF and MWNT/PVDF/PCL = 90/10 nanocomposites, the improvement of conductivity over some decades at the same filler loading can be clearly seen. These gave another hint to double percolation structure in co-continuous blend phase

4. Conclusions

In conclusion, a strategy of designing ternary system and selective localization of MWNT in co-continuous blend phase were taken to prepare MWNT/PVDF conductive material with low percolation threshold by melt blending. Investigation on the interfacial tensions of PVDF and PCL melts at mixing temperature and calculations of wetting coefficient confirmed selectively localization of MWNT in PCL phase. The formation of well-developed double percolated morphologies by adjusting the proportion of blends was observed. PVDF nanocomposites with low percolation threshold (<0.5 wt%) was acquired. Preferential localization of conductive filler in co-continuous blends opens perspectives for the development of conductive PVDF based material.

Acknowledgements

The authors are grateful for the support of the Natural Science Foundation of China (Grant: 51173207), the Science and Technology Department of Guangdong Province (Grants: 2011B090500004, 2012B091100313, 2012A090100006 and 2013C2FC0009), and Key projects of Guangdong Education Office (Grant: cxzd1101).

References

- [1] Wang J., Wu J., Xu W., Zhang Q., Fu Q.: Preparation of poly(vinylidene fluoride) films with excellent electric property, improved dielectric property and dominant polar crystalline forms by adding a quaternary phosphorus salt functionalized graphene. *Composites Science and Technology*, **91**, 1–7 (2014). DOI: [10.1016/j.compscitech.2013.11.002](https://doi.org/10.1016/j.compscitech.2013.11.002)
- [2] Ting Y., Gunawan H., Sugondo A., Chiu C-W.: A new approach of polyvinylidene fluoride (PVDF) poling method for higher electric response. *Ferroelectrics*, **446**, 28–38 (2013). DOI: [10.1080/00150193.2013.820983](https://doi.org/10.1080/00150193.2013.820983)
- [3] Liu Z. H., Pan C. T., Lin L. W., Li H. W., Ke C. A., Huang J. C., Wang P. S.: Mechanical properties of piezoelectric PVDF/MWCNT fibers prepared by flat/hollow cylindrical near-field electrospinning process. in '2013 8th IEEE International Conference on Nano/Micro Engineered and Molecular Systems (NEMS), Suzhou, China' 707–710 (2013). DOI: [10.1109/NEMS.2013.6559827](https://doi.org/10.1109/NEMS.2013.6559827)
- [4] Wang L., Dang Z-M.: Carbon nanotube composites with high dielectric constant at low percolation threshold. *Applied Physics Letters*, **87**, 042903/1–042903/3 (2005). DOI: [10.1063/1.1996842](https://doi.org/10.1063/1.1996842)
- [5] Hu B., Li D., Manandharm P., Fan Q., Kasilingam D., Calvert P.: CNT/conducting polymer composite conductors impart high flexibility to textile electroluminescent devices. *Journal of Materials Chemistry*, **22**, 1598–1605 (2012). DOI: [10.1039/C1JM14121J](https://doi.org/10.1039/C1JM14121J)
- [6] Thomas J. A., Iutzi R. M., McGaughey A. J. H.: Thermal conductivity and phonon transport in empty and water-filled carbon nanotubes. *Physical Review B*, **81**, 045413/1–045413/7 (2010). DOI: [10.1103/PhysRevB.81.045413](https://doi.org/10.1103/PhysRevB.81.045413)
- [7] Bui K., Grady B. P., Papavassiliou D. V.: Heat transfer in high volume fraction CNT nanocomposites: Effects of inter-nanotube thermal resistance. *Chemical Physics Letters*, **508**, 248–251 (2011). DOI: [10.1016/j.cplett.2011.04.005](https://doi.org/10.1016/j.cplett.2011.04.005)
- [8] Ke K., Wang Y., Zhang K., Luo Y., Yang W., Xie B-H., Yang M-B.: Melt viscoelasticity, electrical conductivity, and crystallization of PVDF/MWCNT composites: Effect of the dispersion of MWCNTs. *Journal of Applied Polymer Science*, **125**, 49–57 (2012). DOI: [10.1002/app.36293](https://doi.org/10.1002/app.36293)
- [9] Kim G. H., Hong S. M.: Structures and physical properties of carbon nanotube reinforced PVDF composites. *Molecular Crystals and Liquid Crystals*, **472**, 161–169 (2007). DOI: [10.1080/15421400701545494](https://doi.org/10.1080/15421400701545494)
- [10] Hong S. M., Nam Y. W., Hwang S. S., Chae D. W.: Physical properties of multi-walled carbon nanotube-filled PVDF composites prepared by melt compounding. *Molecular Crystals and Liquid Crystals*, **464**, 195–203 (2007). DOI: [10.1080/15421400601030969](https://doi.org/10.1080/15421400601030969)
- [11] Yang D-D., Xu H-P., Wang J-R., Wu Y-H.: Nickel-multiwalled carbon nanotubes/polyvinylidene fluoride composites with high dielectric permittivity. *Journal of Applied Polymer Science*, **130**, 3746–3752 (2013). DOI: [10.1002/app.39645](https://doi.org/10.1002/app.39645)

- [12] Yang C., Lin Y., Nan C. W.: Modified carbon nanotube composites with high dielectric constant, low dielectric loss and large energy density. *Carbon*, **47**, 1096–1101 (2009).
DOI: [10.1016/j.carbon.2008.12.037](https://doi.org/10.1016/j.carbon.2008.12.037)
- [13] Li Q., Xue Q., Zheng Q., Hao L., Gao X.: Large dielectric constant of the chemically purified carbon nanotube/polymer composites. *Materials Letters*, **62**, 4229–4231 (2008).
DOI: [10.1016/j.matlet.2008.06.047](https://doi.org/10.1016/j.matlet.2008.06.047)
- [14] Dang Z-M., Wang L., Yin Y., Zhang Q., Lei Q-Q.: Giant dielectric permittivities in functionalized carbon-nanotube/electroactive-polymer nanocomposites. *Advanced Materials*, **19**, 852–857 (2007).
DOI: [10.1002/adma.200600703](https://doi.org/10.1002/adma.200600703)
- [15] Liu L., Wang Y., Xiang F., Li Y., Han L., Zhou Z.: Effects of functionalized multiwalled carbon nanotubes on the morphologies and mechanical properties of PP/EVA blend. *Journal of Polymer Science Part B: Polymer Physics*, **47**, 1481–1491 (2009).
DOI: [10.1002/polb.21749](https://doi.org/10.1002/polb.21749)
- [16] Gödel A., Kasaliwal G., Pötschke P.: Selective localization and migration of multiwalled carbon nanotubes in blends of polycarbonate and poly(styrene-acrylonitrile). *Macromolecular Rapid Communications*, **30**, 423–429 (2009).
DOI: [10.1002/marc.200800549](https://doi.org/10.1002/marc.200800549)
- [17] Pang H., Yan D-X., Bao Y., Chen J-B., Chen C., Li Z-M.: Super-tough conducting carbon nanotube/ultrahigh-molecular-weight polyethylene composites with segregated and double-percolated structure. *Journal of Materials Chemistry*, **22**, 23568–23575 (2012).
DOI: [10.1039/C2JM34793H](https://doi.org/10.1039/C2JM34793H)
- [18] Jin S-H., Lee D-S.: Electrical and rheological properties of double percolated poly(methyl methacrylate)/multiwalled carbon nanotube nanocomposites. *Journal of Nanoscience and Nanotechnology*, **7**, 3847–3851 (2007).
DOI: [10.1166/jnn.2007.058](https://doi.org/10.1166/jnn.2007.058)
- [19] Bose S., Bhattacharyya A. R., Bondre A. P., Kulkarni A. R., Pötschke P.: Rheology, electrical conductivity, and the phase behavior of cocontinuous PA6/ABS blends with MWNT: Correlating the aspect ratio of MWNT with the percolation threshold. *Journal of Polymer Science Part B: Polymer Physics*, **46**, 1619–1631 (2008).
DOI: [10.1002/polb.21501](https://doi.org/10.1002/polb.21501)
- [20] Li Y., Shimizu H.: Conductive PVDF/PA6/CNTs nanocomposites fabricated by dual formation of cocontinuous and nanodispersion structures. *Macromolecules*, **41**, 5339–5344 (2008).
DOI: [10.1021/ma8006834](https://doi.org/10.1021/ma8006834)
- [21] Sumita M., Sakata K., Asai S., Miyasaka K., Nakagawa H.: Dispersion of fillers and the electrical conductivity of polymer blends filled with carbon black. *Polymer Bulletin*, **25**, 265–271 (1991).
DOI: [10.1007/BF00310802](https://doi.org/10.1007/BF00310802)
- [22] Baudouin A-C., Devaux J., Bailly C.: Localization of carbon nanotubes at the interface in blends of polyamide and ethylene-acrylate copolymer. *Polymer*, **51**, 1341–1354 (2010).
DOI: [10.1016/j.polymer.2010.01.050](https://doi.org/10.1016/j.polymer.2010.01.050)
- [23] Baudouin A-C., Bailly C., Devaux J.: Interface localization of carbon nanotubes in blends of two copolymers. *Polymer Degradation and Stability*, **95**, 389–398 (2010).
DOI: [10.1016/j.polymdegradstab.2009.11.007](https://doi.org/10.1016/j.polymdegradstab.2009.11.007)
- [24] Gödel A., Marmur A., Kasaliwal G. R., Pötschke P., Heinrich G.: Shape-dependent localization of carbon nanotubes and carbon black in an immiscible polymer blend during melt mixing. *Macromolecules*, **44**, 6094–6102 (2011).
DOI: [10.1021/ma200793a](https://doi.org/10.1021/ma200793a)
- [25] Wu D., Zhang Y., Zhang M., Yu W.: Selective localization of multiwalled carbon nanotubes in poly(ϵ -caprolactone)/polylactide blend. *Biomacromolecules*, **10**, 417–424 (2009).
DOI: [10.1021/bm801183f](https://doi.org/10.1021/bm801183f)
- [26] Gödel A., Kasaliwal G., Pötschke P.: Selective localization and migration of multiwalled carbon nanotubes in blends of polycarbonate and poly(styrene-acrylonitrile). *Macromolecular Rapid Communications*, **30**, 423–429 (2009).
DOI: [10.1002/marc.200800549](https://doi.org/10.1002/marc.200800549)
- [27] Arashiro E. Y., Demarquette N. R.: Use of the pendant drop method to measure interfacial tension between molten polymers. *Materials Research*, **2**, 23–32 (1999).
DOI: [10.1590/S1516-14391999000100005](https://doi.org/10.1590/S1516-14391999000100005)
- [28] Stauffer C. E.: The measurement of surface tension by the pendant drop technique. *The Journal of Physical Chemistry*, **69**, 1933–1938 (1964).
DOI: [10.1021/j100890a024](https://doi.org/10.1021/j100890a024)
- [29] Gödel A., Kasaliwal G., Pötschke P.: Selective localization and migration of multiwalled carbon nanotubes in blends of polycarbonate and poly(styrene-acrylonitrile). *Macromolecular Rapid Communications*, **30**, 423–429 (2009).
DOI: [10.1002/marc.200800549](https://doi.org/10.1002/marc.200800549)
- [30] Baudouin A-C., Devaux J., Bailly C.: Localization of carbon nanotubes at the interface in blends of polyamide and ethylene-acrylate copolymer. *Polymer*, **51**, 1341–1354 (2010).
DOI: [10.1016/j.polymer.2010.01.050](https://doi.org/10.1016/j.polymer.2010.01.050)
- [31] Wu S.: *Polymer interface and adhesion*. Marcel Dekker New York (1982).
- [32] Ke K., Wang Y., Zhang K., Luo Y., Yang W., Xie B-H., Yang M-B.: Melt viscoelasticity, electrical conductivity, and crystallization of PVDF/MWCNT composites: Effect of the dispersion of MWCNTs. *Journal of Applied Polymer Science*, **125**, 49–57 (2012).
DOI: [10.1002/app.36293](https://doi.org/10.1002/app.36293)